



Eidgenössische Technische Hochschule Zürich
Swiss Federal Institute of Technology Zurich

Experimental analysis of photovoltaic energy scavengers for sensor nodes

Steven Laurier

Master thesis, Academic year 2006-2007
Erasmus Exchange Program

Guest University: ETH Zurich, Switzerland
Department: Computer Engineering and Networks Laboratory
Professor : Prof. Dr. Lothar Thiele
Supervisor: Dipl. Ing. Clemens Moser

Home University: University of Ghent, Belgium
Department: Electronics and Information Systems
Professor: Prof. Dr. Dirk Stroobandt

Abstract

This thesis covers an experimental analysis of photovoltaic energy harvesters - also known as scavengers - for sensor nodes. The most important points of interest are the energy efficiencies that the harvesters can achieve and the factors their efficiency is influenced by. The experimental results shed more light on how well the performance of an energy scavenger can be predicted. We investigate the characteristics of supercapacitors as energy storage devices by means of measurement and find that the voltage over a supercapacitor is highly unreliable as indicator of the stored supercapacitor energy. A solar energy scavenger based on the design of the "Bologna scavenger" is implemented and tested. Shortcomings of this design are identified and improvements are suggested. To test the performance of the scavenger, an indoor test setup is implemented. The efficiency of the harvester is compared with simple designs where solar cell, supercapacitor and sensor node are directly connected without a regulating circuit.

Contents

1	Introduction	1
2	Photovoltaic energy harvesting	4
2.1	Solar cell characteristics	4
2.2	Maximum power point tracking techniques	5
2.2.1	Different techniques	5
2.2.2	Important comparative considerations	7
2.3	Photovoltaic energy scavengers for sensor nodes	7
2.3.1	Prometheus	7
2.3.2	Ambimax	8
2.3.3	Everlast	9
3	Supercapacitors and their unregular behaviour	11
3.1	Introduction	11
3.2	General discussion	12
3.2.1	Principles	12
3.2.2	Supercapacitors versus batteries	15
3.2.3	Current applications of supercapacitors	18
3.2.4	Modelling	19
3.3	Measurement results	22
3.3.1	Measurement setup	22
3.3.2	Leakage	24
3.3.3	Single cycle experiments	27
3.3.4	Multiple cycle experiments	35
4	Bologna energy scavenger for sensor nodes	44
4.1	Introduction	44
4.2	Circuit design	44
4.2.1	MPP tracker	44
4.2.2	DC-DC converter	49
4.2.3	Supercapacitor	52
4.2.4	Complete circuit	54
4.3	Measurement results	56
4.3.1	Test setup	56

4.3.2	Relation between main solar cell and pilot cell	58
4.3.3	Temperature influence	59
4.3.4	Normal operation	62
4.3.5	Unwanted behaviour	64
4.3.6	Comparator power supply issue	73
5	Energy efficiency performance of Bologna scavenger	77
5.1	Introduction	77
5.2	Test setup	77
5.2.1	Tested circuits	77
5.2.2	Test procedure	79
5.2.3	Accuracy of calculations	80
5.3	Efficiency definitions	82
5.3.1	Short-term or instant efficiency	82
5.3.2	Long-term or round-trip efficiency	83
5.4	Measurement results	84
5.4.1	Direct connection	84
5.4.2	Direct connection with diode	88
5.4.3	Bologna scavenger	94
5.4.4	Prototype board implementation of Bologna scavenger	97
5.5	Comparative Analysis of tested circuits	101
6	Conclusions	107
A	More pictures	109
	List of Figures	111
	List of Tables	115
	Bibliography	116

Chapter 1

Introduction

The interest in wireless sensor nodes that scavenge energy from their environment has been increasing over the last years. Thanks to the progress in the design of low power circuits, sensor nodes consume less and less power. Because of this lower power demand, small solar cell panels suffice to ensure continued sensor node operation. The advantage of solar energy over other forms of environmental energy is that the available solar energy can be predicted, at least to some extent. This allows to plan and optimize the future sensing activity in order to achieve a more sustainable operation.

Several control algorithms that perform this optimization have been recently proposed [1, 2]. These algorithms either assume lossless conversion from solar to electrical energy or model the occurring losses as a linear process. These assumptions reduce however the practical use of the theoretical results that have been obtained for the mentioned algorithms. Simultaneously, several prototype sensor nodes that scavenge solar energy have been developed [3, 4, 5]. They perform efficient energy conversion and storage and are able to adapt to changing light conditions. The charging process of a storage device, like e.g. a supercapacitor, by means of a solar cell is however a very non-linear process. The amount of energy that can be harvested depends on various factor like e.g. the voltage level of the storage device and the incident light intensity.

What is needed at this point is an accurate estimation of the usable electrical energy, which is substantially harder than estimating the amount of available solar energy. Only with this capability, the energy optimisation algorithms can be used in practice. This thesis wants to investigate the role of the non-linearities in the energy conversion and the inefficiencies of the energy storing process. Major questions are how accurately the available electrical energy can be predicted and which factors influence the energy efficiency of a scavenger.

To this end, a prototype scavenger that was developed at the University of Bologna [6, 7] will be extensively investigated in this thesis. The "Bologna scavenger", as the scavenger will be called from now on, is based on the architecture of the Everlast energy harvester [4] with some additional features and improvements. The scavenger uses a supercapacitor as storage device and is self-controlled,

which means no active microcontroller is needed to ensure correct operation. The Bologna scavenger's functionality will be demonstrated by its ability to power the BTnode [8]. The BTnode is an autonomous wireless communication and computing platform based on a Bluetooth radio and a microcontroller. It serves as a demonstration platform for research in mobile and ad-hoc connected networks (MANETs) and distributed sensor networks.

The several components of the scavenger's circuit will be discussed with a focus on energy efficiency and predictability of available electrical energy. Also the working principle of the scavenger will be covered since a clear understanding of this principle is needed to fully comprehend the several influences on the energy efficiency. Finally, the extent of the advantage of the Bologna scavenger compared to less complex circuits will be examined.

The following new results are described in this thesis:

- We investigate the characteristics of supercapacitors as energy storage devices by means of measurement. We find that the voltage over the supercapacitor may be a highly unreliable indicator for the currently stored energy. This result contrasts to related work, where the classical formula $\frac{1}{2}CV^2$ has been extensively used to determine and optimize the efficiency of energy scavenging systems.
- A solar energy scavenger based on the Bologna harvester design has been implemented and tested.
- We identify some shortcomings of the Bologna harvester design and make suggestions for improvements. In particular, we point out situations in which MPP tracking does not work properly and measure the sensitivity of the circuit towards temperature changes.
- To test the performance of the Bologna harvester, an indoor test setup has been implemented. By introducing suitable metrics, the efficiency of the harvester is compared with simple designs where solar cell, supercapacitor and sensor node are directly connected without a regulating circuit.

The remainder of this thesis will be structured in the following way. Chapter 2 will give a short overview of the existing techniques that can be used to maximise the energy that can be extracted from a solar cell. It will also discuss advantages and disadvantages of existing energy scavenger prototypes that are different from the Bologna scavenger. Chapter 3 is completely dedicated to the storage device that is used in the majority of the currently existing energy scavengers for sensor nodes, the supercapacitor. The occasionally unexpected behaviour of the supercapacitor and its influence on the performance of an energy scavenger were never before investigated in the context of sensor nodes. Several experiments will be discussed to shed more light on the observed behaviour of the supercapacitor. In Chapter 4, the working principle of the Bologna scavenger is demonstrated and examined. The shortcomings of the scavenger and their resulting effect on its performance will be described.

Chapter 5 contains a comparison between the Bologna scavenger and two very simple energy scavenging circuits. In this chapter, several measurements are used to identify the influences on the energy efficiency and overall performance of the tested circuits. The benefit of the Bologna scavenger in comparison to direct connection implementations will be determined for different circumstances and conditions. Finally, Chapter 6 summarizes and discusses the main findings of this thesis.

Chapter 2

Photovoltaic energy harvesting

The Bologna scavenger harvests solar energy in order to provide power to a sensor node. Energy that is not directly consumed by the sensor node is stored on a supercapacitor to be used during periods of limited available solar energy. The aim of the scavenger circuit is to maximize the power that can be extracted from a solar cell. The Bologna scavenger will be discussed thoroughly in Chapters 4 and 5. This chapter will concisely describe the characteristics of a solar cell and the techniques that can be used to detect the operating point in which the solar cell generates the most power. Finally, some other photovoltaic energy scavengers for sensor nodes will be discussed.

2.1 Solar cell characteristics

A fundamental solar cell element can be represented by its equivalent circuit that is depicted in Figure 2.1. The current source of the solar cell is dependent on the intensity of the incident light while the resistor in parallel with the source represents the internal leakage. The other resistor represents the internal resistance of the cell. In most cases, a solar cell panel consists of multiple fundamental solar cell elements connected in parallel and/or series. Because of the presence of the diode(s), a solar cell has a very specific voltage-current relationship that can be represented as a VI curve. Figure 2.2 depicts an example of such a VI curve together with the related VP curve. The VP curve represents the relationship between the solar cell voltage and its output power for a certain light condition. One can clearly see that the output power of the solar cell is very sensitive to its voltage. Consequently, for the same incident light intensity, the power a solar cell provides can vary significantly.

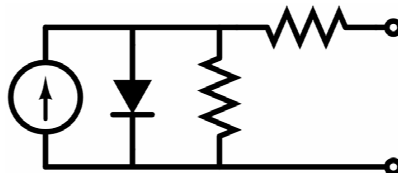


Figure 2.1: Equivalent circuit of a solar cell.

The operation point in which the solar cell provides the maximum power it can generate for a certain light condition, is called the maximum power point (MPP). The current, voltage and power in this point are respectively called maximum power point current (I_{MPP}), voltage (V_{MPP}) and power (P_{MPP}).

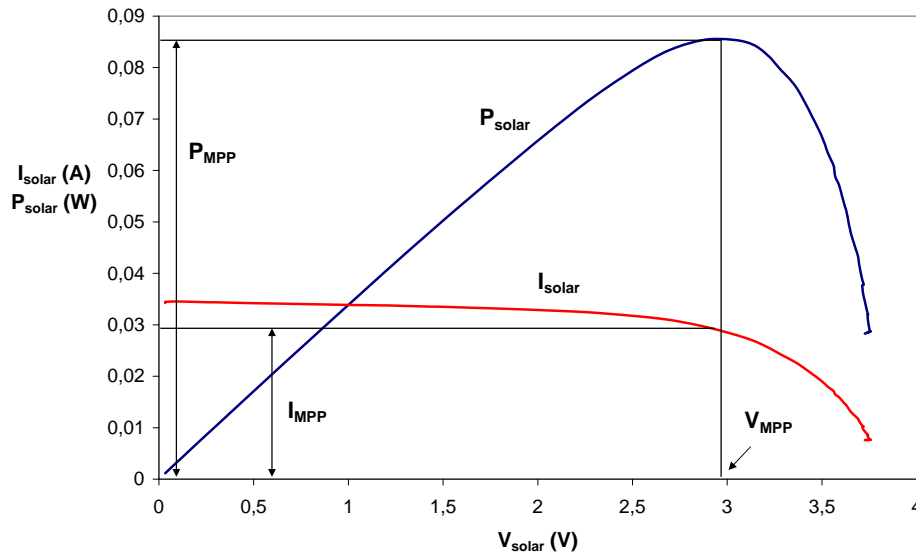


Figure 2.2: VI and VP curve of a solar cell.

2.2 Maximum power point tracking techniques

The last two decades, a lot of work and research has been done in the field of maximum power point tracking techniques [9, 10, 11]. These techniques try to aim for a continuous operation of the solar cell in its maximum power point (MPP) while adapting to varying light conditions. The goal is of course to harvest as much energy as possible from the available solar energy. The next section will give a short overview of the most commonly used maximum power point tracking techniques. The focus will be on the principle behind the MPP estimation and less on the exact method that is used to force the solar cell in this MPP. Section 2.3 will give some examples of how this is done while discussing existing solar energy scavengers for sensor nodes.

2.2.1 Different techniques

Hill-Climbing/Perturb and Observe

Hill-Climbing and perturb and observe (P&O) are very similar and widely spread methods. Hill-Climbing involves a perturbation in the duty ratio of the power converter and P&O a perturbation in the operating voltage of a photovoltaic cell or array. Basically, the methods work as follows. A perturbation is imposed on the circuit and if the perturbation (solar cell voltage increase or decrease) causes the increase of the solar cell power, the direction of the next perturbation is kept the same.

After all, keeping the VP curve of Figure 2.2 in mind, this perturbation will bring the solar cell closer to its MPP. In case the perturbation causes a decrease of the solar cell power, the direction of the next perturbation is reversed. The process is repeated periodically until the MPP is reached. The system then oscillates about the MPP. In most hill-climbing or P&O systems, DSP or microcomputer control is applied although some examples exist with only discrete analog and digital circuitry.

Incremental Conductance

The incremental conductance method is based on the fact that the slope of a photovoltaic power curve is zero at the MPP, positive on the left of the MPP and negative on the right. Through the help of a simple calculation, a DSP or microcontroller periodically checks at which side of the MPP the solar cell operates. Depending on this result, the operating point in which the solar cell is forced is incremented or decremented. This process stops when the MPP has been reached.

Fractional open-circuit voltage

A near linear relationship between V_{MPP} and V_{OC} (= open-circuit voltage) exists, and this under varying irradiance and temperature levels. Since the linear factor depends on the characteristics of the solar cell that is being used, it usually has to be computed beforehand by empirically determining V_{MPP} and V_{OC} for the specific cell at different irradiance and temperature levels. The voltage V_{MPP} can then be calculated based on V_{OC} , which is measured periodically by momentarily shutting down the power converter that is connected to the solar cell. Since the linear relationship is only an approximation, the solar cell rarely operates in its exact MPP. The technique is however very easy and cheap to implement and does not necessarily require DSP or microcontroller control.

Fractional short-circuit current

Fractional I_{SC} (= short-circuit current) stems from the fact that there also exists an approximately linear relationship between I_{SC} and I_{MPP} . Just like in fractional V_{OC} , the linear factor has to be determined for each specific solar cell. Measuring I_{SC} during operation can be problematic. An additional switch usually has to be added to the power converter to periodically short the solar cell to measure the short-circuit current with a current sensor, adding complexity and cost to the system. Using this method, the MPP is never perfectly matched. Some systems periodically sweep the solar cell from open-circuit to short-circuit to update the linear factor, as is also sometimes done in systems that use the fractional V_{OC} technique.

Others

Other methods include fuzzy logic control, neural networks and many other techniques. We won't discuss those but it's certainly important to know which considerations need to be taken into account when selecting a certain technique. This will be discussed in the next section.

2.2.2 Important comparative considerations

Some MPP trackers can be built as circuits with discrete analog and digital components while others require the digital processing power of programmable microcontrollers. The choice between the two different kinds of implementation can be especially important for sensor nodes. If the MPP tracking technique needs control signals from a microcontroller to work correctly, the sensor node cannot go into a sleep mode without stopping the tracking, which is a huge disadvantage. This way, the extra input energy that is harvested because of MPP tracking is offset by a much higher energy consumption of the sensor node.

The cost and complexity of a MPP tracker is an important consideration that certainly influences the choice between analog or digital. The number of sensors that the tracker requires, can be an important factor too. Especially current sensors can increase the cost of a system substantially.

MPP tracking techniques are very common in the world of large-scale solar cells. The extra energy that is consumed by the MPP tracker, is easily offset by the much higher amount of energy that can be harvested from the environment. Sensor nodes are often required to be small and therefore they are powered by small solar cells that generate limited energy. For those cells, the gain in input energy is not always higher than the additional losses that are caused by the MPP tracking operation. Energy consumption of the MPP tracker is therefore a very important design criterion in energy scavengers for sensor nodes.

2.3 Photovoltaic energy scavengers for sensor nodes

Some examples of photovoltaic energy scavengers for sensor nodes, different from the Bologna scavenger, will be discussed in this section. They are all powered by a solar cell and use a supercapacitor as storage device.

2.3.1 Prometheus

An overview of the system architecture of the energy scavenger Prometheus [3] is depicted in Figure 2.3. Prometheus does not perform MPP tracking and connects the solar cell directly to the supercapacitor. This means that especially for low supercapacitor voltages, the solar cell generates much less power than its P_{MPP} . Besides the supercapacitor, Prometheus possesses a second energy buffer, a rechargeable battery. Chapter 3 will discuss supercapacitors extensively and Section 3.2.2 contains a detailed comparison of supercapacitors and batteries. Therefore this section will not pay a lot of attention to the used storage devices.

The aim of the architecture of the Prometheus is an increase of the battery lifetime by reducing the number of charge/discharge cycles. The battery is only used when the voltage of the supercapacitor is too low to power the sensor node. The charging of the battery is done when the supercapacitor is near

to its maximum voltage. The control of the circuit and its switches is performed by the sensor node. Only every hour the energy levels of the supercapacitor and the battery are checked, which reduces the load on the sensor node.

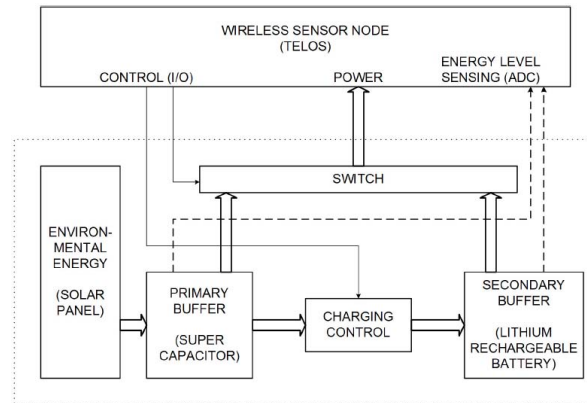


Figure 2.3: System architecture and Prometheus implementation.

2.3.2 Ambimax

The Ambimax [5] (Figure 2.4) is an autonomous energy harvesting platform for multi-supply wireless sensor nodes. "Autonomous" refers to the fact that Ambimax does not need intervention or control from a microcontroller. The Ambimax supports different power sources and does not only harvest solar energy but e.g. also wind energy. Each power source has its own harvesting subsystem that charges a separate supercapacitor. The supercapacitors of the different power sources form a reservoir supercapacitor array (Figure 2.5). The energy that is stored in this array is used to charge a battery and to supply power to the sensor node. The battery is only used as a supply when the supercapacitor array voltage is below the minimum allowed input voltage of the sensor node. The individual supercapacitors are separated from each other and the load by a diode. The supercapacitor with the highest voltage is then used as power supply.

The circuit consists of discrete digital and analog components such as comparators, switches and a boost DC/DC converter. This converter is normally used to convert the DC voltage of a battery to the desired supply voltage of a circuit. In this case however, the comparator is used as part of a MPP tracker. The Ambimax uses a variant of the fractional V_{OC} technique as it assumes a linear relationship between the output of a light sensor and the V_{MPP} of the solar cell. The complete working principle will not be explained. Basically, the voltage of the solar cell is forced around its estimated MPP by a comparator that compares the voltage-divided light sensor output and the voltage-divided solar cell voltage. The comparator output determines if the boost converter is turned on or off. In one case the solar cell voltage decreases, in the other the cell's voltage increases, resulting in a hysteresis window around the estimated V_{MPP} to which the solar cell voltage is confined.

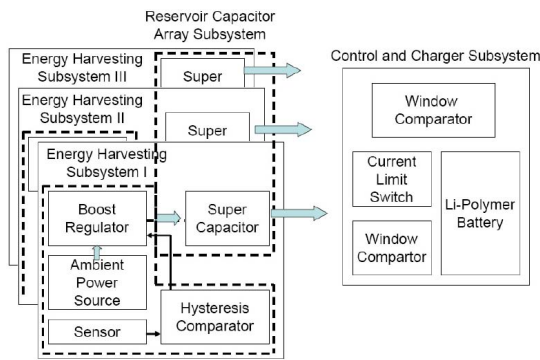


Figure 2.4: Architecture of Ambimax platform

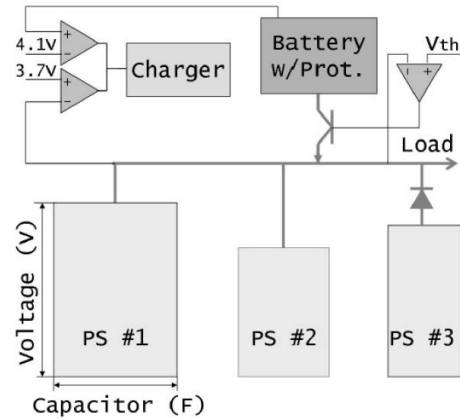


Figure 2.5: Reservoir supercapacitor array

2.3.3 Everlast

The Everlast [4] (Figure 2.6) is a photovoltaic energy scavenger with an architecture that is very similar to the Bologna scavenger's architecture. In contrast to the Bologna scavenger however, the Everlast is not self-controlled since the control of all its components is done by the sensor node. How the solar cell is forced in its MPP is completely the same as for the Bologna scavenger, so this will not be discussed here. The Everlast has however more flexibility in how the maximum power point can be detected. A digital potentiometer, controlled by the microcontroller unit (MCU) on the sensor node, can be used to measure the complete VI curve of the solar cell during a MPP sweep. During this sweep, the solar cell is disconnected from the harvester and connected via the potentiometer to ground, which means that solar energy is lost. While changing the value of the potentiometer, the solar cell voltage and current change too, according to the VI curve. The different solar cell voltage - solar cell current combinations are sampled by sensors and this data is then used to calculate V_{MPP} . To reduce the duration of a sweep, the microcontroller can opt for a different method of MPP tracking. By choosing the lowest value of the potentiometer, the short-circuit current can be measured and the fractional short-circuit current technique can be applied. Similarly, the potentiometer can be configured to its highest value to measure the open-circuit voltage for the fractional open-circuit voltage technique. This way, only one measurement needs to be done, reducing the time during which solar energy cannot be harvested. The sweep is done periodically to adapt to changing light conditions.

The three described photovoltaic energy scavengers are together with the Bologna scavenger among the most recent energy scavenger designs for sensor nodes. Their individual working principles may be different from the Bologna scavenger's principle, but their main components, the solar cell and the supercapacitor, are the same. Consequently, the results of this thesis will be useful for other energy scavengers too. The behaviour of the solar cell and the supercapacitor and the influences on their performance are for all scavengers hugely important.

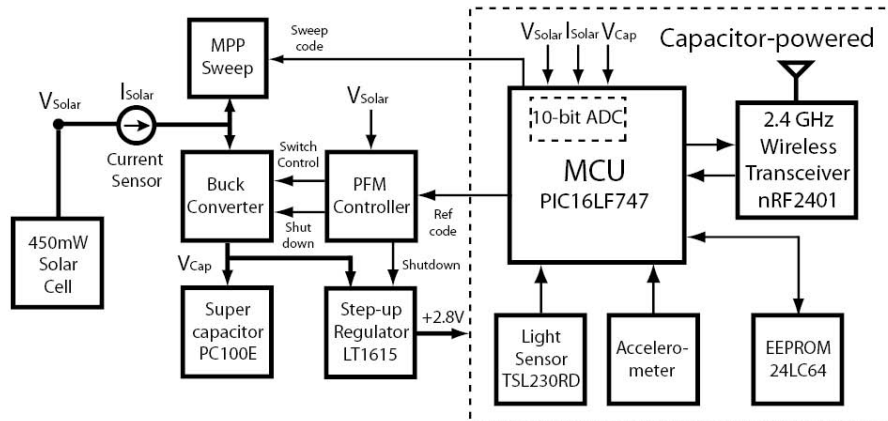


Figure 2.6: Everlast system block diagram.

Chapter 3

Supercapacitors and their unregular behaviour

3.1 Introduction

Section 2.3 demonstrated that a lot of the most recent energy harvesting systems for sensor nodes have opted for supercapacitors as at least one of the used energy storages. The papers presenting those systems always assume a very simple and regular supercapacitor behaviour that is identical to the behaviour of the lower-value capacitors that can be found in most electronic circuits. The energy content of a supercapacitor is assumed to follow Formula 3.1 and the internal losses are believed to be negligible. Even the datasheets of the used supercapacitors do not cover any unregular behaviour that is different from normal lower-value capacitors.

$$E = \frac{CV^2}{2} \quad (3.1)$$

Early experiments showed us however that supercapacitors do demonstrate unregular behaviour under certain conditions. In the context of sensor nodes, this phenomenon has not been noticed or investigated before. The validity of the mentioned energy content formula is however of substantial importance to several applications. In papers like [3] and [6], the supercapacitor voltage and Formula 3.1 are used to estimate the performance of a system. An accurate representation of the energy content of a supercapacitor is equally important to high-level system optimization algorithms such as described in [1], that use the amount of stored energy as prime input.

This chapter will investigate the behaviour of supercapacitors, emphasizing energy and energy efficiency under different conditions. The validity of the energy content formula will be checked. Before discussing my own measurement results however, Section 3.2 will give an overview of the current knowledge about supercapacitors.

3.2 General discussion

3.2.1 Principles

Supercapacitors are energy-storage devices that are also known as ultracapacitors or EDLCs (Electrochemical Double Layer Capacitors). Supercapacitors store energy in a similar way as conventional capacitors. The charges do however not accumulate on two conductors but at the interface between the surface of a conductor and an electrolytic solution. The accumulated charges form an electric double-layer, the separation of each layer being of the order of a few Angstroms. The capacitance of a supercapacitor can be obtained through the double-layer model proposed by Helmholtz in 1853 [12, 13]. One layer is formed on the charged electrode while the other layer consists of ions in the electrolyte.

Gouy introduced in 1910 random thermal motion, which led him to consider a space distribution of the ionic charge in the electrolyte (Figure 3.1). This is known today as diffused layer. This new model explained the voltage dependency of the electric double-layer capacitance. The mathematical formulation of the Gouy diffused layer, established by Chapman in 1913, over-evaluated however the double-layer capacitance.

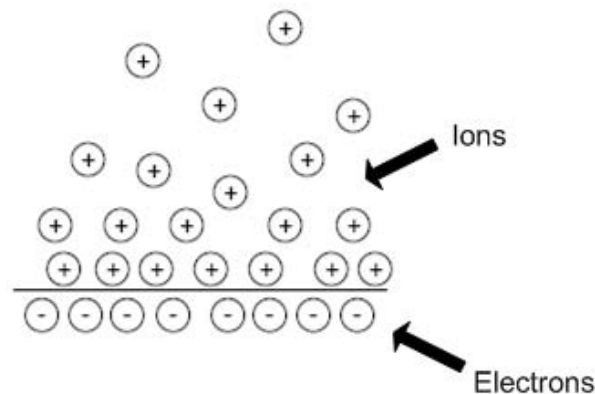


Figure 3.1: The Gouy-Chapman model.

Stern improved in 1924 the Gouy and Chapman theory, first by introducing dimensions of ions and solvent molecules, and second by dividing the space charge in two distinct zones : a compact layer, constituted of adsorbed ions at the electrode surface, and the diffused layer as defined by Gouy and Chapman (Figure 3.2). The capacitance C of the electric double-layer was therefore represented by a series connection of a capacitance C_c , linked to the compact layer, and the capacitance C_d , linked to the diffused layer (Formula 3.2).

$$\frac{1}{C} = \frac{1}{C_c} + \frac{1}{C_d} \quad (3.2)$$

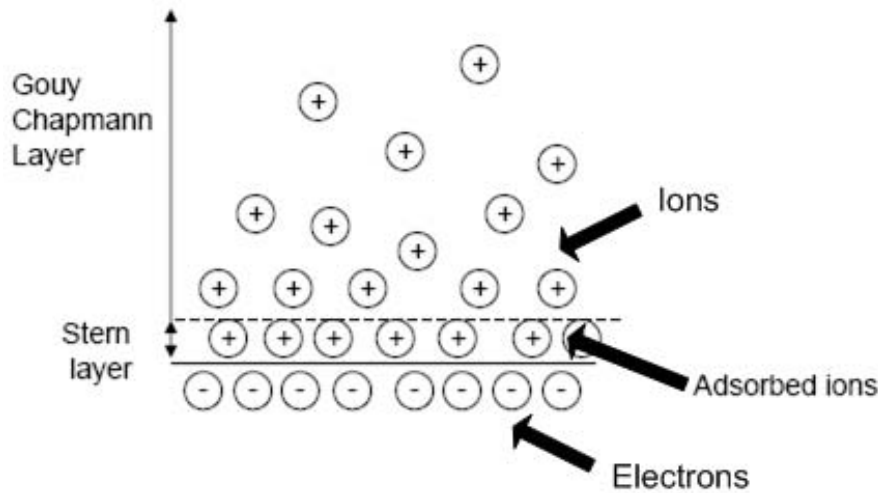


Figure 3.2: The Stern model.

Supercapacitor cells consist of two electrodes to allow a potential to be applied across the cell, and there are therefore two double-layers present, one at each electrode/electrolyte interface (see Figure 3.3) [14, 15, 16]. An ion-permeable separator is placed between the electrodes in order to prevent electrical contact, but still allows ions from the electrolyte to pass through. The electrodes are made of high effective surface-area materials - such as metal oxide, conducting polymers, porous carbon (= activated carbon), carbon aerogels or carbon nanotubes - in order to maximise the surface-area of the double-layer. High energy densities are therefore achievable in supercapacitors due to their high specific capacitance (in F/cm^2), attained because of a high electrode/electrolyte interface surface-area and a small charge layer separation of atomic dimensions. Figure 3.4 shows a cross-section of a supercapacitor. The metal-foil electrode acts as the current collector that is connected to a very porous carbon electrode. These carbon electrodes are surrounded by electrolyte. The electrolyte is an ionic solution with a solvent that consists of polar molecules. These polar molecules are not shown in Figure 3.4 but they form the dielectric layer between electrode and ions. Figure 3.5 indicates how the solvent molecules are distributed.

The operating voltage is controlled by the breakdown or dissociation voltages of the solvents. Organic electrolytes have a breakdown voltage of 2.5 V to 3 V. An aqueous electrolyte offers lower internal resistance but limits the voltage to one volt. Available supercapacitor values range from hundreds of millifarads (mF) to 3000 F.

In addition to the capacitance that arises from the separation of charge in the double-layer, a contribution to capacitance can be made from reactions that can occur on the surface of the electrode: Pseudocapacitance. Pseudocapacitance arises from reversible Faradaic reactions (heterogeneous charge-transfer reactions) occurring at the electrode, and is denoted as "pseudo"-capacitance in order to differentiate it from electrostatic capacitance. The charge transfer that takes place in these reactions is voltage dependent, so a capacitive phenomenon occurs. There are two types of reactions that can

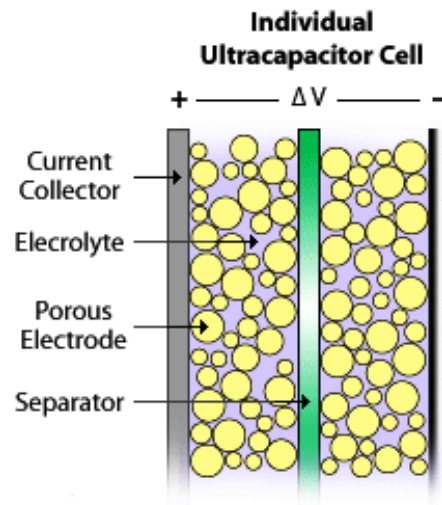


Figure 3.3: An individual supercapacitor cell.

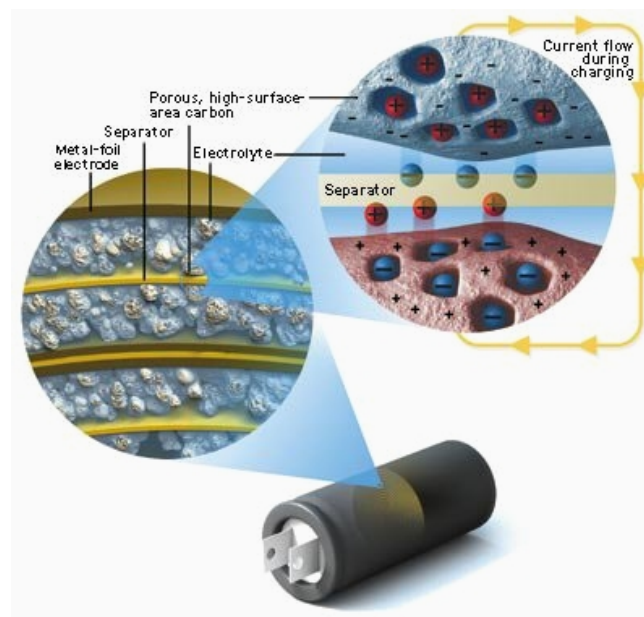


Figure 3.4: A cross-section of a supercapacitor.

involve a charge transfer that is voltage dependent: redox reactions and ion sorption reactions. Pseudocapacitance further improves the achievable capacitance of supercapacitors. Most electrode materials exhibit this phenomenon, especially transition metal oxides (ruthenium or iridium) and electric conducting polymers. The pseudocapacitance of a carbon electrode device can be enhanced by treatment of the activated carbons.

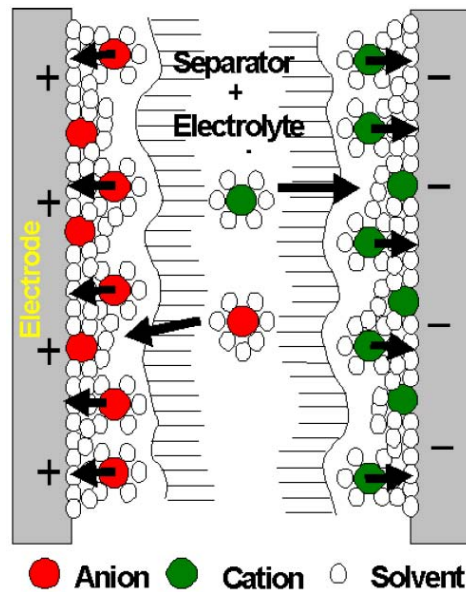


Figure 3.5: A supercapacitor image indicating the distribution of the solvent's molecules.

3.2.2 Supercapacitors versus batteries

Figure 3.6 shows a Ragone chart that allows to compare the performance of various energy storing devices. On such a chart the values of energy density (in Wh/kg) are plotted versus power density (in W/kg). Conceptually, the vertical axis describes how much energy is available, while the horizontal axis shows how quickly that energy can be delivered. Supercapacitors offer a much higher power density than batteries because of their low equivalent series resistance (ESR). This low ESR allows them to discharge quickly using enormous currents (up to 1000 A for high capacitance values). Compared to batteries, they have however a low energy density which makes them less suitable as single energy storing device for high power applications.

Even though supercapacitors have a lower energy density and consequently are bulkier and heavier than an equivalent battery, they become more common as replacements for batteries for specific applications (see 3.2.3). Their advantages over batteries are:

- *Much longer lifetime*

A typical supercapacitor offers more than half a million charge cycles and a 10-year operational lifetime until the capacity is reduced by only 20%. They require very little maintenance. Since a battery depends on a chemical reaction between its electrolyte and electrodes, each charge/discharge cycle will cause both the active materials and the electrolyte to deteriorate, which means that its useful lifetime, when the full battery capacity is employed, is normally measured in thousands of cycles (although Ni-MH or Li-ion batteries can achieve several hundred thousand cycles when used at a depth of discharge of just a few per cent of capacity). In contrast, a carbon type supercapacitor is in theory a pure electrostatic device which stores energy with no physical

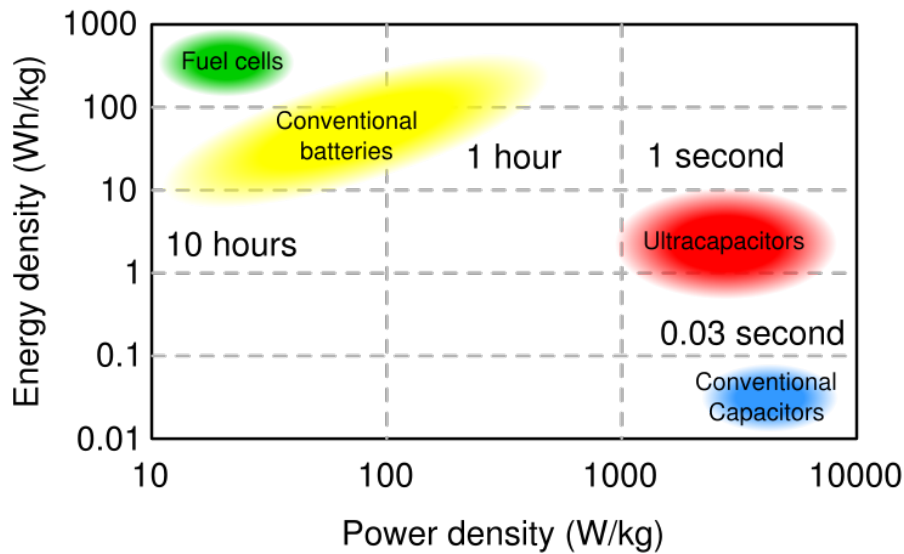


Figure 3.6: Ragone chart showing energy density vs. power density for various energy storing devices

changes taking place, which means that we might expect it to last forever. In practice, in the same way that chemical batteries consume water over time due to electrolysis of the solvent, the same process can occur with the supercapacitor's organic electrolyte, albeit to a much smaller degree.

- *High efficiency*

Supercapacitors are highly efficient. They achieve cycle efficiencies up to 97% for a complete charge/discharge cycle. Sections 3.3.3 and 3.3.4 will cover cycle efficiencies extensively based on own measurement results.

- *Higher power density*

They can discharge in matters of milliseconds and are capable of producing enormous currents.

- *Fast and simple charging*

Batteries take time to charge and discharge because the process involves chemical reactions with non-instantaneous rates. Different battery types need different - sometimes complex - ways of charging. Often external charging hardware is necessary to achieve the maximum obtainable charging efficiency.

- *No hazard to the environment*

Supercapacitors do not contain hazardous substances that can damage the environment.

- *Low operating temperature*

Since the rate of chemical reactions taking place in a battery are temperature dependent, a battery's performance will deteriorate at extremes of temperature. For example, a lead-acid

battery can be expected to lose approximately one percent of its capacity and power for every degree Celsius drop in temperature. Since there are no complicated chemical reactions taking place in a supercapacitor during normal operation and combined with the choice of a highly conductive organic electrolyte, its performance remains completely unaffected over a very wide range of temperatures from +70°C down to -20°C[17]. Below this temperature the conductivity of the organic electrolyte will start to limit the performance of the supercapacitor. But even at -40°C half the power is still available.

There are however also some other not yet mentioned disadvantages of supercapacitors that need to be taken into account when compared with batteries:

- *Lower energy density*

To prevent too bulky supercap configurations, a supercapacitor is only recommendable as stand-alone energy storing device for low power applications.

- *Voltage is highly dependent on stored energy*

Whereas the electro-chemical battery delivers a fairly steady voltage in the usable energy spectrum, the voltage of the supercapacitor approximately follows the stored energy according to Formula 3.1. This is in contrast with the customary flat voltage curve characterized by most chemical batteries. Often applications require a certain voltage range as input and once the supercapacitor is below the minimum allowed voltage, the remaining charge turns unusable. A DC-DC converter can be used to increase the voltage range but this option adds costs and introduces inefficiencies of 10 to 15 percent.

- *Low breakdown voltage*

Applications that demand higher voltages than the rather low breakdown voltages of supercapacitors (1V to 3V) need series configurations [18]. If more than three or four capacitors are connected in series, voltage balancing must be used to prevent any cell from reaching over-voltage. Since supercapacitors with the same published capacitance values and of the same manufacturer are not completely identical, the voltage over the series connection is not always proportionally distributed (see Section 3.3.2). This can cause a breakdown of one supercapacitor belonging to the series configuration much earlier than expected. Voltage balancing circuitry adds extra costs to the system.

- *High self-discharge*

The self-discharge is considerably higher than that of an electrochemical battery. The leakage of a supercapacitor is voltage-dependent and can be decreased by using a series connection of multiple supercapacitors. This reduces however the available capacitance. Leakage will be further investigated in Section 3.3.2.

3.2.3 Current applications of supercapacitors

Electrical vehicles (EV)

In electrical vehicle applications, supercapacitors permit faster acceleration, increased range, and extend battery life by freeing it from stressful high-power tasks [19]. In addition, supercapacitor technology now can do load-leveling to extend the life of EV batteries and provide the high power essential for EV acceleration. For example, a vehicle might use this power burst to accelerate and climb a steep hill. Supercapacitors also can absorb regenerative braking energy and thus limit the otherwise very high charging current to the battery. One should keep in mind that while supercapacitors can be used to provide the increased range and short term power, it is at the cost of considerable added weight and bulk of the system. This is weighed against the advantages of using higher capacity batteries.

Electric vehicle applications are one of the many system applications that require that capacitors are connected together, in series and/or parallel combinations, to form a "bank" with a specific voltage and capacitance rating. As mentioned in Section 3.2.2, voltage balancing is recommended for such configurations and is often included in the bank circuitry. Figure 3.7 shows a 54 V/175 F NESSCAP ultracapacitor bank module that can be used for 42 V vehicle applications.



Figure 3.7: A 54V/175F NESSCAP ultracapacitor bank module

UPS applications

Supercapacitors are used as power back-up in UPS (Uninterruptible Power Supply) applications. By combining a capacitor with a battery-based uninterruptible power supply system, the life of the batteries can be extended. The batteries provide power only during the longer interruptions, reducing the peak loads on the battery and permitting the use of smaller batteries. In addition, supercapacitors can

serve as a load-leveling function by absorbing power surges and spikes. This ensures clean quality power which is essential for precision high-tech equipment.

Memory backup applications

Capacitors are extensively used as power back-up for memory functions in a wide range of consumer products such as mobile phones, laptops and radio tuners. Small supercapacitors defend against data loss during short-period power outages or, in the case of portable devices, during battery replacement. For this, an supercapacitor is superior to a battery because it's less expensive and requires no replacement during the device's lifetime.

Quick-charge applications

Supercapacitors charge in seconds whereas batteries often require hours, thus potentially benefiting quick-charge applications. Wireless power tools employing an supercapacitor can be charged just before use. Moving toys, such as miniature racing cars, also benefit from the fast-charge properties of the supercapacitor.

Peak pulse power

Supercapacitors are also used in pulsed applications to share the load and for providing peak power assistance in products or devices using mechanical actuators such as digital cameras. This can help to reduce the duty cycle on the battery to prolong battery life.

Primary power source for small and low power devices

Thanks to recent evolutions that have led to an increase in energy and power density is the supercapacitor more and more considered as primary power source for low power devices such as sensor nodes. Supercapacitors will be discussed in this capacity for the remainder of this thesis.

Although some supercapacitor applications, such as memory backup, are already in widespread use, many of the applications just discussed are still in the initial phase of adoption. Because of their nature, supercapacitors can be used in a very wide range of applications and the overview given in this section has certainly not covered all the applications supercapacitors are investigated for.

3.2.4 Modelling

Significance of supercapacitor models for this thesis

Papers presenting energy harvesters for sensor nodes often do not mention the specific and sometimes unregular behaviour of supercapacitors. This however does not mean that there hasn't been scientific research in this field. Especially in the area of power electronics, much effort has been done to obtain accurate supercapacitor models. The available literature focuses however on the modelling

of very high capacitance supercapacitors with values of 500 F up to 2000 F. Charging currents of 100 A are not at all exceptional for the applications that use this kind of supercapacitor. In contrast, energy harvesters for sensor nodes are low power circuits that handle much smaller input and output currents. Because of size restrictions and low available input power, much smaller capacitance values are used (50 F and less). The models that will be discussed in this section are based on the physical structure of supercapacitors and there is no reason to assume that these models would be less valid for lower capacitance values. This thesis does not have the intention to obtain the model parameters for the supercapacitors used in energy harvesters for sensor nodes. The models can however help to understand how a supercapacitor behaves in specific situations and they are therefore definitely worth mentioning. The models will be the basis for a qualitative analysis and interpretation of the observed behaviour during own measurements (see Section 3.3).

Supercapacitor models

Electrical charge is stored in the double-layer of a supercapacitor when an external voltage is applied. The flow of charges across the interface is not an instantaneous process. It depends on the ion mobility, environmental conditions and several other factors. In addition, the exchange of electrical charges between the two electrodes is followed by a series of charge distribution processes and dipole orientations that can take a considerably long time. To represent the combination of many processes with different time behaviour, a model consisting of an infinite number of parallel branches has been proposed [20, 21]. Each branch is composed of a resistor and a capacitor in series. The time constant of each branch is longer with respect to the previous one producing a general device with a complicated internal behavior. This structure is presented in Figure 3.8.

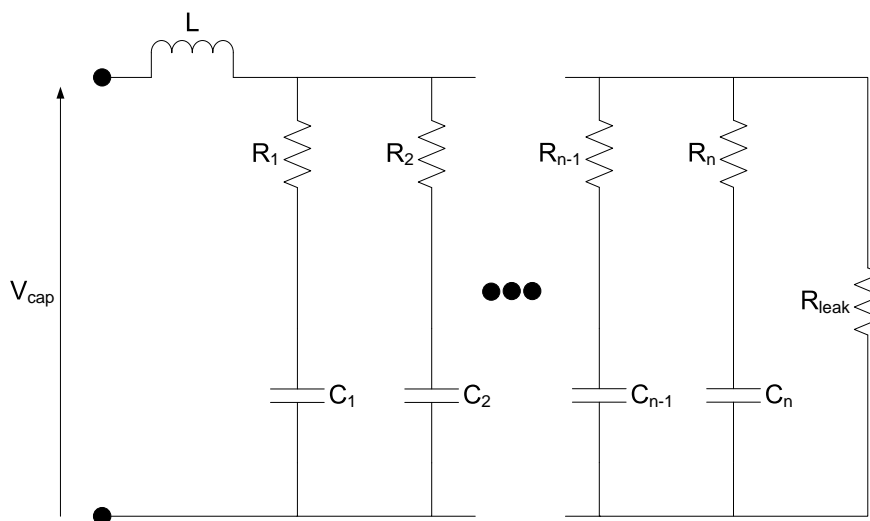


Figure 3.8: Supercapacitor model based on physical structure.

This model also takes the self-discharge process that occurs in a supercapacitor into account. This phe-

nomenon is a result of electrochemical reactions occurring across the electrode-electrolyte interface when charge separation is present. The self-discharge or leakage is represented by resistor R_{leak} . This resistor is in parallel with the different time constant branches and allows to model the internally lost charge in the double-layer that cannot be recovered. One can also notice a series inductance connected to all different branches. This inductance embodies all the inductive effects in the supercapacitor, e.g. caused by rolled up electrodes.

The model presented in Figure 3.8 does not yet take the already mentioned (Section 3.2.1) voltage-dependency of the capacitance into account. The infinite number of branches render the extraction of the model parameters and eventual simulations using the model impossible. Although some internal processes may have time constants of several hours, the scope of power electronics is often restricted to 30 minutes because of relatively short time or high power applications. Therefore the authors opted for a simplified model consisting of three branches with time constants in the order of respectively a few seconds, a few minutes and tens of minutes. The resulting model is shown in Figure 3.9. The first branch or 'immediate' branch contains a constant and a voltage-dependent capacitor. The second branch is called the 'delayed' branch while the third is named 'long term' branch. This model is based on assumptions typical for power electronics and one should be cautious when using the model for other applications.

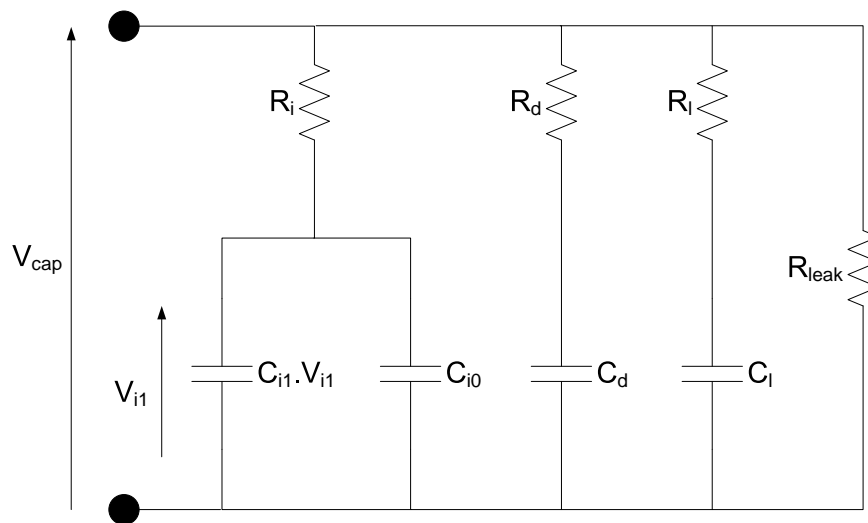


Figure 3.9: Supercapacitor model

Less important for the relatively long term processes present in energy harvesters for sensor nodes is a model that includes a transmission line [22]. This transmission line is placed in front of the model in Figure 3.9 and represents the very short term and high frequency effects. The idea of including a transmission line stems from the representation of an electrode pore as a sequence of elementary transmission line components (see Figures 3.10 and 3.11). In mathematical estimations of the double-layer capacitive effects, straight, cylindrical pores of uniform diameter and a perfectly conducting

electrode are assumed. The transmission line models a distributed double-layer capacitance and a distributed electrolyte resistance that extends into the depth of the pore.

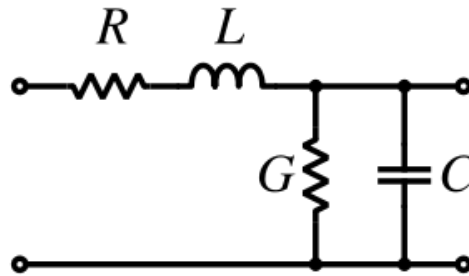


Figure 3.10: Schematic representation of the elementary component of a transmission line.

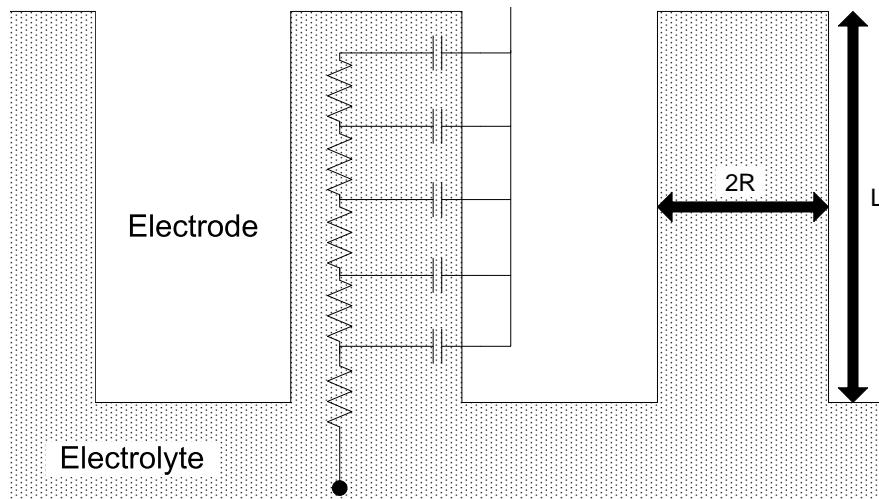


Figure 3.11: An electrode pore as a sequence of elementary transmission line elements.

3.3 Measurement results

3.3.1 Measurement setup

As mentioned before, this thesis does not have the intention to extract the model parameters for the used supercapacitors. The main goal - concerning supercapacitors - is the investigation of their influence on energy and energy efficiencies of a complete energy harvesting system. Chapter 5 will do an extensive comparison of a limited number of different harvesting circuits. This comparison will also involve the efficiency performance of the used supercapacitors. First however, the remainder of this chapter will investigate supercapacitors in a very simple and isolated test setup. This allowed to test the supercapacitors for charge/discharge patterns that weren't achievable using the tested harvesting

circuits from Chapter 5. These tests are valuable for energy harvesters that exhibit other charge/discharge patterns than the harvesters investigated in this thesis.

Figure 3.12 gives an overview of the used test setup. The supercapacitor is charged by a normal DC voltage power source through two resistors. The charge resistor (R_{charge}) is carefully chosen to manipulate the time constant of the charging process. The shunt resistor (R_{shunt}) is a small and very accurate resistor that is used to measure currents based on the voltage drop over the shunt (V_{shunt}). For some experiments the internal shunt of a DDM (digital multimeter) was used, for others an external shunt [23] was employed. The setup for discharging is equally modest. The supercapacitor discharges through a discharge resistor ($R_{discharge}$) and a shunt (R_{shunt}). The discharge resistor determines the time constant of the discharging process.

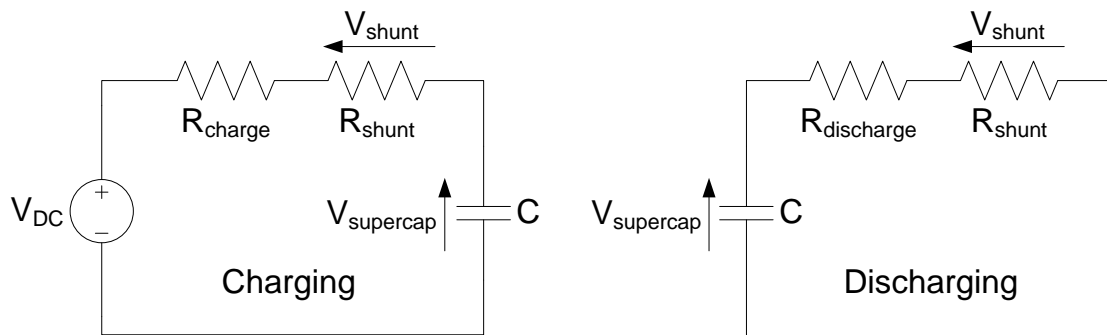


Figure 3.12: Supercapacitor test setup.

The supercapacitors used in all experiments are manufactured by Cooper-Bussmann. We opted for their aerogel supercapacitor B series [24] (Table 3.1, Figure 3.13) and purchased 22 F, 33 F and 50 F samples. The choice for this capacitance range will be explained in Section 4.2.3. Because of time constraints, only one capacitance value was adopted for the majority of the tests. Section 3.3.2 will compare the three tested samples based on their leakage performance. This comparison was a major consideration in the choice of the used capacitance value.

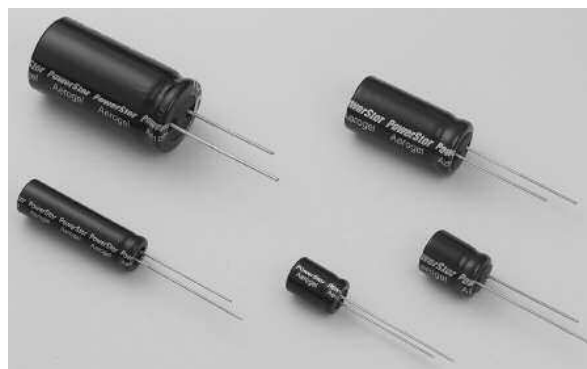


Figure 3.13: Cooper-Bussmann supercapacitor B series.

SPECIFICATIONS	
Working Voltage	2.5 volts
Surge Voltage	3.0 volts
Nominal Capacitance Range	0.22 to 100 F
Capacitance Tolerance	-20% to +80% (20°C)
Operating Temperature Range	-25°C to 70°C

Table 3.1: Cooper-Bussmann supercapacitor B series specifications.

3.3.2 Leakage

Supercapacitors experience several charge distribution processes with different time constants (see Section 3.2.4), even in isolated and disconnected state. This makes it difficult to identify the process that is responsible for a certain increase or decrease in voltage. After just being charged for a short period, a disconnected supercapacitor will exhibit a decreasing voltage. This decrease is caused by a charge distribution from the fast branches to the slow ones - keeping the models of Section 3.2.4 in mind. After all, the fast branches are more easily charged and will have a higher voltage over their capacitors at the end of charging. At this point self-discharging is also taking place. It is however impossible to say which proportion of the voltage decrease can be attributed to which process. Therefore, a specific method has to be used to identify leakage without occurrence of charge distribution.

The supercapacitors in the following experiments were all charged for more than 24 hours by a voltage source. This long charging period enables the supercapacitor to bring the capacitors of all its branches to the same voltage. In this way, charge distribution during the experiment is prevented as no charge will be transferred from one branch to another. One can then safely assume that every voltage decrease is solely caused by internal leakage. Figure 3.14 shows the results of such an experiment. The voltages over three pre-charged supercapacitors were tracked for over 50 hours. The graph clearly shows a difference in leakage performance for the three different capacitance values. Especially the 33 F supercapacitor demonstrates dissatisfying behaviour, losing more than 25% of its initial voltage. Figure 3.15(a) shows the evolution of the energy content of the supercapacitors during the same experiment. These energy values are calculated using Formula 3.1. The 22 F supercapacitor experiences the lowest energy loss (12.25 J). Although the voltage decrease for the 50 F was not very different from the voltage decrease for the 22 F, the 50F capacitor suffers a much higher energy loss (37.8 J) because of its higher capacitance value. The 33 F supercapacitor is even worse with a loss of 43.59 J. Figure 3.15(b) displays the normalized energy content of the tested supercapacitors, with the maximum energy content of the respective supercapacitors as references. The 22 F supercapacitor again emerges as the best performing supercapacitor.

The used energy content formula is not yet checked for its validity but it should give an indication of how much energy is lost through leakage. Based on these results, the 22 F supercapacitor was chosen

for all the energy harvesting experiments in this thesis. In general, one can conclude that leakage is voltage dependent with more leakage loss for a higher voltage. Especially close to the maximum allowed voltage (2.5 V), the leakage is significant.

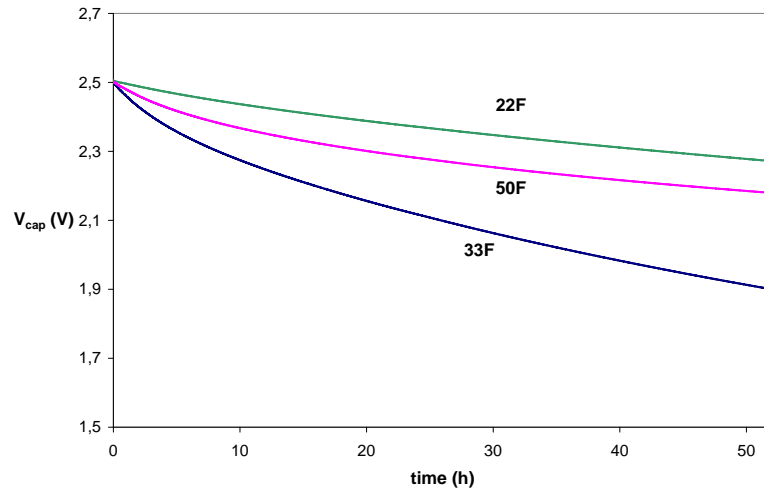


Figure 3.14: Leakage phenomenon in a single supercapacitor: voltage.

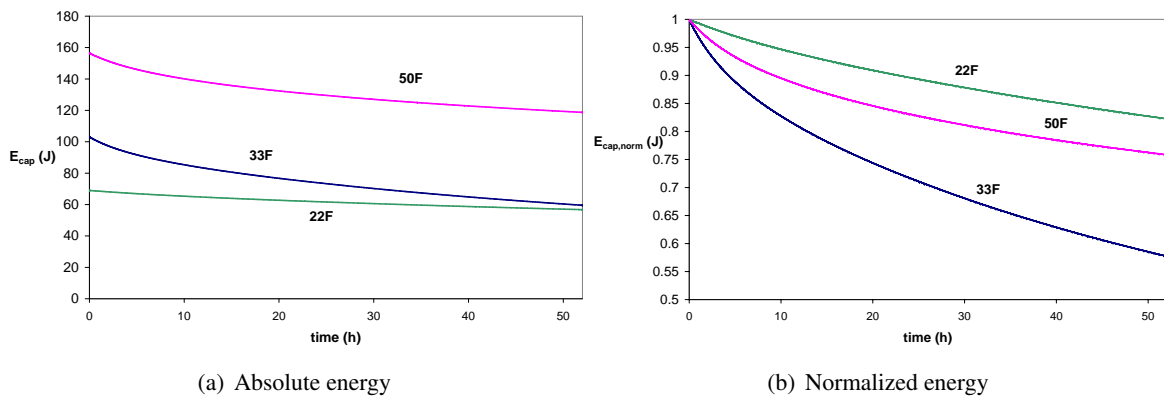


Figure 3.15: Leakage phenomenon in a single supercapacitor: energy content.

The same experiment was done for a series connection of two identical supercapacitors (Figure 3.16). In this way, for the same overall voltage, the single supercapacitors experience a lower voltage with lower leakage as a consequence. The series connection also allows the overall voltage to be higher than the maximum allowed voltage of a single supercapacitor. Therefore, the series configurations were pre-charged to 3.3 V (= the input voltage of the BTnode, normally provided by a step-up DC/DC converter). The results are shown in Figures 3.17, 3.18(a) and 3.18(b). The 22 F series configuration performs best in terms of absolute energy loss while the 50 F series configuration has the upper hand in terms of normalized energy loss. Compared to the single supercapacitor experiment, the energy losses are as expected significantly lower. A series connection halves the available capacitance but

also allows a higher voltage to be applied. As a result, the energy content at the beginning of the experiment - which is the maximum stored energy - is not that different for the single capacitor and the series connection.

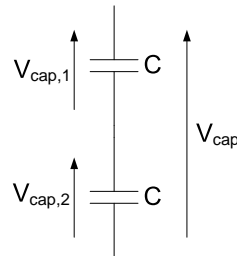


Figure 3.16: Series connection of two identical supercapacitors.

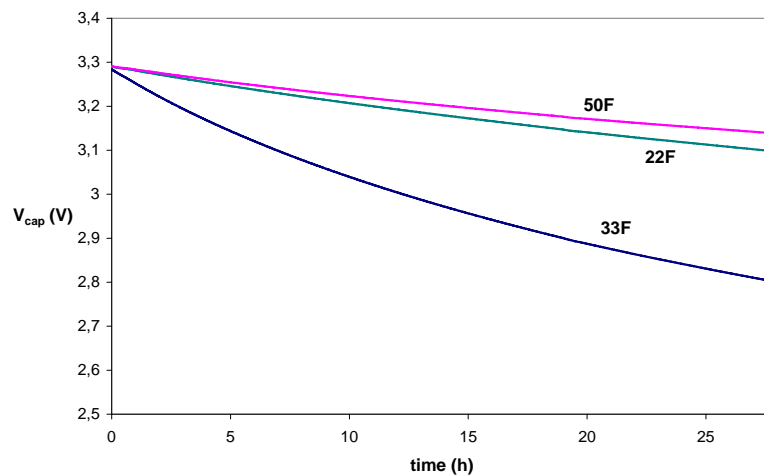


Figure 3.17: Leakage phenomenon in a series connection of two supercapacitors: voltage.

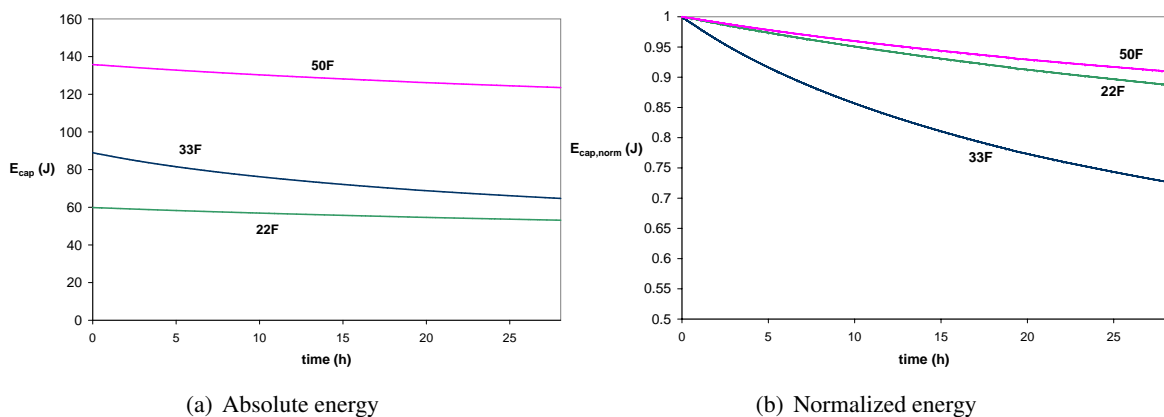


Figure 3.18: Leakage phenomenon in a series connection of two supercapacitors: energy content.

Section 3.2.2 already mentioned that supercapacitors with identical catalogued capacitance values not always act in a perfect identical way, e.g. because of slightly different conditions during manufacturing. Therefore, voltage balancing circuits are recommended for series configurations of three supercapacitors or more [18]. This phenomenon is also demonstrated in Tables 3.2 and 3.3. Table 3.2 shows how the total voltage V_{cap} was distributed over the two single capacitors of the series configuration at the beginning of the last experiment. An equal voltage distribution can only be seen for the 33 F series configuration. Table 3.3 presents the same voltages at the end of the experiment. Even the 33 F series configuration has now unequally distributed voltages, indicating the difference in leakage for the two single 33 F supercapacitors.

	22F	33F	50F
$V_{cap,1}$ (V)	1,76	1,64	1,56
$V_{cap,2}$ (V)	1,53	1,64	1,74
V_{cap} (V)	3,29	3,28	3,29

Table 3.2: Voltage distribution over the series connection: start of the experiment.

	22F	33F	50F
$V_{cap,1}$ (V)	1,68	1,43	1,47
$V_{cap,2}$ (V)	1,42	1,37	1,67
V_{cap} (V)	3,10	2,80	3,14

Table 3.3: Voltage distribution over the series connection: end of the experiment.

3.3.3 Single cycle experiments

Quick/slow charging combined with quick/slow discharging

As first experiments, single charge/discharge cycles between 1 V and 2.5 V were performed. Although any voltage interval could have been chosen for the first experiments, the upper and lower boundaries were not completely arbitrary. The lower boundary of 1V equals the average minimum input of a DC/DC converter (actual minimum depends on required output power and consequently the load). A DC/DC converter is in most energy harvesters the first component after the supercapacitor. The upper boundary of 2.5 V is the maximum allowed voltage over the supercapacitor preventing breakdown of the electrolyte. Charging and discharging resistors were chosen in such a way that one cycle would take about half an hour, as it seemed preferable to use cycles that would not be very different from cycles that could occur in energy harvesters. For the charge resistor, two resistance values were selected, one for quick and one for slow charging. Similarly, for the discharge resistor, two values were selected. The used resistance values are shown in Table 3.4. The voltage source used during charging was fixed at 2.7 V.

	Quick	Slow
charge resistor	4 Ω	10 Ω
discharge resistor	15 Ω	33 Ω

Table 3.4: Used resistance values for the charge and the discharge resistor.

The charge/discharge cycle did not only consist of a charging and a discharging phase. To be able to visualize the internal charge distribution processes of the supercap, a delay period of 10 minutes was inserted in between the charging and discharging interval. During this delay, the charged supercapacitor was kept isolated and disconnected.

During the experiments, the voltage over the supercapacitor and the current entering it were constantly tracked with a sample rate of 1 second. These values were multiplied to estimate the average power entering - or leaving - the supercapacitor during each sample period. The graphs showing the results of the described experiments always include two different plots, denoted as E and E_{form} . The energy E_{form} represents the energy content of the supercapacitor based on its voltage, using Formula 3.3.

$$E = \frac{CV^2}{2} \quad (3.3)$$

The energy E , on the other hand, is based on the measured power entering or leaving the supercap. Its starting value is the same as for E_{form} . The next values follow however Formula 3.4.

$$\begin{aligned} E(n+1) &= E(n) + P(n+1) \cdot 1s \\ &= E(n) + I_{cap}(n+1) \cdot V_{cap}(n+1) \cdot 1s \end{aligned} \quad (3.4)$$

The sample period equals 1 second and therefore the average power during one sample period can be interpreted as the energy entering or leaving the supercapacitor during this period. E basically represents the energy stored in the supercapacitor assuming that its starting value was correct and that no internal losses occur.

Before going to the actual measurement results, the definition of cycle efficiency is clarified (Formula 3.5).

$$\eta_{cycle} = \frac{E_{out}}{E_{in}} \cdot 100 \quad (3.5)$$

The energy E_{in} is the total energy provided to the supercapacitor during charging, while E_{out} represents the total energy delivered by the supercapacitor during discharging. Because of its definition, the plot of E allows to easily recognise E_{in} and E_{out} , as is shown in Figure 3.19. This Figure reveals the results of the first experiment, which was a quick charging - slow discharging combination.

For this first combination, two graphs are provided (see also Figure 3.20). The only difference between the two mentioned graphs is the time during which the supercapacitor had been pre-charged. For Figure 3.19, the pre-charging only took 15 minutes, while for the experiment of Figure 3.20 one

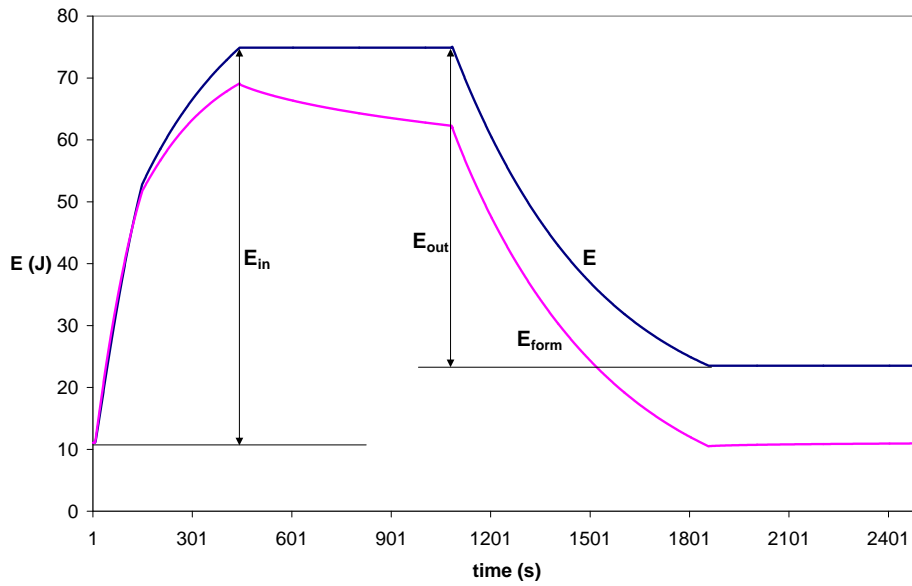


Figure 3.19: Single cycle with quick charging and slow discharging (short pre-charging).

hour of pre-charging was performed. The clear difference in behaviour demonstrates how important the previous history of a supercapacitor can be for its future performance. In order to enable a fair comparison between the different charge and discharge resistor combinations, a standard pre-charge of one hour was performed. In this way, the influence of pre-charging could be excluded.

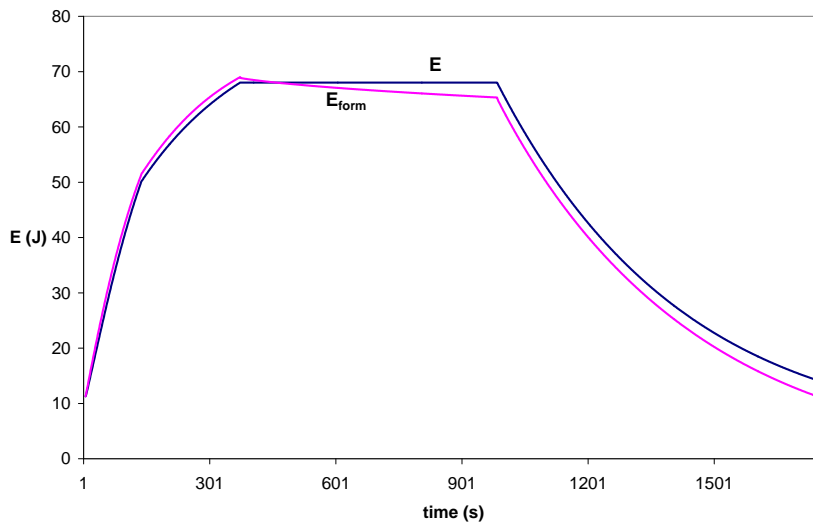


Figure 3.20: Single cycle with quick charging and slow discharging (1 hour pre-charging).

One can also notice a kink in the energy curves during quick charging. This kink is caused by an automatically changed shunt resistor in the digital multimeter. The used DMM (Agilent 34980A Multifunction Switch/Measure Unit with 34921A 40-Channel Armature Multiplexer [25, 26]) uses

a shunt of 0.1Ω for currents higher than 100 mA, while lower currents are led through a higher 5Ω shunt. This is done to achieve high accuracy for small currents. In many circuits, this automatic change has limited influence. Supercapacitors however have very low internal resistances, especially in their fast branches, and because of this low ESR (equivalent series resistance) a changing shunt value can have a quite big influence. The changing shunt phenomenon allows us to conclude that the traditional energy content formula holds best when high currents are applied. After all, after the kink the curves of E and E_{form} go more noticeably their separate ways. At that point, the exponentially decreasing current (test setup forms RC-network) suddenly drops because of the higher shunt resistor.

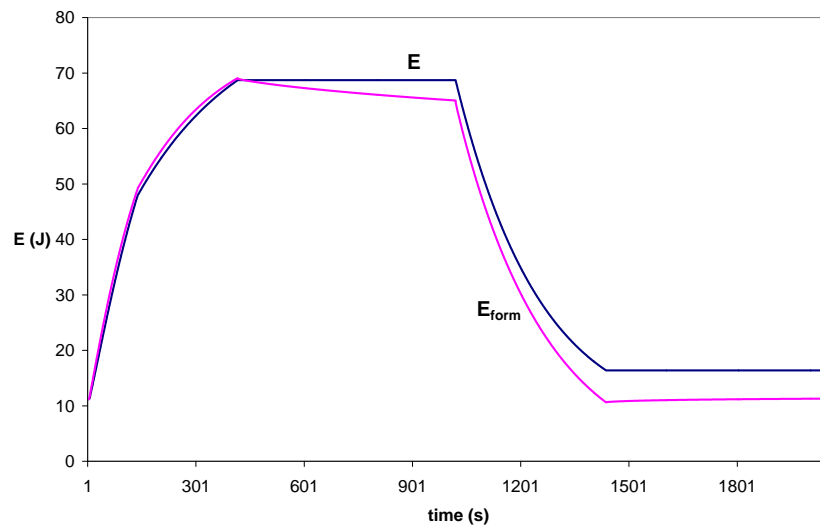


Figure 3.21: Single cycle with quick charging and quick discharging.

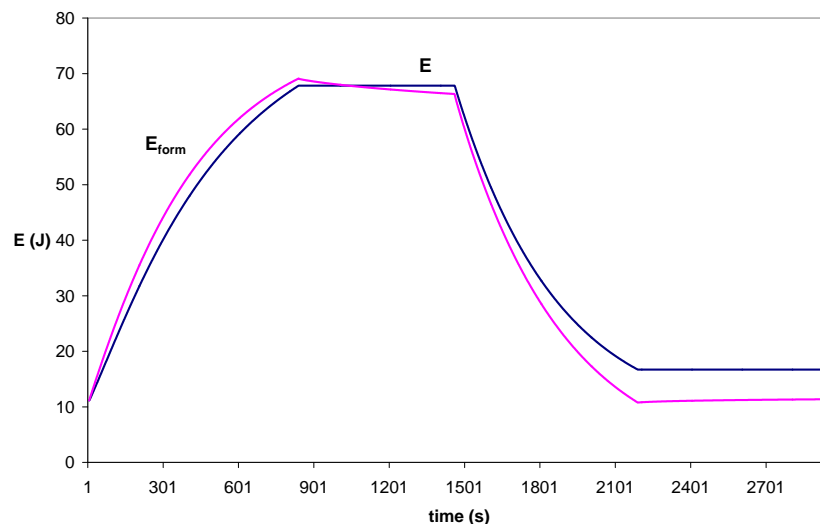


Figure 3.22: Single cycle with slow charging and slow discharging.

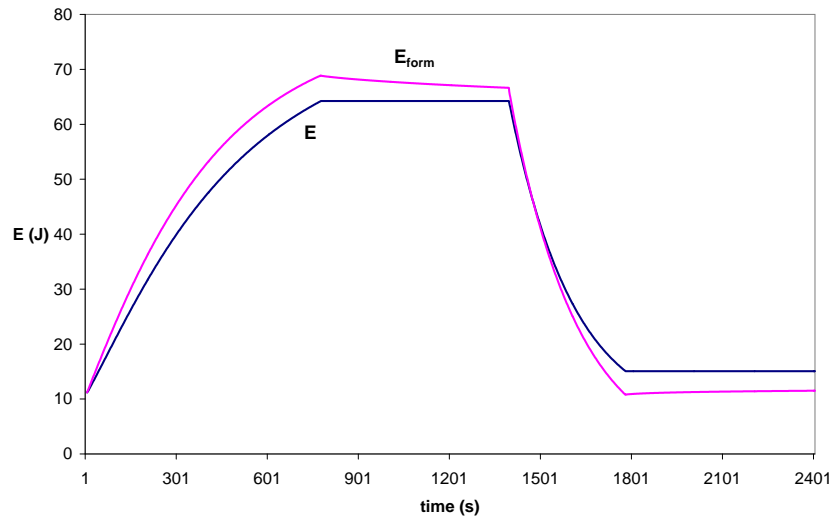


Figure 3.23: Single cycle with slow charging and quick discharging.

A very important characteristic is the cycle efficiency for the different charge/discharge patterns. They are shown in Table 3.5. The result for the quick charging - slow discharging combination with a short pre-charge period is also included in this table because of the insight it gives about the influence of charging history. The cycle efficiency for the short pre-charge situation is substantially lower than the other observed cycle efficiencies. This can be more easily understood when keeping the models of Section 3.2.4 in mind. A shorter pre-charge period means emptier capacitors in the slow branches of the supercapacitor. Consequently, more energy will be needed to fill these branches during charging. This results in a lower cycle efficiency and a longer charging time (about 100 seconds longer for this experiment). The four cycle efficiencies obtained under the same pre-charge conditions are less different from each other. The quick-slow combination achieves the best cycle efficiency, 95.44%. Trying to explain the reason behind the observed efficiency difference is very hard without simulations using equivalent circuit models. Section 3.2.4 already explained however that the extraction of model parameters was out of the scope of this thesis. Another difficulty is the identification of the real losses and the losses caused by the inability of the slow branches to deliver their energy faster. Several graphs show a slow increase of the voltage after the discharging phase. This increase is caused by charge distribution from the slow to the fast branches. The slow branches have at that point a higher voltage over their capacitor than the overall supercapacitor voltage.

quick-slow (short pre-charge)	quick-slow	quick-quick	slow-slow	slow-quick
80.72%	95.44%	90.94%	90.18%	92.65%

Table 3.5: Cycle efficiencies (η_{cycle}).

Cycle efficiencies are based on E_{in} (Table 3.6) and E_{out} (Table 3.7). Their values are however not always very consistent. Completely identical charging conditions seem no guarantee for an identi-

cal E_{in} . Probably this is caused by structural differences between the different used supercapacitor samples.

quick-slow (short pre-charge)	quick-slow	quick-quick	slow-slow	slow-quick
63.83J	56.79J	57.56J	56.70J	53.05J

Table 3.6: The energy E_{in} for the different tested cycles.

quick-slow (short pre-charge)	quick-slow	quick-quick	slow-slow	slow-quick
51.52J	54.20J	52.34J	51.13J	49.15J

Table 3.7: The energy E_{out} for the different tested cycles.

Table 3.8 contains the values of the ratio E_{form}/E at the end of the charging interval. For a short pre-charge period, more energy than defined by the energy content formula needs to be provided since E is larger than E_{form} . A longer pre-charge period seems to entail the opposite. The high value for the slow-quick combination can only be explained by structural differences between the used samples.

quick-slow (short pre-charge)	quick-slow	quick-quick	slow-slow	slow-quick
92.29%	101.39%	100.51%	101.87%	107.21%

Table 3.8: Difference between E and E_{form} after charging (%).

Another important phenomenon is the decrease of the supercapacitor voltage during the delay interval. No energy is extracted from the supercapacitor and still the voltage decreases. This is mainly caused by charge distribution processes - there is also some leakage. Table 3.9 indicates how much energy - according to the energy content formula - is lost during the ten minutes of the delay interval. The supercapacitor that was pre-charged for a short period loses more than 10% of its energy, which can be considered as quite bad for being in a disconnected state. The slow charging combinations exhibit the lowest energy losses or voltage drops. The longer charging time enabled more charge distribution during the charging itself. During the delay interval, less charge needs to be transferred from fast to slow branches leading to a smaller voltage decrease.

quick-slow (short pre-charge)	quick-slow	quick-quick	slow-slow	slow-quick
10.59%	5.74%	6.68%	4.37%	4.17%

Table 3.9: Energy loss during delay according to $E = CV^2/2$ (%).

Table 3.10 compares the validity of the energy content formula during the discharge interval. It contains the values of the ratio $E_{out,form}/E_{out}$, with $E_{out,form}$ being the difference between the energy levels at the beginning and the end of the discharge interval and this according to the energy content

formula. The charging speed appears to be the most decisive factor for the formula validity during discharging. The combinations with slow charging deliver around 10% less energy than the formula would predict. The ratio for the other combinations is close to 100%. For the first time, different pre-charge conditions deliver identical results. The ratio $E_{out,form}/E_{out}$ is apparently only influenced by the very recent past.

quick-slow (short pre-charge)	quick-slow	quick-quick	slow-slow	slow-quick
99.60%	99.96%	102.89%	108.20%	112.39%

Table 3.10: Difference between actual and formula-based E_{out} (%).

Single cycle with long delay interval

The following experiment tests a situation with fast charging, fast discharging and a long delay in between. This situation can manifest itself when an energy harvester is supplied for a short period, only to use the stored energy hours later. The resistors used for charging and discharging are the ones in the left ("quick") column of Table 3.4. The duration of the delay is exact 4 hours. Before the experiment, the supercapacitor was short-circuited for several hours to ensure completely discharged branches. This was done to obtain the strongest possible charge distribution effect.

The outcome of the experiment is shown in Figure 3.24. The energy decrease of approximately 20% - according to the energy formula - is striking. The substantial difference between E_{in} and E_{out} (= difference between end level and start level of E -curve) leads to a cycle efficiency of only 70.51%. It is immediately clear that the behaviour of a supercapacitor cannot be neglected under these test conditions. The ratio $E_{out,form}/E_{out}$ amounts to 118.15%, indicating that the supercapacitor delivers much more energy than the energy content formula would predict. The long delay duration enabled non-negligible charging of the slow branches, leading to the substantial voltage decrease. At this point, the supercapacitor contains much more energy than the energy content formula states. The low cycle efficiency demonstrates how charge distribution not only involves the transfer of charge but also additional loss. After all, when transferred from one branch to another, the charge needs to overcome internal resistance.

Long delay after short single cycle

The next experiment was done to focus on the charge distribution effect after the discharge phase. The same resistors as in the previous experiment were used to generate a short charge/discharge cycle without delay interval. The used supercapacitor was discharged for several hours before the beginning of the measurements. After the discharge phase, the voltage of the disconnected supercapacitor was monitored for almost 18 hours to observe the voltage variations. Figure 3.25 shows the resulting curves (for the first 9 hours) that exhibit very limited variation once the discharging is finished. Figure 3.26 contains the same curves, but only for the lower energy region. Now, a slight voltage increase

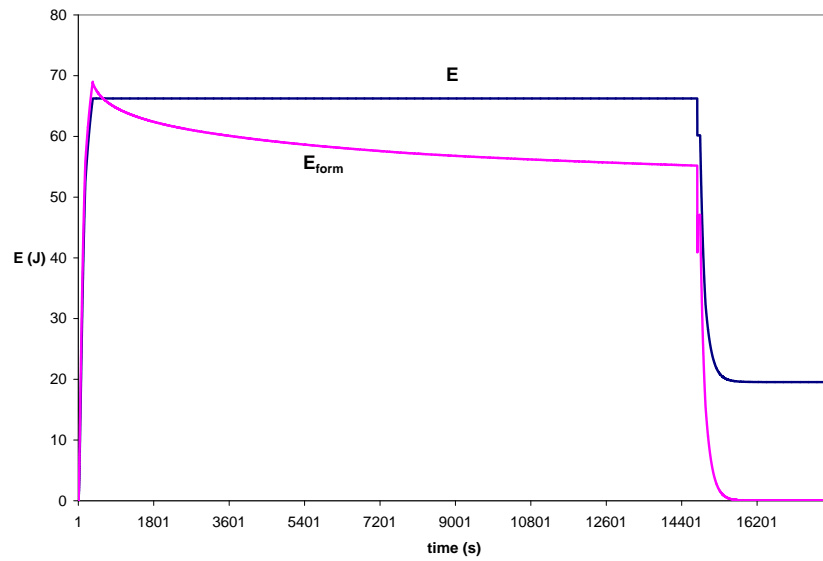


Figure 3.24: Single cycle with long delay interval.

can be perceived as E_{form} rises. The rise is however very limited with an increase of only 250 mJ after 18 hours. The short charge/discharge cycle proved to be too short to cause major charge distribution effects afterwards. The long observation period should be enough to detect leakage. The leakage is however negligible for very low voltages. Consequently, E_{form} experiences no decrease after its rise.

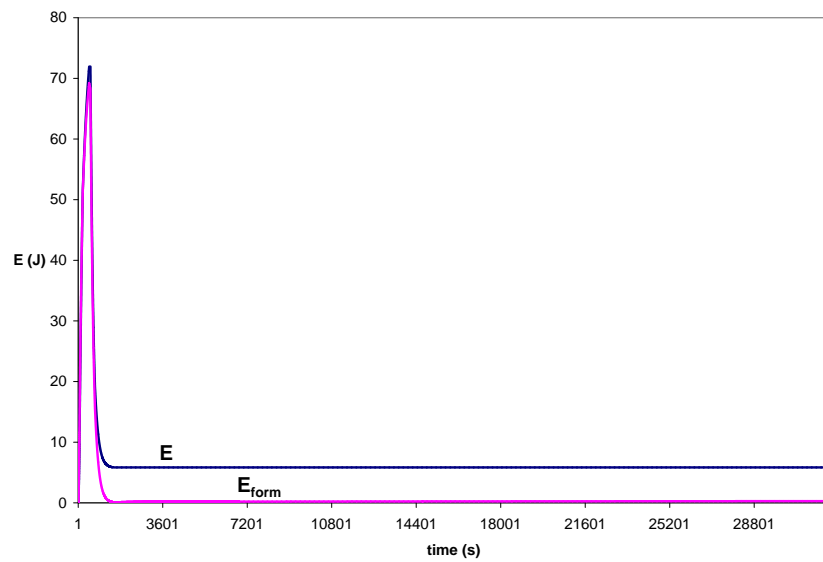


Figure 3.25: Long delay after short single cycle.

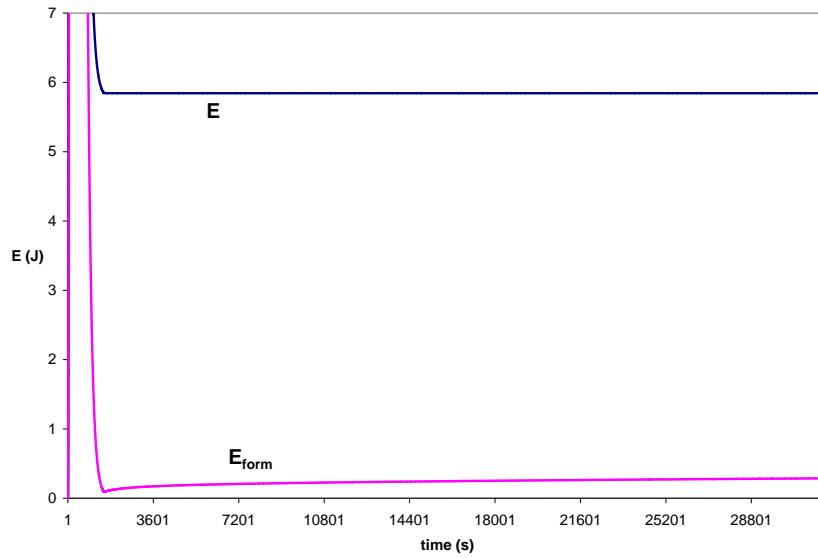


Figure 3.26: Long delay after short single cycle.

Long single cycle

The last single cycle experiment consists of a long charging phase of about 2 hours and an even longer discharging phase. The supercapacitor was once again discharged for several hours before starting the experiment. The charge and discharge resistors were respectively $100\ \Omega$ and $220\ \Omega$. The discharge resistor was chosen this high to prevent fast discharging for high voltages. The current decreases however exponentially with a decreasing voltage, making the discharge for E_{form} smaller than 5 J ($V_{cap} < 675\ \text{mV}$) very slow. Therefore, after 2.5 hours of discharging, the original discharge resistor was replaced with a $4\ \Omega$ resistor to speed up the process.

This type of cycle again behaves differently than seen until now. During charging, an interval during which E_{form} is higher than E , is followed by a period during which E is substantially higher than E_{form} . This leads to a difference of 10% between E and E_{form} at the end of the charging phase. The cycle efficiency amounts to 84.95%, the ratio $E_{out,form}/E_{out}$ to 106.73%.

3.3.4 Multiple cycle experiments

In practice, supercapacitors are not used for just one charge/discharge cycle. In energy harvesters, they can experience totally random charging and discharging patterns and it is obviously impossible to test and measure for every possible pattern. This section will try to investigate how supercapacitors perform when they are subject to a sequence of identical cycles.

Every tested sequence starts with a pre-charged 2 V supercapacitor (at least 1 hour pre-charge). After that, the supercapacitor is charged by a fixed DC voltage source of 2.85 V. The value of the charging resistor is $15\ \Omega$. The moment the supercapacitor voltage reaches 2.5 V, a discharge phase is started

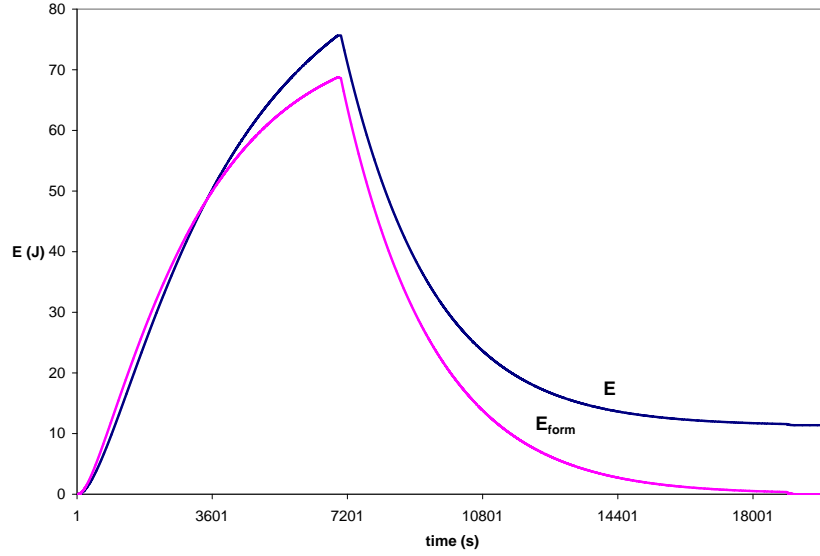


Figure 3.27: Long single cycle.

with a discharge resistor of 22Ω . Three experiments with different lower boundaries for the supercapacitor voltage were executed. Figure 3.28 shows the results for a lower boundary of 250 mV. Other lower boundaries were 1.3 V and 2 V. Once the lower boundary is reached, a charging phase with the already mentioned charge resistor is started. At this point, a periodic charge/discharge cycle sequence begins, with the voltage varying between the experiment-specific lower boundary and 2.5 V. The resistors were chosen in such a way that a single cycle could be representative for a cycle present in energy harvesters. Keeping this requirement in mind, we opted for the minimal possible values, keeping the duration of a whole experiment relatively low. The three different lower boundaries are not completely arbitrary. The intention was to cover a voltage interval of maximum width (250 mV was chosen because discharging to 0 V would have taken too much time), of medium width and of small width. The pre-charge voltage of 2 V was selected because of its presence in the three observed voltage intervals.

Besides the already defined E and E_{form} curves, Figure 3.28 contains a third one, E_{adj} . The energy E_{adj} stands for adjusted energy curve and the definition is very similar to the definition of E . At the beginning of each charge/discharge cycle, E_{adj} is reset to the value of E_{form} . After that, E_{adj} is raised or reduced in the same way as E , following Formula 3.6.

$$\begin{aligned} E_{adj}(n+1) &= E_{adj}(n) + P(n+1) \cdot 1 s \\ &= E_{adj}(n) + I_{cap}(n+1) \cdot V_{cap}(n+1) \cdot 1 s \end{aligned} \quad (3.6)$$

This definition allows to easily observe the difference between E_{in} and E_{out} for each cycle, whatever its position in the cycle sequence is. The energy E_{in} represents the energy inserted in the supercapacitor during charging from the experiment-specific lower boundary to 2.5 V. The energy E_{out} represents the

energy delivered by the supercapacitor during discharging from 2.5 V to the experiment-specific lower boundary. The difference between E_{in} and E_{out} for a specific cycle is basically the difference between the start and the end value of E_{adj} .

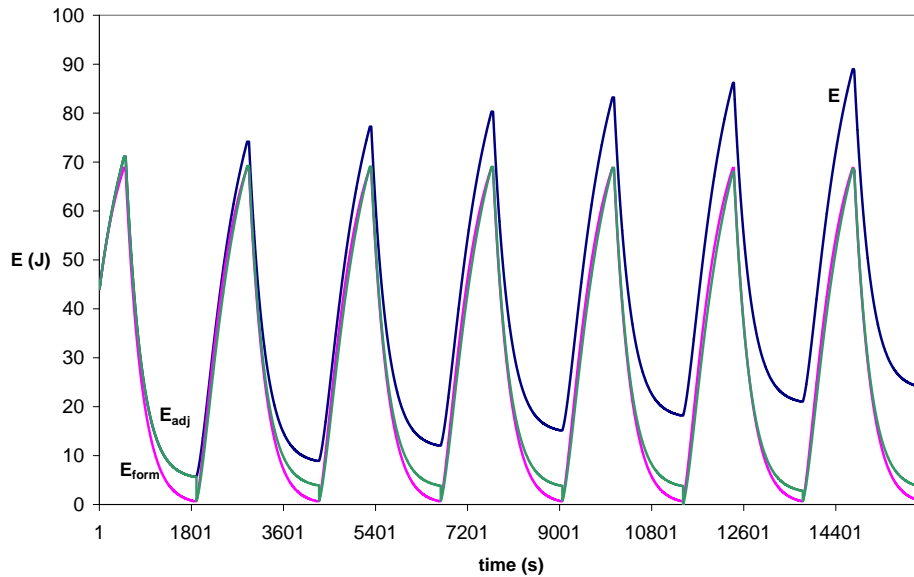


Figure 3.28: Multiple charge/discharge cycles between 0.25 V and 2.5 V.

Excluding the first cycle, all cycles in Figure 3.28 seem very much alike. Apparently, when identical cycles are applied, the energy behaviour of the supercapacitor is the same for each cycle, at least after a certain transition period. The evolution of the cycle efficiency throughout the sequence (6 cycles) was examined for the three different lower boundaries and the results can be found in Figure 3.29. The 2 V to 2.5 V cycle efficiencies have lower values for the first two cycles but stabilize after an increase. Besides some small variations, the other two cycle efficiency sequences seem already quite stable.

In general, we can conclude that the performance of a supercapacitor is only influenced by its most recent charging history. It takes no more than 3 cycles to arrive to a quite stable cycle efficiency. At that point, the influence of the pre-charging is almost completely cancelled. That is probably also the reason why the 2 V to 2.5 V cycle sequence at first sight needs more cycles to stabilize. Because its pre-charge voltage and lower boundary were equal, the first cycle starts immediately at the beginning of the experiment. For the other experiments, the first cycle only starts after a charging phase to 2.5 V and a discharging phase to its lower boundary. This discharge phase is similar to the discharge phase of a normal cycle, bringing the supercapacitor closer to its eventual state before the actual first cycle starts.

Figures 3.30, 3.31 and 3.32 show a single cycle chosen randomly from the cycle sequences. E is omitted in favour of E_{adj} to allow an easier comparison of the measured energies and the theoretical energy variations according to the energy content formula. They will not be discussed in the same

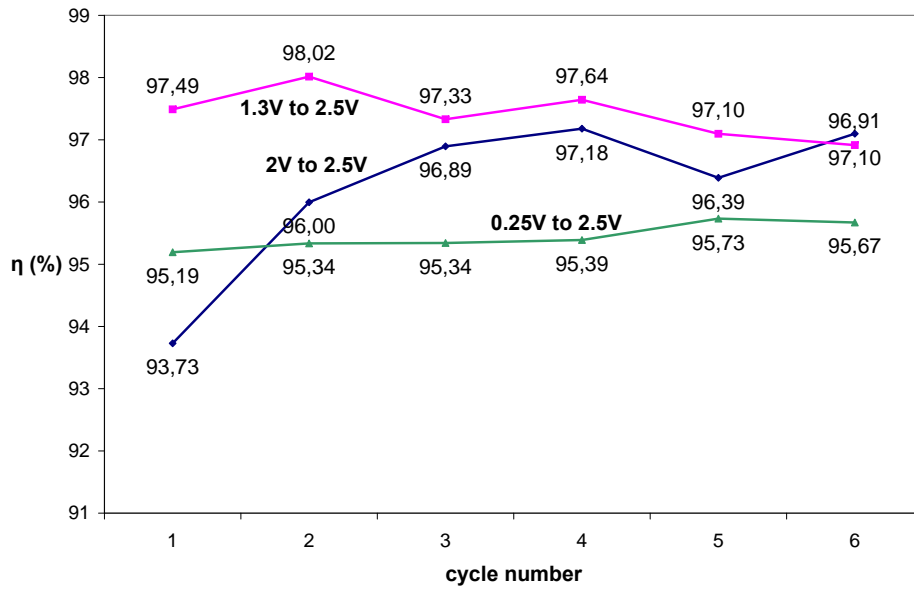


Figure 3.29: Multiple charge/discharge cycles: cycle efficiencies (η_{cycle}).

extensive way as some of the single cycle experiments. The only intention of this section is the investigation of specific multiple cycle behaviour. In between the charging and discharging phase, a short delay interval can be noticed. This is the time during which the charge test setup is manually changed into the discharge test setup.

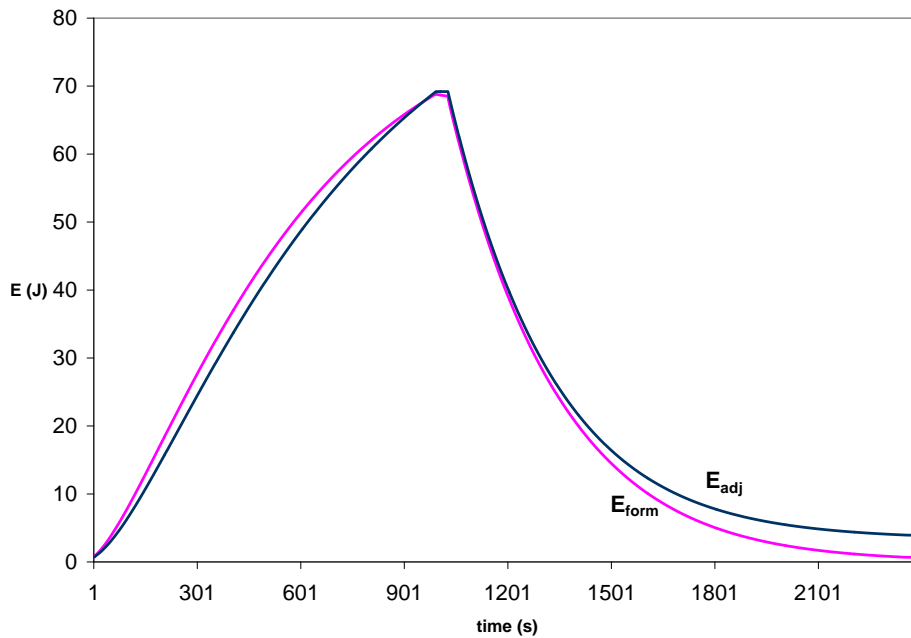


Figure 3.30: Multiple charge/discharge cycles between 0.25 V and 2.5 V: one cycle.

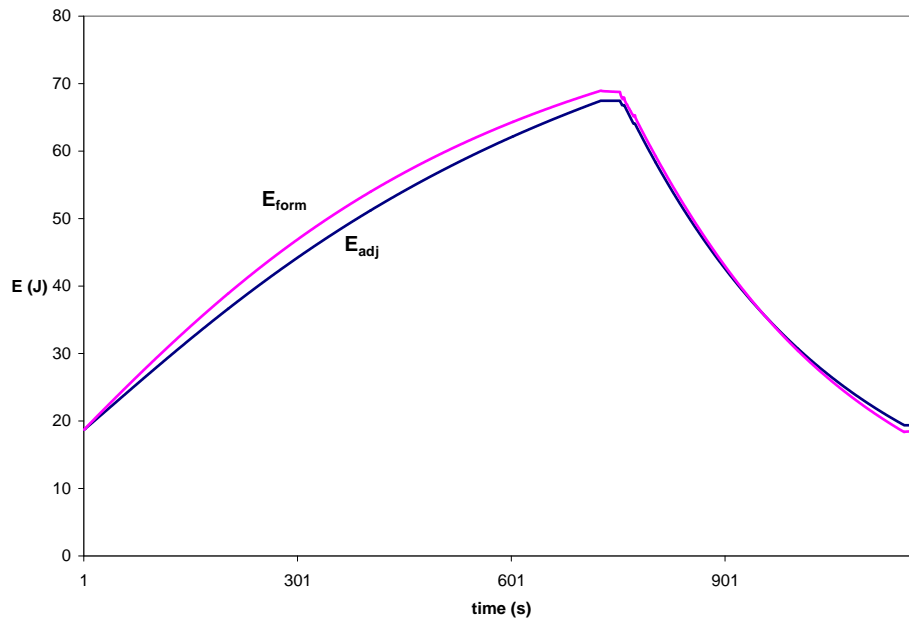


Figure 3.31: Multiple charge/discharge cycles between 1.3 V and 2.5 V: one cycle.

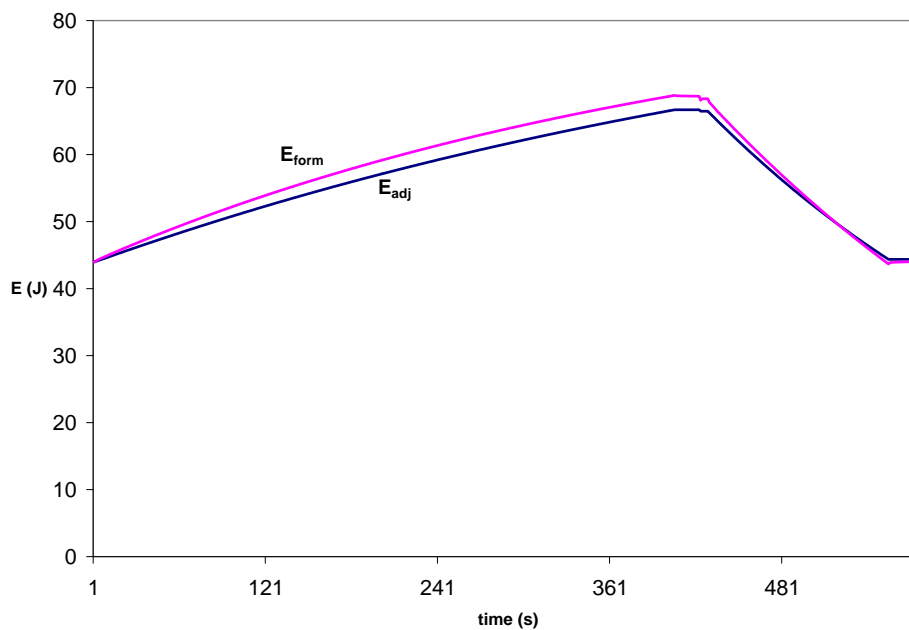


Figure 3.32: Multiple charge/discharge cycles between 2 V and 2.5 V: one cycle.

The importance of the pre-charge voltage is also demonstrated by a repetition of the 1.3 V to 2.5 V experiment, now however with the supercapacitor pre-charged to 0.5 V instead of 2 V. Figure 3.33 compares the achieved cycle efficiencies. The pre-charge voltage of 0.5 V is much lower than the average voltage during the cycle sequence (somewhere between 1.3 V and 2.5 V). It takes consequently longer to bring the slower branches of the supercapacitor around these average voltage levels. The

additional charging of the slow branches causes a lower cycle efficiency for the first two cycles.

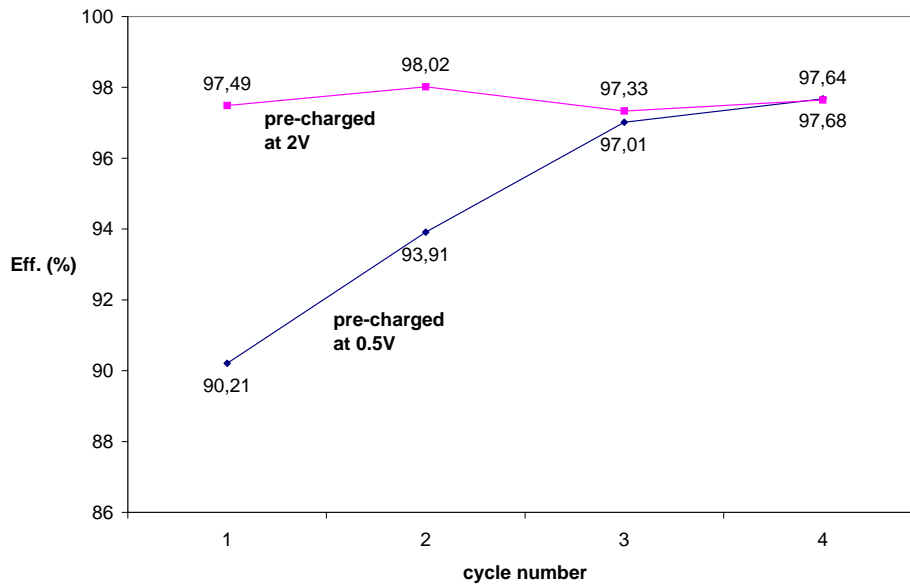


Figure 3.33: Multiple charge/discharge cycles between 1.3 V and 2.5 V: influence of pre-charging on η_{cycle} .

For a certain charge/discharge cycle, multiple cycle efficiencies can be calculated. Until now, the mentioned cycle efficiencies were based on E_{in} and E_{out} with the lower boundary of the experiment as voltage reference. It is however also possible to take another voltage reference and calculate E_{in} as the inserted energy during the charging from this reference voltage to 2.5 V. In an analogous way, E_{out} is then the delivered energy during discharging from 2.5 V to the new voltage reference. Figure 3.34 shows this in a graphical way. The charge/discharge interval is 250 mV to 2.5 V. At the same time, the new cycle efficiency is based on the energies measured between 1.3 V up to 2.5 V and back. E_{ref} is the energy at the reference voltage according to the energy content formula. The used capacitance value was 22 F for all experiments.

The average cycle efficiencies for the three different charge/discharge cycles and for three different voltage references are summarized in Table 3.11. The energy efficiencies in a certain voltage interval clearly depend on the overall charge/discharge interval. Compared to a 2 V to 2.5 V cycle, going from 2 V to 2.5 V and back is 10% less efficient than when this is done during a 250 mV to 2.5 V charge/discharge cycle. The key in understanding these numbers is keeping the voltages of the capacitors in the slow branches in mind (see models in Section 3.2.4). During the charging from 2 V to 2.5 V, the slow branches are less charged for a 250 mV to 2.5 V cycle than for a 2 V to 2.5 V cycle as the overall voltage for the last mentioned cycle type never goes below 2 V. Consequently, more energy is drawn to the slow branches. This effect on the cycle efficiency is mitigated when lower voltage references are used, leading to higher cycle efficiencies for the same charge/discharge interval.

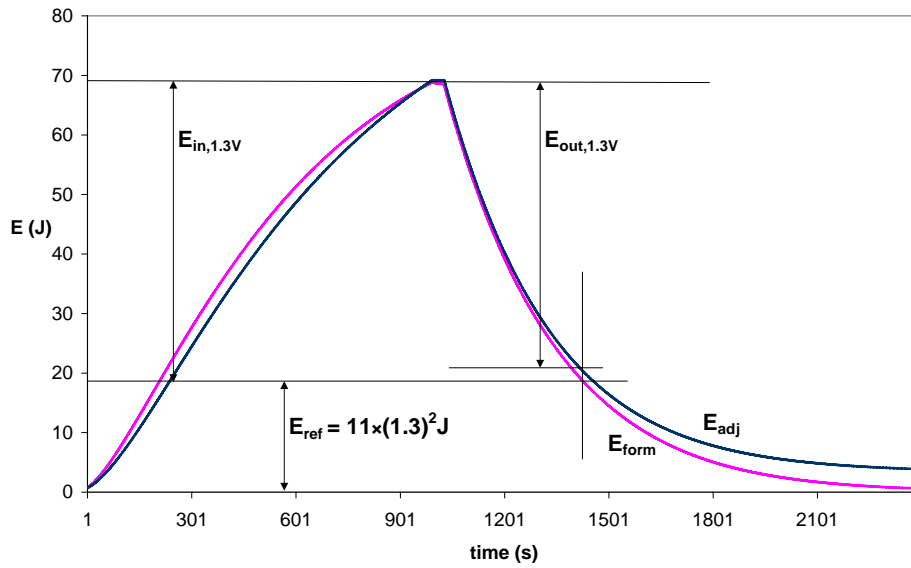


Figure 3.34: Multiple charge/discharge cycles between 0.25 V and 2.5 V: cycle efficiency with 1.3 V as reference.

		Charge/discharge interval		
		0.25 V to 2.5 V	1.3 V to 2.5 V	2 V to 2.5 V
η_{cycle} reference	0.25 V	95.44%		
	1.3 V	92.03%	97.41%	
	2 V	86.12%	91.47%	96.71%

Table 3.11: Average cycle efficiencies (η_{cycle}) for multiple cycles .

Table 3.12 gives an overview of the observed average charging times. The charging time is the time needed to charge from the η_{cycle} reference to 2.5 V. Charging from a certain voltage reference takes longer when the lower boundary of the charge/discharge cycle is placed lower. This fits perfectly into the picture of less charged slow branches for lower cycle boundaries.

		Charge/discharge interval		
		0.25 V to 2.5 V	1.3 V to 2.5 V	2 V to 2.5 V
η_{cycle} reference	0.25 V	983.83 s		
	1.3 V	777.67 s	722.00 s	
	2 V	492.00 s	459.78 s	404.73 s

Table 3.12: Average charging times for multiple cycles.

Table 3.13 shows the same evolution for the discharging times. Again, this can be explained by assuming less charged slow branches. When the slow branches are less charged, more charge is transferred from the fast to the slow branches during discharging. This process only stops when the

decreasing voltage over the capacitors of the fast branches reaches the voltage over the capacitors of the slow branches. Only at that point, all charge leaving the branches is transferred out of the supercapacitor. This phenomenon is depicted in Figure 3.35. The Figure shows the discharge test setup with the supercapacitor replaced by the simplified model of Section 3.2.4. As it is only the intention to visualize the explained concept, the voltage values are arbitrary - but still realistic for being at the beginning of the discharge phase. The thick black arrows indicate the direction of the different currents.

		Charge/discharge interval		
		0.25 V to 2.5 V	1.3 V to 2.5 V	2 V to 2.5 V
η_{cycle} reference	0.25 V	1297.67 s		
	1.3 V	397.83 s	388.38 s	
	2 V	144.86 s	134.44 s	126.09 s

Table 3.13: Average discharging times for multiple cycles.

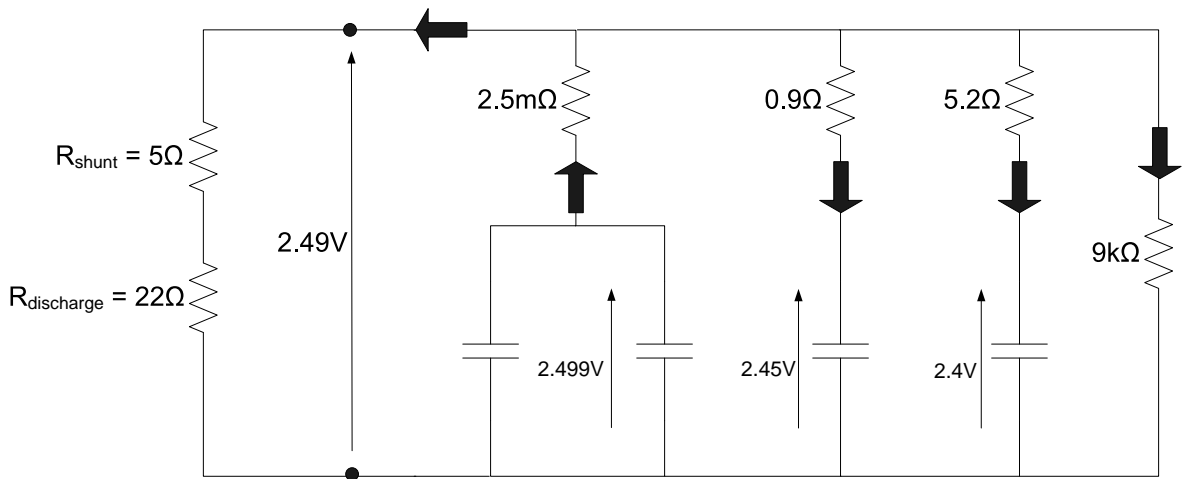


Figure 3.35: Charge distribution in equivalent circuit model at beginning of discharge phase.

Chapter summary and conclusions

This chapter contains a general theoretical and practical discussion of supercapacitors. More important however were the findings about their behaviour, based on the own measurement results.

Different charge/discharge patterns can have very varying energy efficiency performances. Also the validity of the energy content formula can change quite strongly depending on how the supercapacitor was used in the past and will be used in the future. The voltage at a certain moment in time gives only limited information about how much energy can be extracted from a supercapacitor for a certain discharge pattern. The measurements were still rather general and were less focussed on energy harvester applications. They showed however how strong a supercapacitor's behaviour can differ from its behaviour defined by the energy content formula. Some cycles - like the short cycle with long delay interval - led to cycle efficiencies of only 70%. For those cycles, the specific behaviour of supercapacitors cannot be ignored.

When designing energy harvesters, the performance and behaviour of supercapacitors should be taken into account. The most accurate way to do this, would be the execution of a series of tests that would cover the majority of the possible charge/discharge patterns for the supercapacitor. Depending on the intended usage profile of the sensor node and the available power profile of the energy source, this can become a very complex and tedious task. Another and probably easier way of investigating the energy behaviour of supercapacitors is the use of simulations based on equivalent circuit models. Once the parameters of the model are extracted, simulations of any imaginable charge/discharge pattern can be performed. One should however check if the simplified model that is used in power electronics, is completely valid for charge/discharge patterns that occur in energy harvesters.

Chapter 5 will analyze, among other characteristics, the supercapacitor's performance when used in the Bologna harvester.

Chapter 4

Bologna energy scavenger for sensor nodes

4.1 Introduction

This chapter will take a closer look at the Bologna scavenger. The working principle of the scavenger will be explained based on its circuit and circuit elements. Afterwards, own observations and measurements will be discussed in section 4.3. Until now, the Bologna circuit has been tested mainly for ideal situations where plenty of light is available. In this chapter more attention will be given to the performance of the scavenger in limited light conditions. Also some other problems that can occur because of the scavenger's shortcomings will be examined.

4.2 Circuit design

4.2.1 MPP tracker

The heart of the Bologna scavenger is the MPP tracker. This part of the circuit tries to make sure that the solar cell delivers the maximum achievable power, irrespective of the light conditions. The MPP tracker is based on a buck converter architecture (see Figure 4.1). A buck converter is a switching DC/DC converter that can be used to supply any output voltage between 0 V and the input voltage. Therefore, a buck converter can also be called step-down converter. In a normal buck converter, the duty ratio of the control signal for the switch determines the output voltage. Through a feedback loop a constant output voltage is ensured, adjusting the duty ratio when the input voltage or the drawn output power changes.

Figure 4.2 shows the complete MPP tracker circuit. In contrast to the buck converter, the purpose of the circuit is keeping the input voltage (V_{solar}) - instead of the output voltage - around an imposed value, preferably the maximum power point. Through a voltage divider (with large resistors to restrict losses) the solar cell voltage is led to one of the inputs of a comparator (LTC1440 [27]). The other

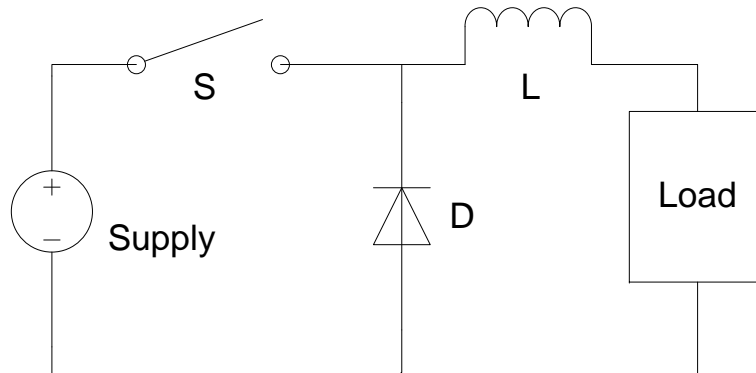


Figure 4.1: Buck converter architecture.

input of the comparator is the voltage-divided open-circuit voltage of a pilot cell, a very small solar cell that is exposed to the same light conditions as the main solar cell. The relationship between the open-circuit voltage of the main solar cell (Solarex MSX-005F [28]) and of the pilot cell (Clare CPC1824 [29]) is approximately linear (this assumption will be checked in Section 4.3.2). We already mentioned in Chapter 2 the linear relationship between the V_{oc} and the V_{mpp} of a solar cell. Consequently, there is also a linear relationship between the open-circuit voltage of the pilot cell and the maximum power point of the main solar cell (equation 4.1).

$$\begin{aligned} V_{mpp} &\approx V_{oc} \cdot k_{mpp} \\ &\approx V_{oc,pilot} \cdot k_{pilot} \cdot k_{mpp} \end{aligned} \quad (4.1)$$

By choosing the proper resistors for the voltage dividers that are connected to the main solar cell and the pilot cell (last divider is not depicted in the circuit as dividing is done before the "Pilot Cell" port), the comparator is configured to switch its output when the solar cell voltage equals the maximum power point. The resistors R_3 and R_4 configure the hysteresis of the comparator. By adding hysteresis, one threshold voltage is replaced by a lower and an upper threshold. The hysteresis prevents unwanted switching that would occur because of the noise of the solar cell and pilot cell. The maximum allowed difference between upper and lower threshold is 100 mV for the LTC1440. The resistance values given in the picture set the hysteresis voltage band to approximately 15 mV.

The power supply of the comparator has to be connected to pin V+, supplying a voltage of more than 2 V. How the power is supplied, will be discussed in Section 4.12. The circuit also contains a Zener diode. This diode has a breakdown voltage close to the maximum allowed voltage of the supercapacitor and protects the supercapacitor from being overcharged.

How the scavenger exactly works, will be explained with the help of Figures 4.3 and 4.4. Both of them depict a simplified MPP tracking circuit with the comparator and its connections omitted. In the first figure, the situation when the PMOS switch is open, is displayed. The thick black arrows indicate the direction of the different currents.

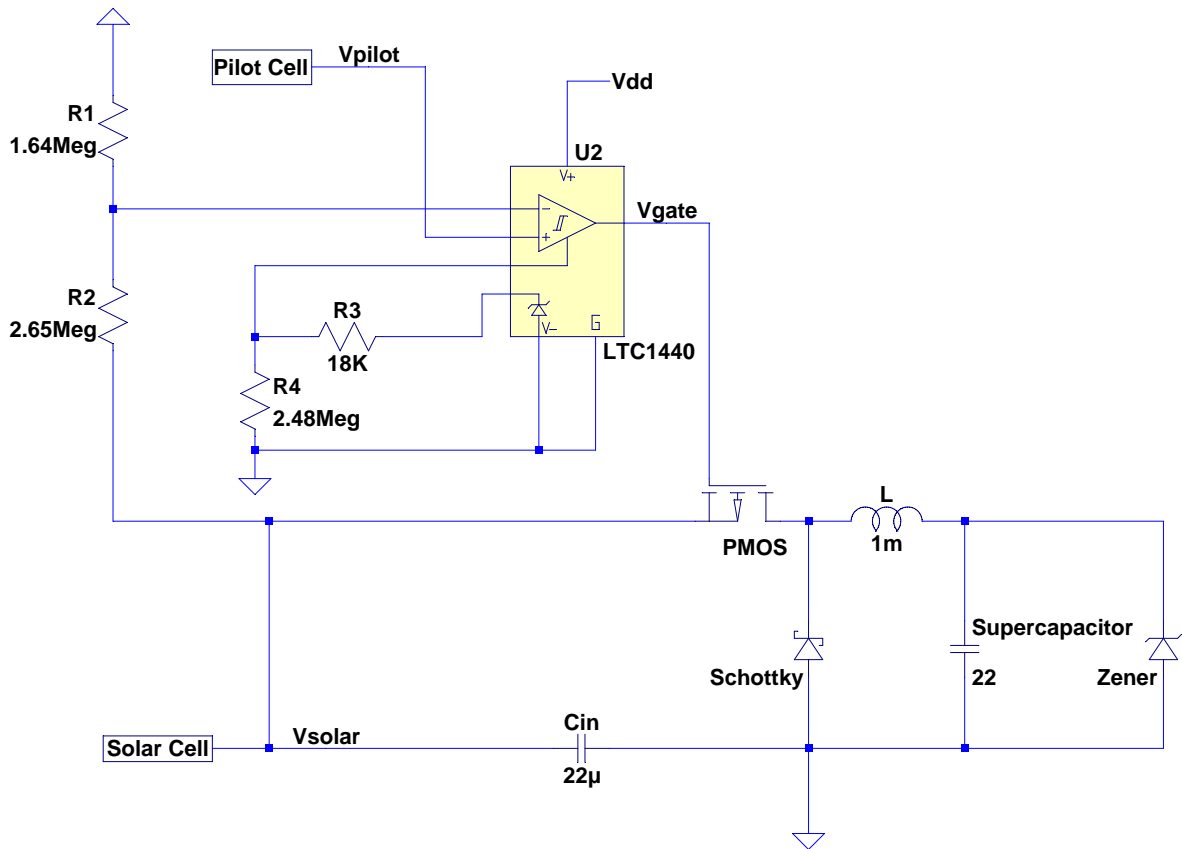


Figure 4.2: Complete MPP tracker circuit.

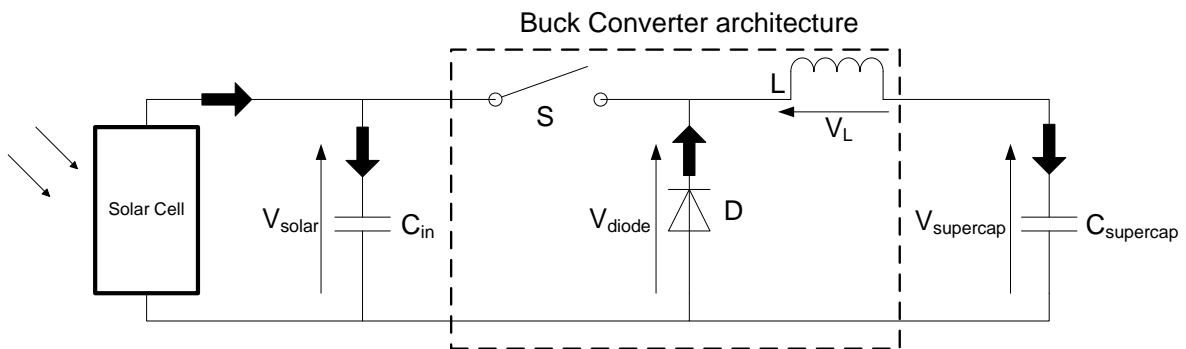


Figure 4.3: MPP tracker circuit with open switch.

When the switch is open, the solar cell charges the small capacitor C_{in} . The voltage V_{solar} increases until the difference between the two comparator inputs reaches the lower threshold of the comparator (voltage divider of V_{solar} is connected to inverting comparator input, see Figure 4.2). At that point the comparator switches to a low output, closing the PMOS transistor.

What happens at the other side of the openend switch will be discussed later on. First, we go to Figure

4.4 to see what happens when the switch closes. The moment the switch closes, the voltage over the inductor L (V_L) equals $(V_{solar} - V_{supercap})$. This causes a current increase in the inductor in the direction of the supercapacitor. This increase takes place at a rate given by Formula 4.2.

$$\frac{dI}{dt} = \frac{(V_{solar} - V_{supercap})}{L} \quad (4.2)$$

During normal operation, the average current going through the inductor is higher than the current provided by the solar cell (soon more about this). Therefore, the input capacitor C_{in} is discharged to provide the additional current needed by the inductor. Because of this discharge, the voltage V_{solar} decreases. The moment that the difference of the two comparator inputs reaches the upper comparator threshold, the PMOS transistor is opened again. This starts a new charging phase for C_{in} . Because of the sequential charging and discharging of C_{in} , V_{solar} remains close to the maximum power point. The smaller the hysteresis of the comparator, the smaller the voltage band to which the solar cell voltage is confined.

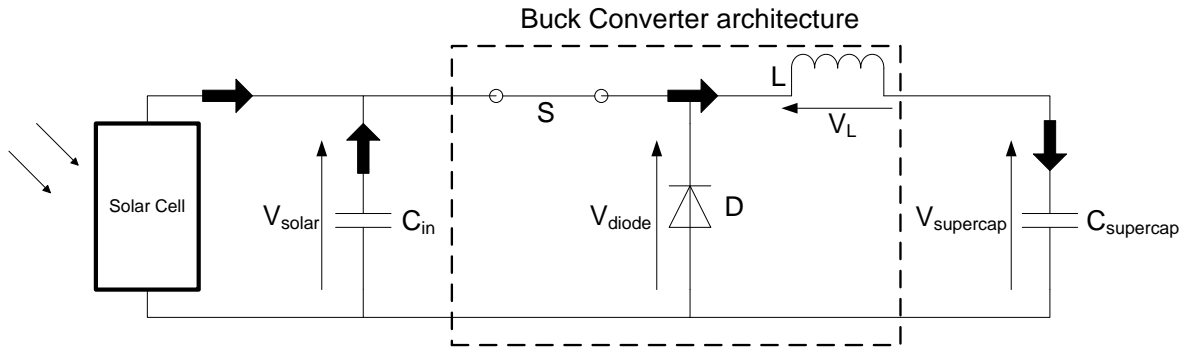


Figure 4.4: MPP tracker circuit with closed switch.

We now return to Figure 4.3. No inductor current can be provided through the opened switch. Because of the subsequent swift decrease in inductor current, the voltage over the inductor instantly turns negative, following Formula 4.3.

$$V = L \frac{dI}{dt} \quad (4.3)$$

The current decrease is almost infinitely fast, which should lead to a very negative voltage over the inductor, more than probably causing a breakdown of the PMOS transistor. Then however, the Schottky diode starts to play its role. The moment the quickly decreasing V_{diode} reaches $-V_D$ (V_D = diode threshold), the diode starts to conduct, taking over the inductor current from the switch. Once this very fast process is finished, V_L equals $-(V_D + V_{supercap})$. This negative inductor voltage causes a decrease of the current in the direction of the supercapacitor. This decrease has a rate described by Formula 4.4.

$$\frac{dI}{dt} = -\frac{(V_D + V_{supercap})}{L} \quad (4.4)$$

The decrease ends when the input capacitor C_{in} reaches its maximum level, leading to the switch being closed again. The diode stops conducting and the switch takes over. This starts a repetition of the process already explained through the help of Figure 4.4. The used diode is a Schottky diode to reduce the energy losses. A Schottky diode has a lower threshold (250 mV compared to 600 mV), leading to a lower voltage drop over the diode when it conducts. This means that less power is lost in a Schottky diode than in a normal one.

A key assumption in this explanation has been that the inductor current is larger than the solar cell current when the switch is closed. This assumption is necessary to achieve a decrease of V_{solar} . This premise is however not always satisfied as will be proved in Section 4.3.5. A preview of what can happen is given by Figure 4.5, a simulation result obtained by LTspice/SwitcherCAD III (freeware simulation tool released by Linear Technologies). This specific simulation depicts the start-up of the MPP tracker. The curve I_L represents the current going through the inductor in the direction of the supercapacitor while I_{solar} represents the current leaving the solar cell. The small negative dent of I_L at the beginning of the simulation is caused by the fact that the comparator still needed to start up. For a moment, the switch was closed which caused current to flow from the pre-charged supercapacitor to the input capacitor C_{in} .

The simulation begins when the solar cell gets connected to the MPP tracker of which the input capacitor is empty. The input capacitor is charged by the solar cell and V_{solar} increases while I_{solar} decreases following the VI curve of the solar cell. The switch closes the moment V_{solar} reaches the voltage that causes the comparator to switch. At that point, I_L starts to increase. V_{solar} however still rises because I_L is smaller than the current delivered by the solar cell, I_{solar} . Starting from the moment I_L rises above I_{solar} , V_{solar} starts its decline. After some switching, I_L reaches a steady state. In this steady state, the current increase when the switch is closed equals the current decrease when the switch is opened.

In this simulation the inductor current in its steady state is always higher than I_{solar} . During the operation, the supercapacitor is charged. The increasing $V_{supercap}$ leads however to a lower average inductor current. After all, keeping Formulas 4.2 and 4.4 in mind, an increasing $V_{supercap}$ causes a lower current increase rate and a higher current decrease rate. The time during which the current decreases, remains the same since the charging of C_{in} is independent of $V_{supercap}$. The time during which the current increases, rises because of the lower average inductor current - it takes longer to discharge C_{in} . Experiments and simulations show however that this last effect is not strong enough to overcome the rate changes. Calculations that try to predict this behaviour are not at all straightforward because of the constantly changing V_{solar} and I_{solar} , leading to constantly changing rates and charging/discharging times. Therefore, one has to turn to simulations or actual tests. The moment the inductor current drops below the solar cell current, unwanted behaviour can be observed (see Section 4.3.5).

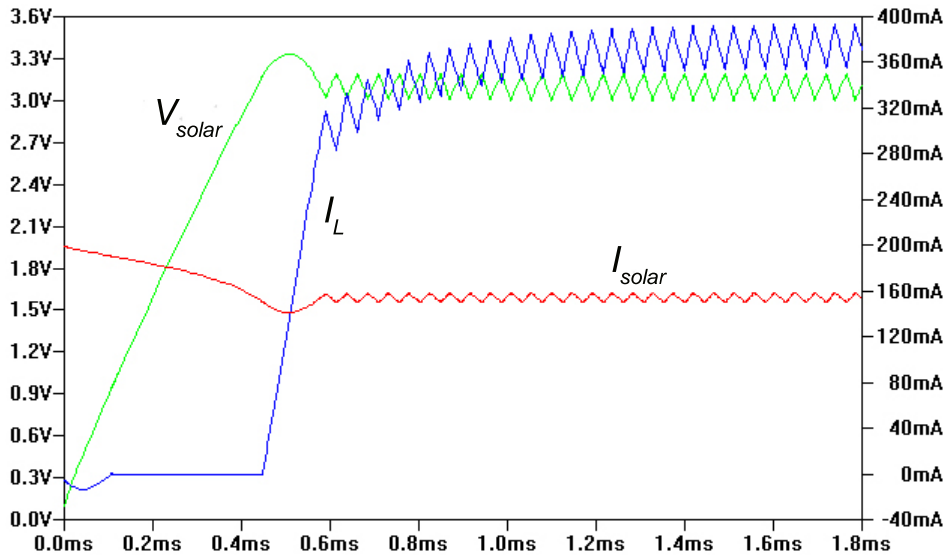


Figure 4.5: MPP tracker simulation.

4.2.2 DC-DC converter

This section discusses another essential part of an energy scavenger, the DC/DC converter. Sensor nodes contain several advanced IC's that require a stable supply voltage. Some sensor nodes, like the BTnode, have a DC/DC converter onboard and do not require the energy scavenger to have a DC/DC converter of its own. The Bologna scavenger however has a DC/DC converter to ensure compatibility with those other sensor nodes requiring a stable input voltage (e.g. the Tmote [30]).

Figure 4.6 depicts the part of the energy scavenger circuit that is built around the DC/DC converter. The used DC/DC converter IC is the LTC3401 from Linear Technologies [31]. This is a high-efficiency step-up converter that allows to provide a stable output voltage (e.g. 3.3 V for many sensor nodes) out of a lower, less stable input voltage. The input is at the same time used to power the device during start-up and the typical start-up voltage is 0.85 V. Once the device reaches the desired output voltage, the output takes over the supply function of the input, allowing even lower input voltages (down to 0.5 V). The actual minimal allowed input voltage depends on the load and more specifically on the output current. The higher the output current, the higher the required input voltage.

Most of the external components connected to the LTC3401 are an essential part of the DC/DC converter - except the supercapacitor of course - and they allow to easily configure the converter by changing one or more of their values. The associated datasheet gives advice and information about how these component values need to be chosen. A DC/DC converter is a fairly standard component in many contemporary circuits and for more details the reader is referred to the mentioned datasheet.

We will however include a short explanation of the working principle of a step-up converter, also called boost converter, and focus on some specific issues that can be important when trying to achieve

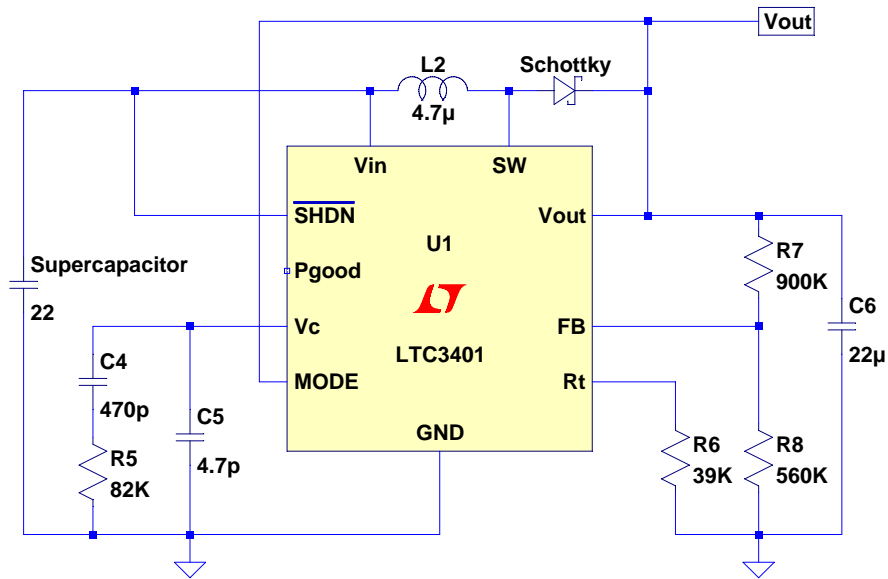


Figure 4.6: DC/DC converter (LTC3401) circuit.

high efficiency. Figure 4.7 depicts the fundamental architecture of a boost converter. The LTC3401 contains several feedback loops with advanced control circuitry and among other components, also an oscillator. The working principle can however still be reduced to what is shown in Figure 4.7.

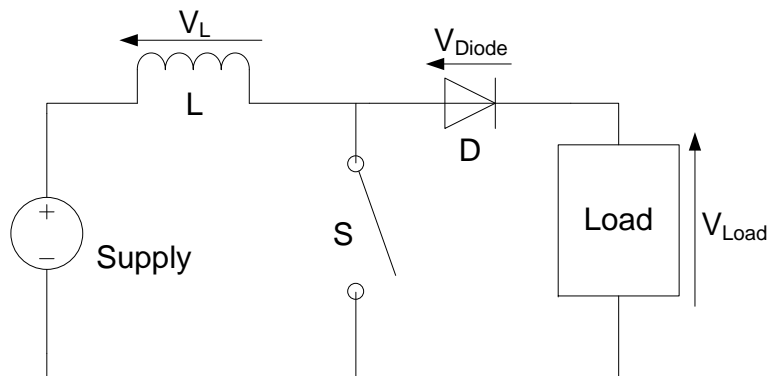


Figure 4.7: Boost converter architecture.

The working principle is very similar to the buck converter, although the circuit is used for opposite purposes. When the switch S is closed, the increasing inductor current ($V_L \approx V_{supply}$) runs to ground. The moment the switch opens, the fast decrease in inductor current leads to a very fast increase of V_L . Once V_{diode} reaches V_D , the diode threshold, the diode clamps the voltage over the inductor to $-(V_D + V_{load} - V_{supply})$. This negative V_L - when V_{supply} is smaller than V_{Load} - causes a decrease of the inductor current. The current decreases but is still positive. In this way, charge is transferred from a lower voltage to a higher one. When the switch closes, the diode stops conducting and the described

process starts all-over again. Control circuitry with feedback loops ensures a stable output voltage. Most DC/DC converters have a small output capacitor (like C6 in Figure 4.6) to stabilize the output voltage. The converter tries to keep the voltage over this capacitor constant, no matter how much current is drawn by the load.

The LTC3401 is a fixed frequency converter of which the frequency is configured by the resistor connected to the R_t pin (Figure 4.6). The frequency can be as high as 3 MHz. A higher frequency allows the use of smaller components but also causes more switching losses and consequently a lower efficiency. The converter switches at a fixed frequency and adjusts the duty ratio depending on how much current the load needs. For light loads, it is however recommendable to use the LTC3401 in another mode, the burst mode. In this mode, the peak inductor current is always 1/3 of the current limit value and returns to zero current on each cycle. During burst mode operation the operation is variable frequency, providing a significant efficiency improvement at light loads. After all, when no extra charge is needed for the output capacitor, the converter goes in a sleep mode, only consuming a very low quiescent current of $38 \mu\text{A}$. Sensor nodes often have very low duty cycles. Some are active for only a few minutes to stay inactive or less active for more than an hour afterwards. During this inactive period, burst mode can bring a substantial improvement of the efficiency as the converter would be in sleep mode most of the time. In fixed-frequency mode the converter would have a very low duty ratio but would still continuously switch at the configured frequency. A high voltage at the MODE pin enables burst mode. It is recommended to enable burst mode only once the converter has started up and therefore the MODE pin is connected to the converter output, as can be seen in Figure 4.6.

Figure 4.8 shows a simulation of the DC/DC converter in fixed frequency (300 kHz) mode for an input voltage of 1.8 V and a load that draws approximately 35 mA. The output voltage is kept stable at the desired 3.3 V. The switching frequency is constant and the switch is closed for only 22% of the time (I_L increases when switch is closed). Figure 4.9 shows a simulation for the same input voltage and load but with the converter in burst mode. In this mode, the hysteresis of the output voltage around the desired value is larger but for most applications still more than acceptable. A sequence of bursts with a constant peak current is followed by a period of very low inductor current (sleep mode). This can be seen even better in a more detailed plot of the same simulation (Figure 4.10).

The discussed simulations were intended to explain the conceptual difference between the two converter modes. For the used load (35mA) the fixed-frequency mode is in fact more efficient than the burst mode. The higher currents in the burst mode are causing losses that cannot be offset by the periods during which the converter is in sleep mode. Figure 4.11 presents the converter efficiency as a function of the output current. Only for light loads, the burst mode offers substantial improvement. It should be clear that the recommendable mode differs for different sensor nodes and for the different duty cycles in which they are used. By choosing for the burst mode, the Bologna scavenger shows a preference for low duty cycle sensor nodes.

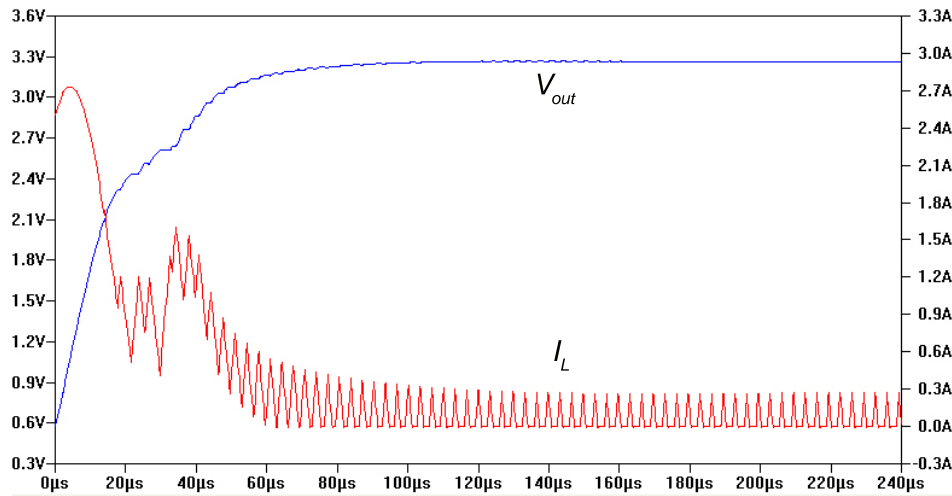


Figure 4.8: DC/DC converter in fixed frequency (300 kHz) mode.

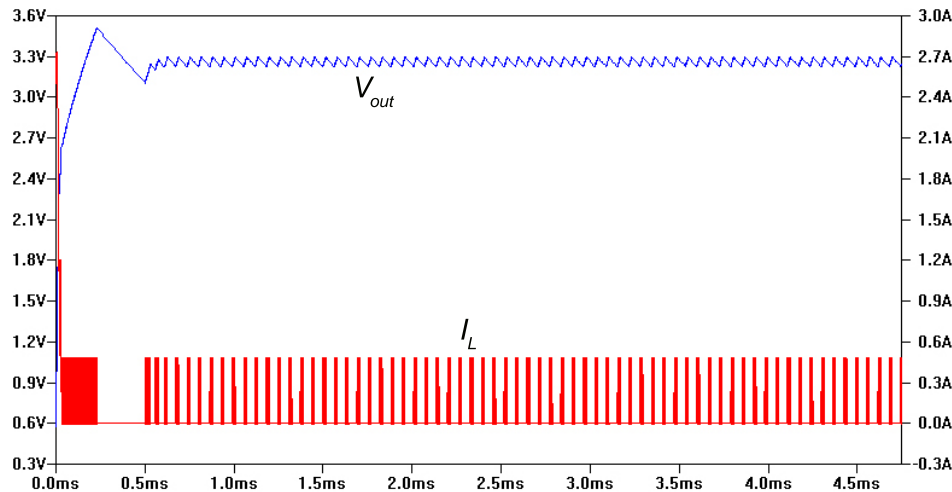


Figure 4.9: DC/DC converter in burst mode.

4.2.3 Supercapacitor

In the previous chapter we already referred to this section for an explanation of the used supercapacitor values. The 22 F supercapacitor was selected out of 22 F, 33 F and 50 F samples because of its lowest self-discharge (Section 3.3.2). The reason why this range of capacitance values was used, has not been given yet. The recommendable capacitance value depends heavily on the situations under which the energy scavenger will be used. When moments of high input power are rare, the capacitance value needs to be high enough to be able to store enough energy that can be used during the time that only limited or no input power is available. The previous chapter demonstrated the limited validity of the energy content formula, making it even more difficult to know which capacitance value is required.

Nonetheless, we did some simple calculations - using the energy content formula and assuming no

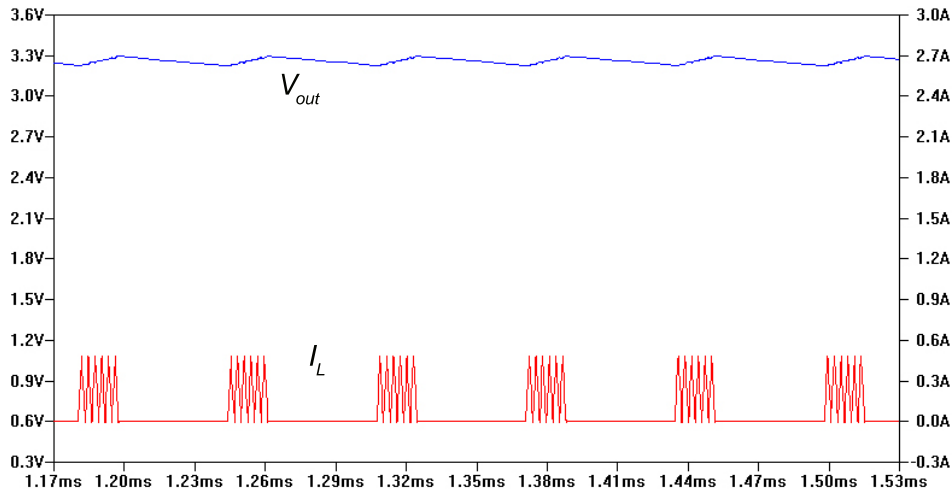


Figure 4.10: DC/DC converter in burst mode (more detail).

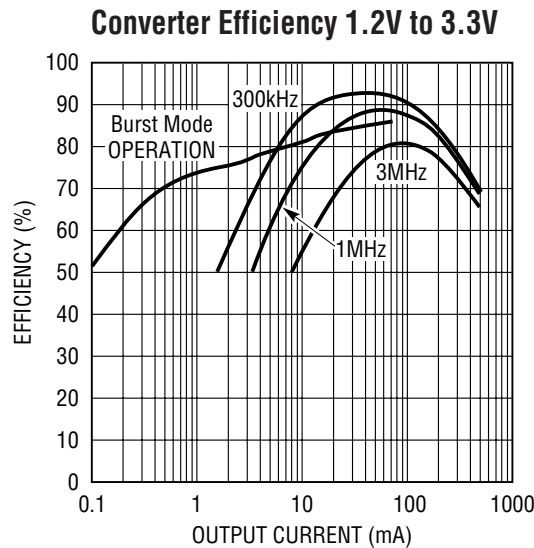


Figure 4.11: LTC3401 efficiency: step-up from 1.2V to 3.3V.

losses - to estimate how long a supercapacitor of a certain value can deliver power between 2.5 V and 1 V (approximation of minimal DC/DC converter input voltage). We assumed a constant output power of 20 mW, directly delivered by the supercapacitor. Under these circumstances, a 22 F supercapacitor can deliver power for about 48 minutes while a 50 F capacitor can deliver power for about 110 minutes. A typical sensor node consumes much less than 20 mW during stand-by (e.g. a few hundreds of μ W) but can consume the double of 20 mW when fully active. Given the low duty cycles of most sensor nodes (a few minutes fully active per hour), these capacitance values seem capable of assuring proper operation of a sensor node for more than 10 hours. A 10 hour independence is more than sufficient.

4.2.4 Complete circuit

The complete circuit of the Bologna scavenger is displayed in Figure 4.12. There is only one part of the circuit that still needs explanation: the supply of the comparator. A structure with two diodes in parallel (Schottky diodes to limit losses) leads two possible power supplies to the comparator. Only one diode can conduct at the same time and the source with the highest voltage is used as power supply. In case the supercapacitor voltage is high enough for the DC/DC converter to operate, the comparator is powered by the 3.3 V (minus voltage drop over diode) supplied by the DC/DC converter. With the supercapacitor empty and the DC/DC converter turned off, the MPP tracker is still able to work if the solar cell supplies a high enough voltage. The maximum power point of the used solar cell can be close to 3.3 V for outdoor conditions. For indoor conditions however, the MPP is always several hundreds of millivolts lower than 3.3 V. In practice the DC/DC converter will consequently always supply the comparator once the converter is turned on.

This way of supplying power to the comparator tries to ensure proper operation of the MPP tracker, even when the supercapacitor is completely discharged. There are however some situations in which the described circuit does not behave as desired. Section 4.3.6 will demonstrate this.

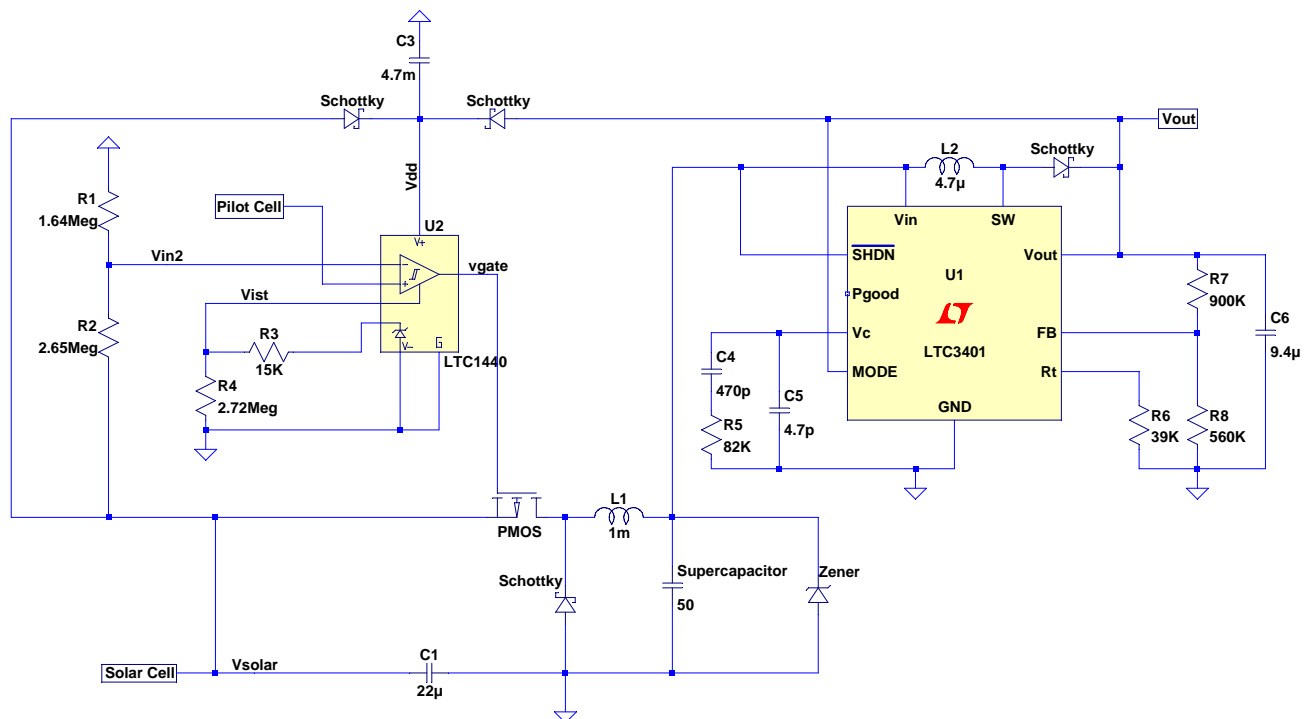


Figure 4.12: The complete Bologna scavenger circuit.

The Bologna scavenger has been implemented on a two-sided printed circuit board (PCB) of about 4 cm x 4.5 cm by the Micrel Lab of the University of Bologna. This PCB (Figures 4.13 and 4.14) was used during the measurements of which the results can be found in the next section (Section 4.3).

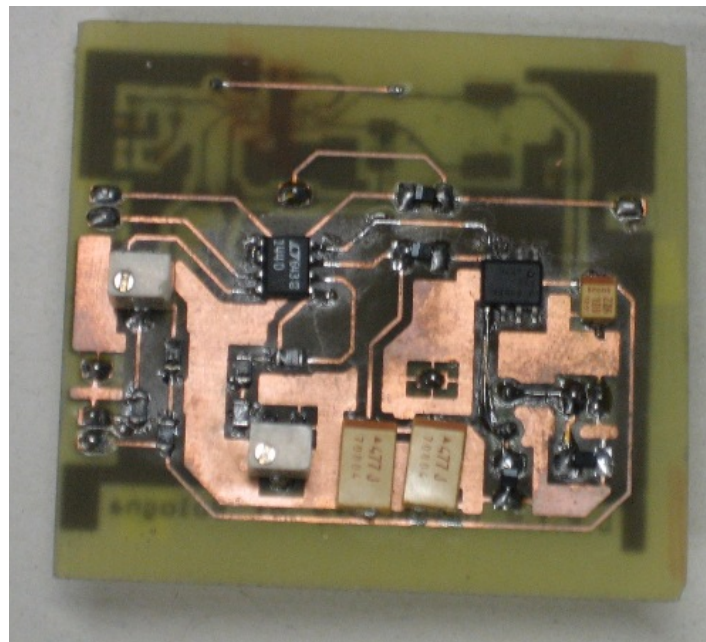


Figure 4.13: Bottom layer of the Bologna scavenger PCB.

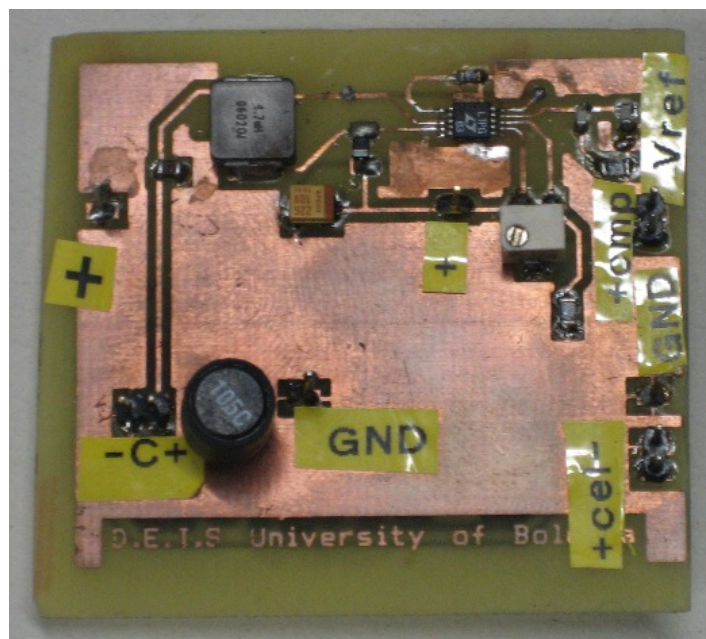


Figure 4.14: Top layer of the Bologna scavenger PCB.

4.3 Measurement results

4.3.1 Test setup

The test setup that was used in the rest of this chapter is shown in Figure 4.15 (see also Appendix A for photograph). The measured voltages are indicated by the thin arrows, the measured currents are specified by the thick ones. The BTnode is connected to the Bologna scavenger in such a way that the DC/DC converter of the node is circumvented, this to prevent the use of 2 DC/DC converters directly connected to each other. The same digital multimeter (DMM) as in the previous chapter was used (Agilent 34980A Multifunction Switch/Measure Unit with 34921A 40-Channel Armature Multiplexer). The current measurements were done by the internal shunt of the DMM, which is a resistor of $5\ \Omega$ for the observed current range. The figure includes one shunt per current measurement. In practice however, only one shunt is used. The DMM measures the voltages and currents in a consecutive way and consequently performs never more than one measurement at the same time.

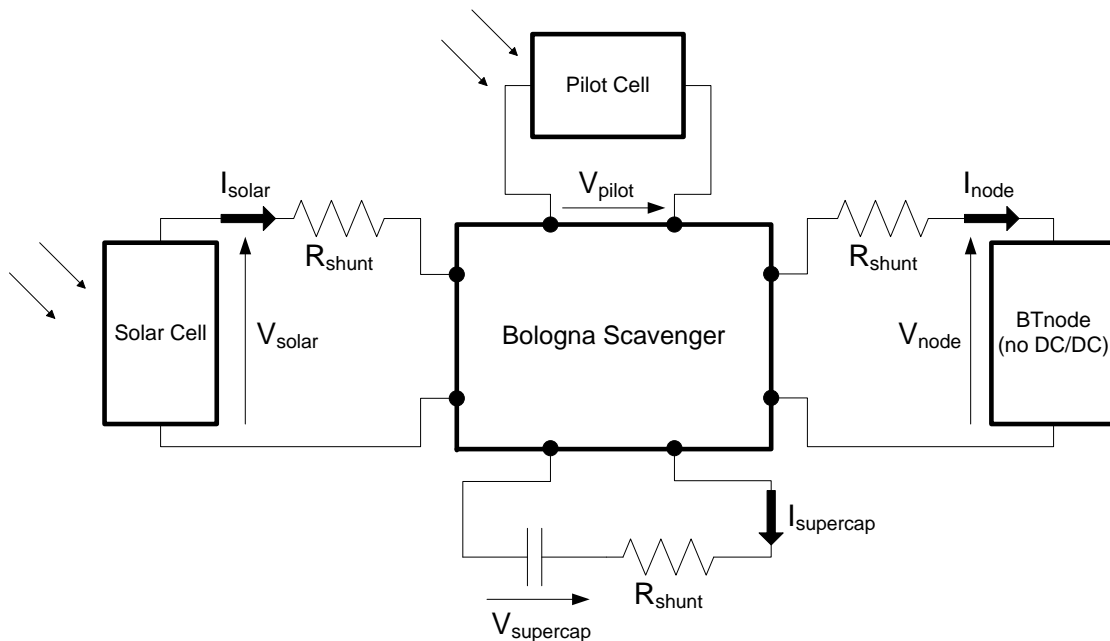


Figure 4.15: Test setup for the Bologna scavenger.

Figure 4.16 demonstrates how the 34921A multiplexer measures multiple channels. The integration time is the time during which one channel (can be current or voltage) is measured through an integrating or averaging process. The standard integration time is 1 PLC (Power Line Cycle) or 20 ms, which is the period of the 50 Hz power line connected to the DMM. This integration time allows to filter the noise of the power lines out of the measured signals. This also means that the values obtained through the DMM are averages over the whole integration time. The MPP tracker works at frequencies of tens of kHz while the DC/DC converter works at frequencies up to 1MHz. The majority of the signals

measured in the test setup of Figure 4.15 have consequently much smaller periods than the integration time, which should make the averaging process quite accurate. For all measurements, the standard integration time of 1 PLC was used.

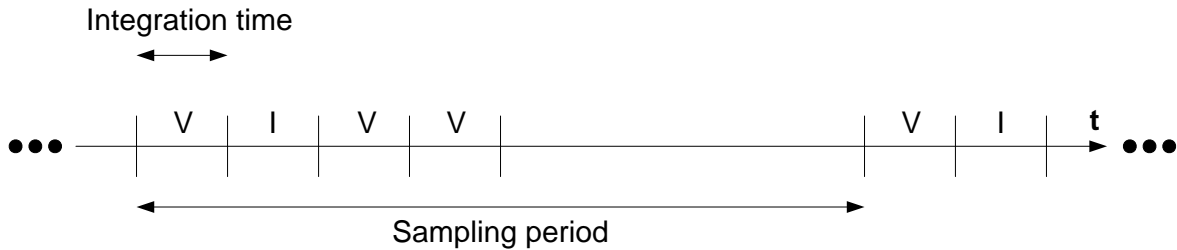


Figure 4.16: Principle of the Agilent 34921A 40-Channel Armature Multiplexer.

Once all the desired channels are measured, the DMM waits until the end of the sampling period (one second for all experiments) to start a new sequence of measurements. The samples are not taken simultaneously and therefore there is a time difference between the different measured averages of the same sampling period. This difference is however not more than 140 ms. The charging and discharging of the supercapacitor is a much slower process with e.g. an increase of less than 1 mV per second for $V_{supercap}$. The changes in the waveforms during 140 ms are therefore very limited. In calculations, the measurements of the different channels during the same sampling period can be considered as simultaneous.

The solar cell and the pilot cell were illuminated by a desk lamp with adjustable light intensity. The distance between lamp and solar cell was 12 cm. It would have been possible to choose for a smaller distance to increase the maximum power delivered by the solar cell. Then however, temperature effects would have played a much bigger role than they already played for this test setup (see Section 4.3.3). Figure 4.17 shows the VI and the VP curve for the highest light intensity of the desk lamp. The maximum obtainable power delivered by the solar cell is then about 85 mW.

It is of course interesting to know how this compares to the powers that can be achieved when outdoor light is available - lab was lit by artificial light only. Figure 4.18 depicts the VI and VP curves for the solar cell, still placed inside but close to an outside window during a normal sunny day in Zurich. In such a situation, a maximum obtainable power of almost 120 mW can be achieved. Also interesting is the available power in the lab environment without the additional lighting of the desk lamp and with the solar cell in the middle of the room on a Table (Figure 4.19). The maximum power is then only $90 \mu\text{W}$. Apparently, a lot of artificial light or an average amount of outside light is needed to obtain an acceptable amount of power from the solar cell.

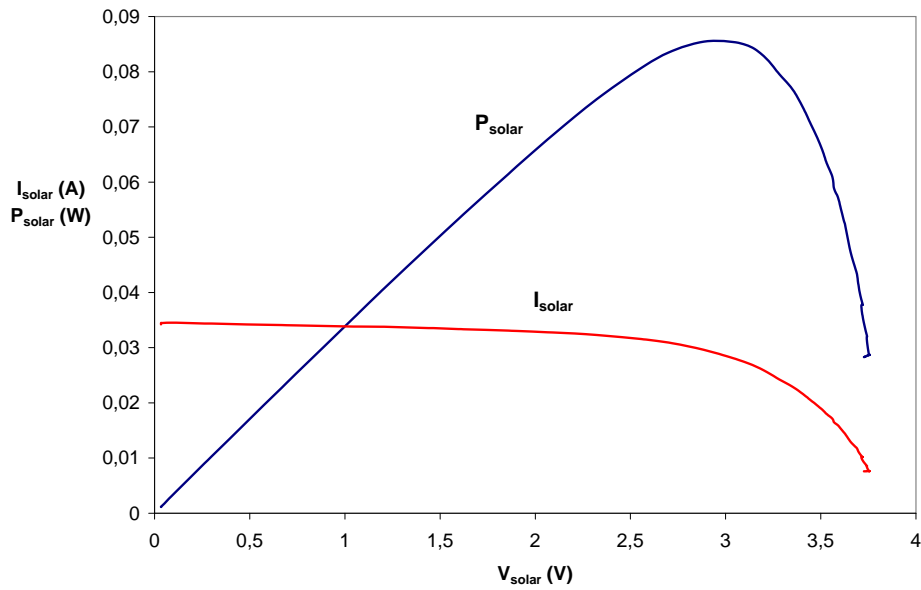


Figure 4.17: VI and VP curve: maximum obtainable power for test setup.

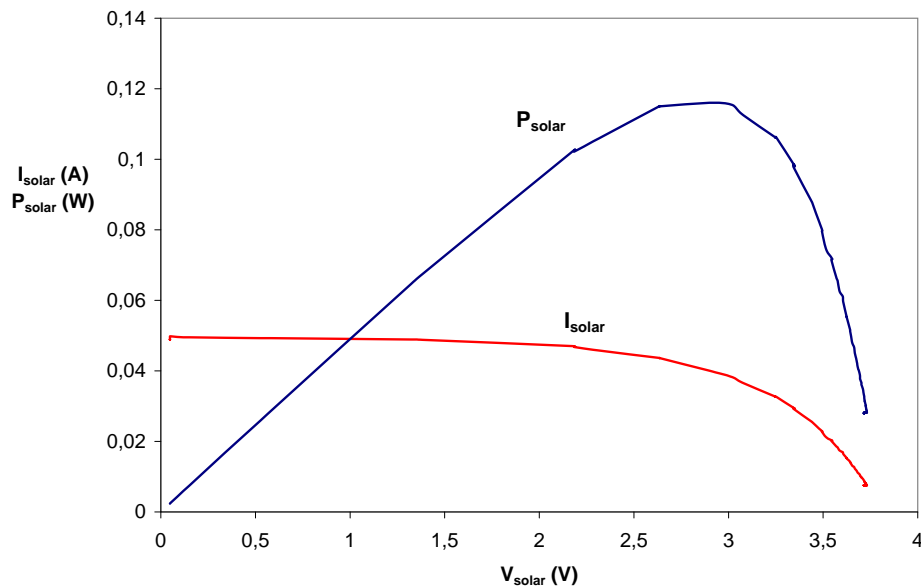


Figure 4.18: VI and VP curve: behind window during typical sunny day.

4.3.2 Relation between main solar cell and pilot cell

An important assumption that was made during the conception of the Bologna scavenger was the linear relation between the V_{mpp} of the main solar cell and the open circuit voltage of the pilot cell (V_{pilot}), irrespective of the light intensity. This relation was checked for the described test setup and the results can be seen in Figure 4.20. The linear relation between the open circuit voltage of the main solar cell (V_{oc}) and the open circuit voltage of the pilot cell is quite accurate. The relation

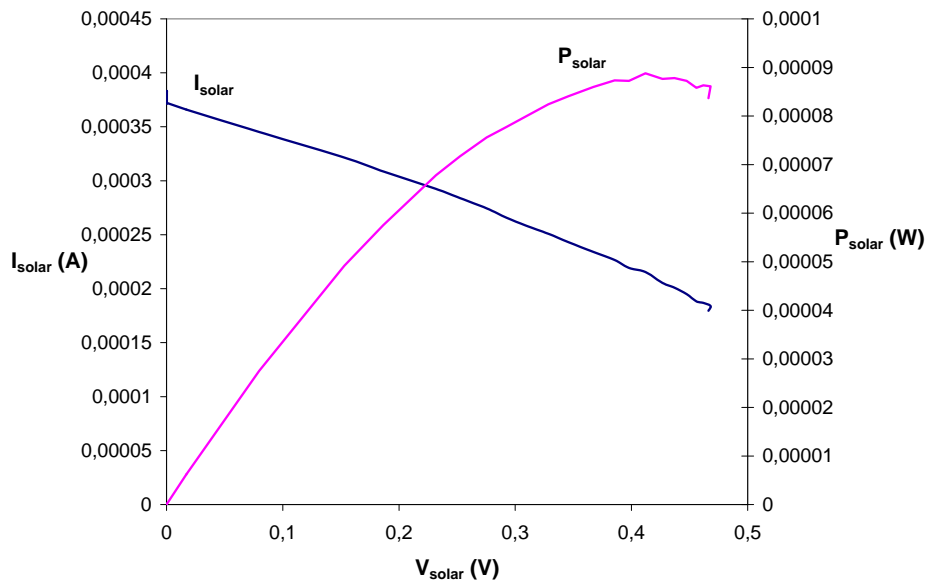


Figure 4.19: VI and VP curve: lab environment without additional lighting.

between V_{mpp} and V_{pilot} shows however some significant unlinear behaviour, especially for the lower light intensities. This is also demonstrated in Figure 4.21 where the ratio between V_{mpp} and V_{pilot} is displayed. The difference between the ratio for the two lowest light intensities is almost 20% of the lowest light intensity ratio.

The voltage dividers that deliver the voltage of the solar cell and the pilot cell to the inputs of the comparator can be configured in such a way that the solar cell is forced to operate in its maximum power point. During operation they remain however fixed. Especially when the solar cell is used in a changing environment of low light intensity, this can lead to substantial losses. When the light condition changes, the solar cell will be forced to work around a voltage that is different from its V_{mpp} . Especially when this voltage is higher than the actual V_{mpp} , the losses cannot be neglected as the VP curve is falling quite fast in this voltage region.

4.3.3 Temperature influence

We already mentioned temperature influence as a reason for not decreasing the distance between the lamp and the solar cell. According to its datasheet, the main solar cell has temperature coefficients of $-16 \text{ mV}/^\circ\text{C}$ and $0.15 \text{ mA}/^\circ\text{C}$. A desk lamp can generate a lot of heat and especially for small distances this can heat up the solar cell to more than 60 degrees Celsius. Also a solar cell close to the window in a lot of sun can heat up with several tens of degrees Celsius. A distance of 12 cm between solar cell and lamp was a compromise between less heating and more power (maximum power as close as possible to power for outdoor light situation of Figure 4.18). Still, the influence of temperature for this distance was quite high because of the high - in absolute value - temperature coefficients.

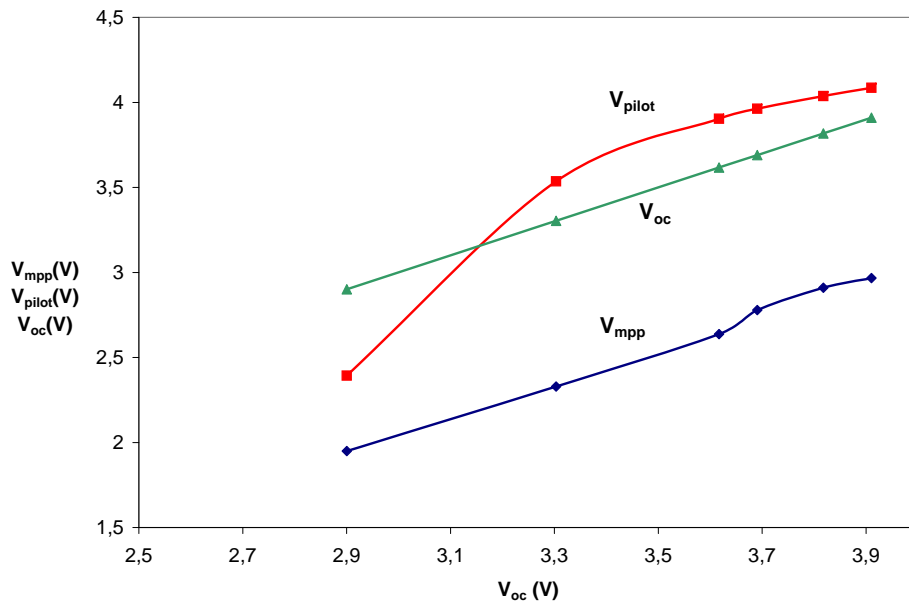


Figure 4.20: Relation between V_{oc} , V_{mpp} and V_{pilot} .

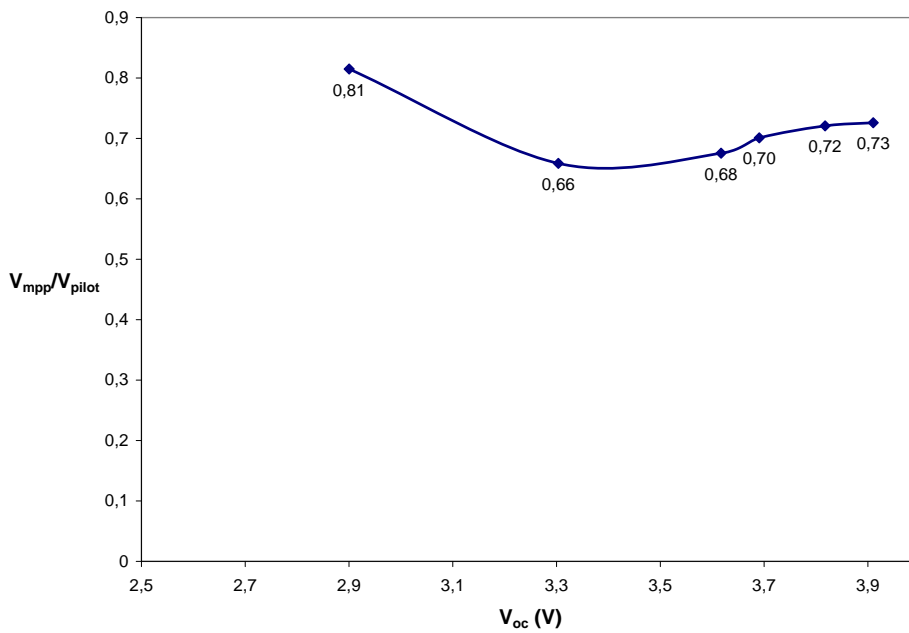


Figure 4.21: Ratio of V_{mpp} and V_{pilot} as a function of V_{oc} .

The solar cell of the test setup was illuminated by the desk lamp for an hour, starting with the cell at room temperature. Every six minutes the VI and VP curves were measured to investigate the influence on the solar cell's characteristics of the heat generated by the lamp. The results can be found in Figures 4.22 and 4.23. After 36 minutes the curves stabilized with a maximum power point that was 13 mW lower than the initial MPP. Figure 4.24 shows the continuation of the experiment with the lamp turned

off after 1 hour of being turned on. The lowest VP curve in this graph was measured at the end of the one hour period that the lamp was on. The other curves were measured 10 and 20 minutes afterwards. The curve measured after 20 minutes is already the same as the curve observed at the beginning of the experiment. Apparently, for the selected test setup, the cooling takes place at a higher rate than the heating.

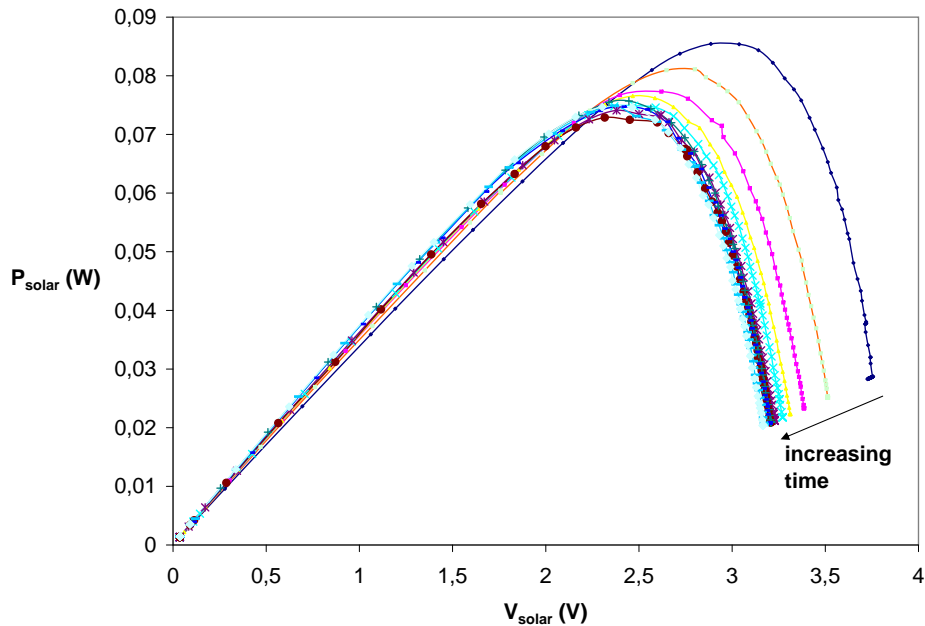


Figure 4.22: Temperature influence on VP curve of solar cell: lamp on.

The test results demonstrate how the maximum power that can be delivered by a solar cell decreases with an increasing temperature (for a constant light condition). This problem can be made worse if the relation between V_{mpp} and V_{pilot} changes with a changing temperature. In that case, the voltage around which the solar cell is forced to operate, changes in a different way than the actual maximum power point voltage. This reduces the delivered solar cell power even more since the solar cell does not continue to work in its MPP. The evolution over the course of the whole experiment of the ratio V_{mpp}/V_{pilot} is depicted in Figure 4.25. The ratio is represented as a percentage, with the ratio measured at the beginning of the experiment as base. At the end of the period during which the lamp was on, the ratio is 13.5% lower than its initial value. It is clear that the accuracy of the MPP tracker is not guaranteed during periods of long illumination, even when the voltage dividers were configured correctly at the beginning of functioning. The results were obtained for a specific test setup and environment. External factors like airconditioning can change the way the solar cell is influenced by the desk lamp's heat.

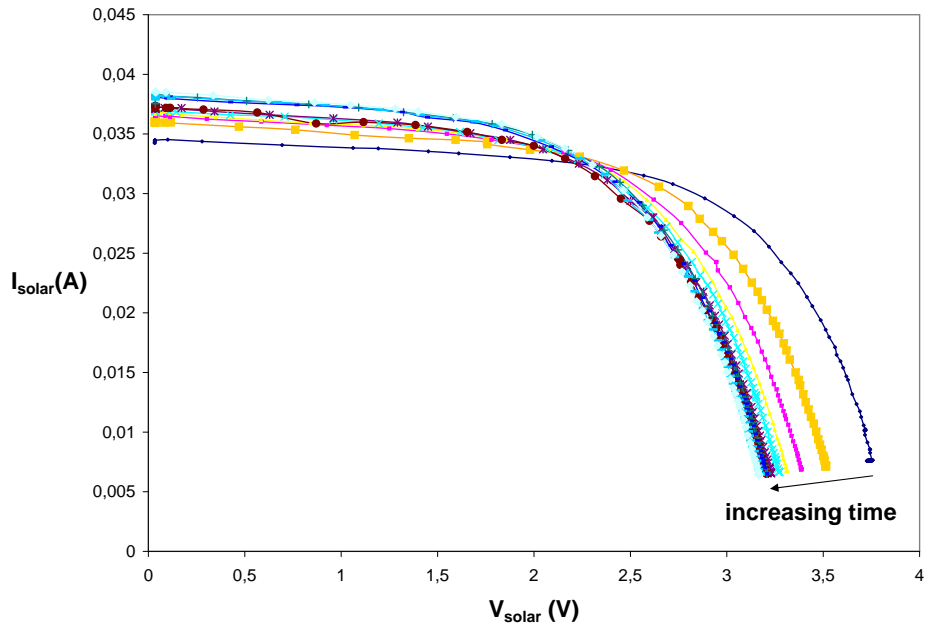


Figure 4.23: Temperature influence on VI curve of solar cell: lamp on.

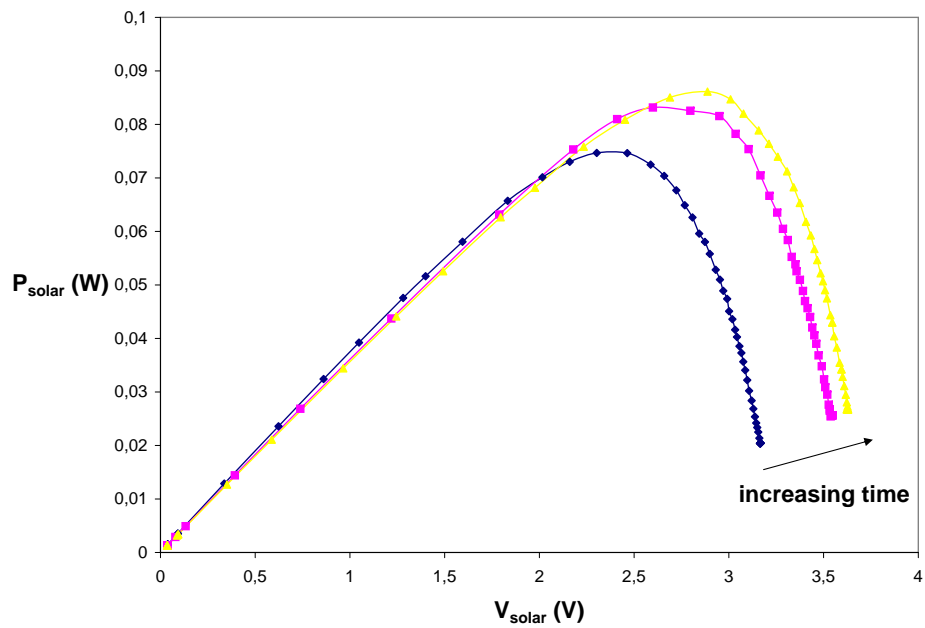


Figure 4.24: Temperature influence on VP curve of solar cell: lamp off.

4.3.4 Normal operation

In this section, the normal and intended operation of the Bologna harvester is demonstrated (Figure 4.26). At the beginning of the experiment, the supercapacitor has a voltage that is a little bit higher than the minimum allowed DC/DC converter input voltage. The BTnode operating system is on but

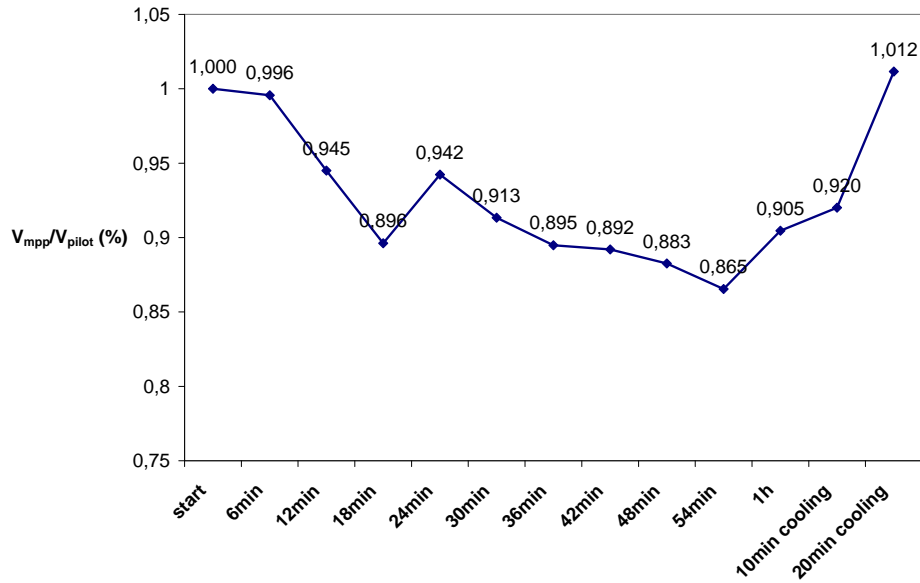


Figure 4.25: Temperature influence on relation between V_{mpp} and V_{pilot} .

does not execute additional tasks. The voltage dividers were configured correctly before the start of the experiment. The lamp is at its maximum intensity and because more energy is supplied by the solar cell than is consumed by the BTnode, the supercapacitor is charged. The moment $V_{supercap}$ reaches 1.8 V, the light intensity of the lamp is reduced. Now more power is consumed than delivered, leading to a discharge. Why the charging was stopped at 1.8 V will be explained in the next section. The open circuit voltage of the pilot cell (not displayed in the graph) decreases when the light intensity is lowered and therefore the voltage around which the solar cell is forced, also decreases. The MPP tracker seems to work as desired.

Figure 4.27 shows every $V_{solar}-P_{solar}$ combination registered over the course of the experiment. A lot of dots are concentrated around the two $V_{solar}-P_{solar}$ combinations to which the solar cell was forced by the MPP tracker. The two dots further away from the two concentration areas were measured during the transition from one light intensity to the other. One can however also see that V_{solar} and P_{solar} change for the same light condition since the dots of the same concentration areas do not completely overlap. This is the temperature influence at work. V_{pilot} changes with the temperature and consequently the forced solar cell voltage changes too. The green line connects consecutive samples and one can actually see that during the low light condition V_{solar} and P_{solar} increase. After all, during the low light condition the lamp generates less heat which allows the solar cell and the pilot cell to gradually cool down. The same phenomenon can be seen for the high light condition. The light intensity changes once and the temperature of the solar cell changes continuously over the course of the experiment. It is very difficult to say how the ratio V_{mpp}/V_{pilot} evolves and how accurate the MPP tracker stays during the experiment.

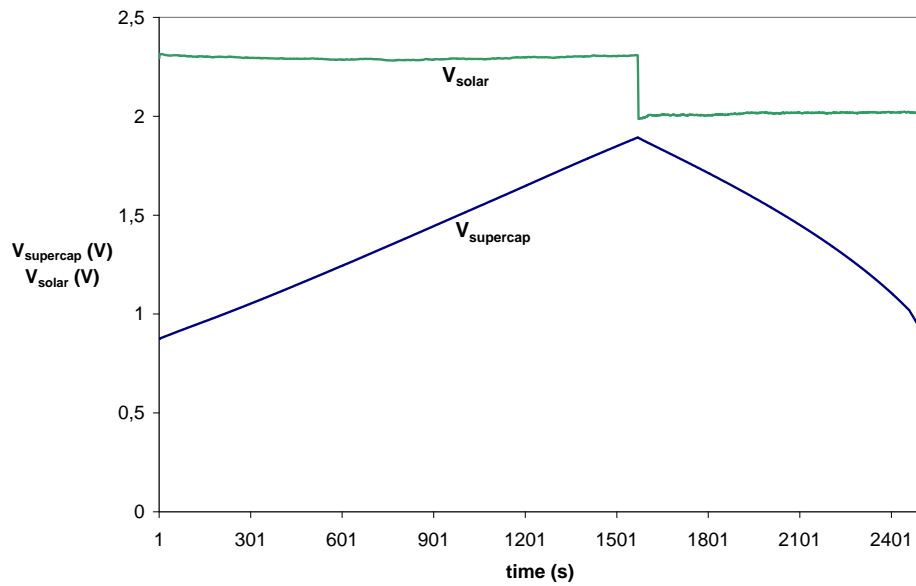


Figure 4.26: Normal operation: V_{solar} and $V_{supercap}$.

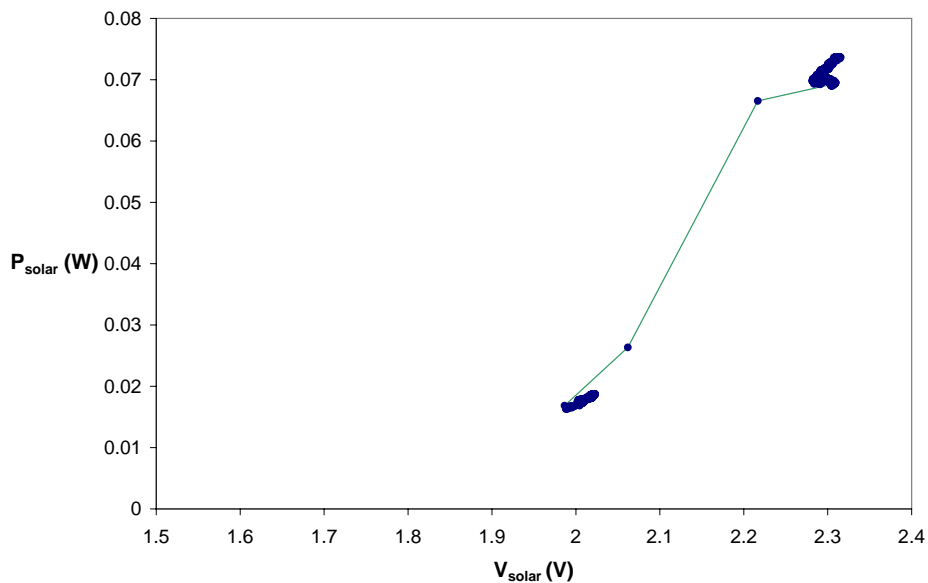


Figure 4.27: Normal operation: P_{solar} as a function of V_{solar} .

4.3.5 Unwanted behaviour

Figure 4.28 shows a similar charging process as in the previous section. This time however, the charging continues until $V_{supercap}$ reaches 2.5 V, the maximum allowed voltage over the supercapacitor. During charging, the difference between the as good as constant V_{solar} and the increasing $V_{supercap}$ decreases. We already explained in Section 4.2.1 how this leads to a lower average inductor current and which implications this has on the working principle of the MPP tracker. When V_{solar} and $V_{supercap}$

get too close, an unwanted effect can be observed. V_{solar} drops, the MPP tracking stops and V_{solar} starts to follow $V_{supercap}$ with a constant voltage difference between them.

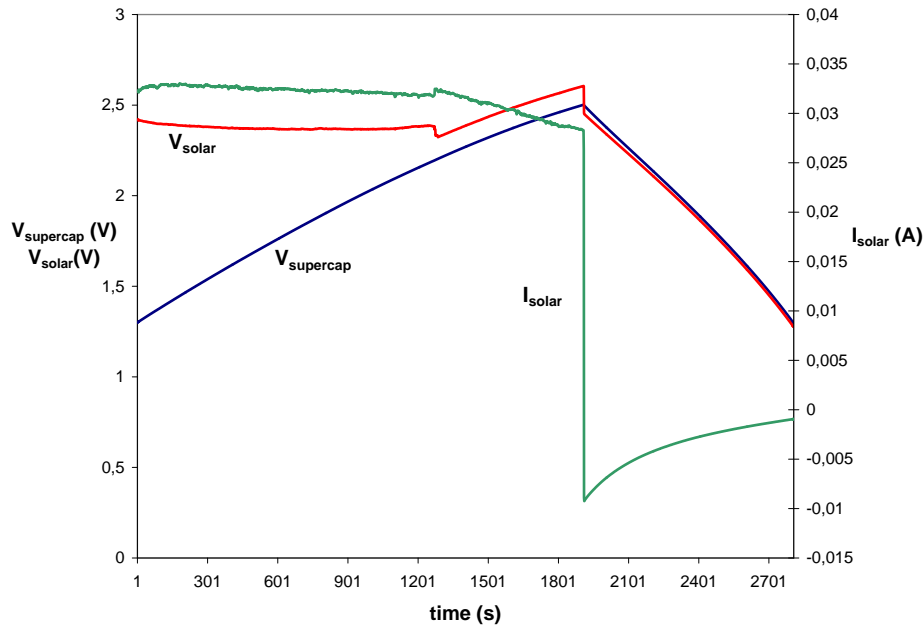


Figure 4.28: Unwanted behaviour: V_{solar} , $V_{supercap}$ and I_{solar} .

This phenomenon can be explained best through waveforms obtained with an oscilloscope. Figures 4.29, 4.30, 4.31, 4.32, 4.33 and 4.34 display oscilloscope screenshots for different $V_{supercap}$ voltages in an increasing order. The solar cell voltage and the control signal of the PMOS transistor (V_{gate}) are plotted. The period during which the transistor is open (V_{gate} is high), appears to be independent of $V_{supercap}$. This is not surprising since $V_{supercap}$ has no influence on the charging process of the input capacitor C_{in} . The period during which the transistor is closed increases however substantially with an increasing $V_{supercap}$. Starting from $V_{supercap} = 2.2$ V, the solar cell voltage shows a continued increase after the switch has been closed. This indicates that at the moment the switch closes, the inductor current is smaller than the solar cell current. Only when the inductor current has risen above I_{solar} , V_{solar} starts its decline. Eventually the MPP tracking stops and for $V_{supercap} = 2.3$ V, the switch remains closed ($V_{gate} = 0$ V) and the solar cell voltage is constant.

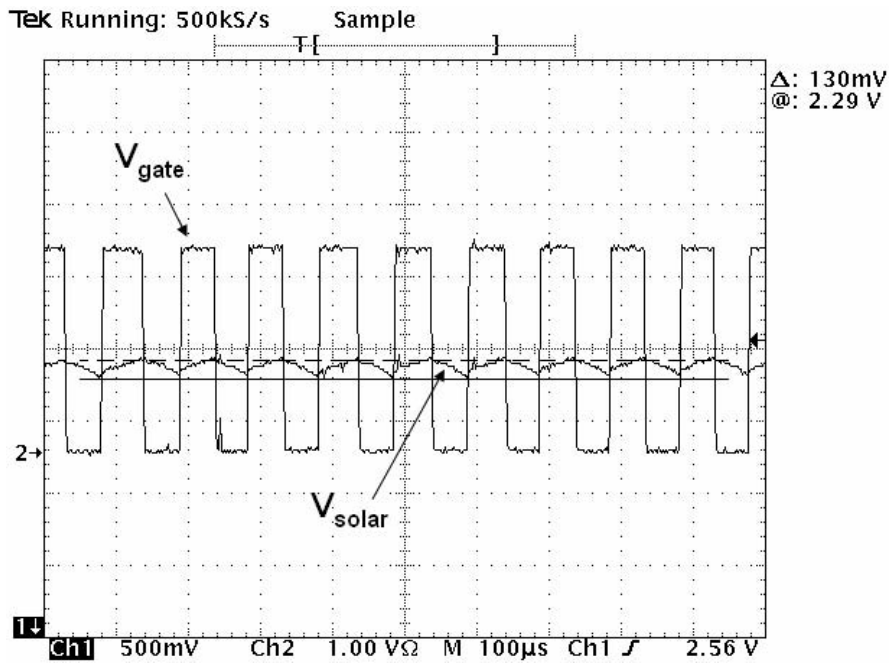


Figure 4.29: Oscilloscope screenshot of V_{solar} and V_{gate} : $V_{supercap} = 0.9\text{ V}$

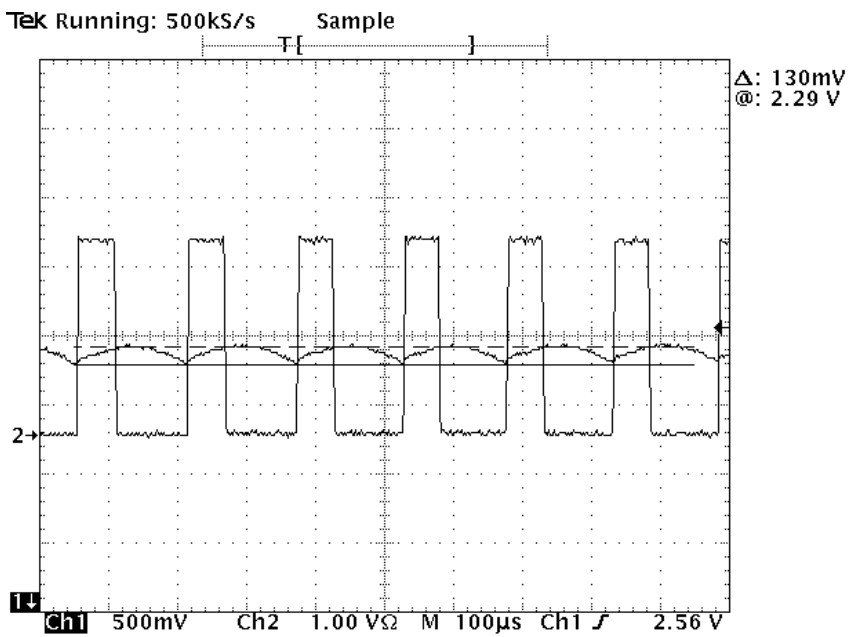


Figure 4.30: Oscilloscope screenshot of V_{solar} and V_{gate} : $V_{supercap} = 1.4\text{ V}$

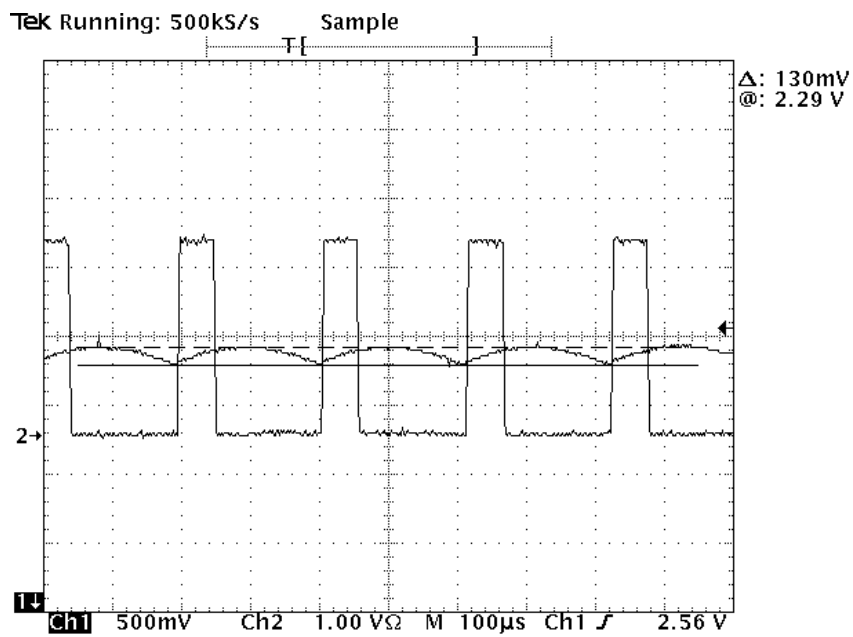


Figure 4.31: Oscilloscope screenshot of V_{solar} and V_{gate} : $V_{supercap} = 1.8 V$

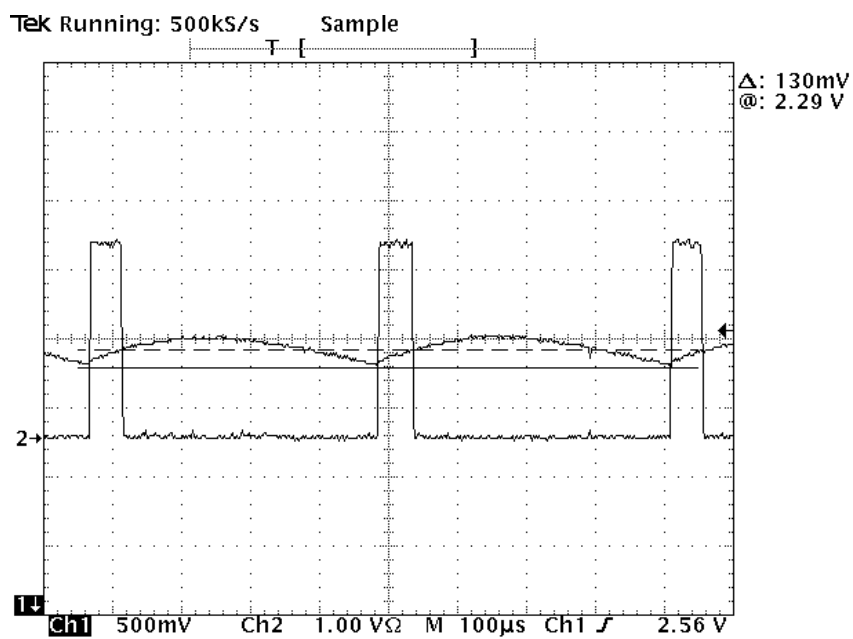


Figure 4.32: Oscilloscope screenshot of V_{solar} and V_{gate} : $V_{supercap} = 2.2 V$

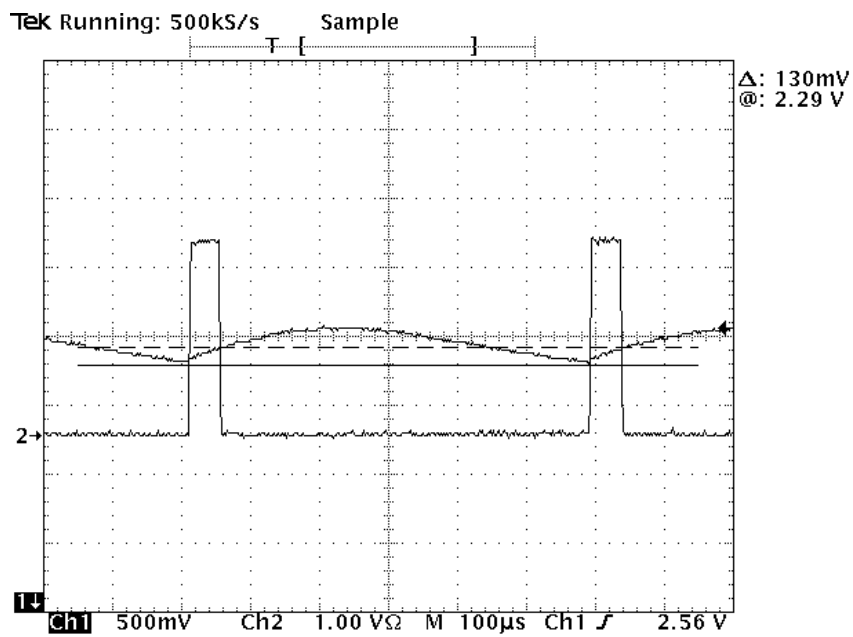


Figure 4.33: Oscilloscope screenshot of V_{solar} and V_{gate} : $V_{supercap} = 2.28$ V

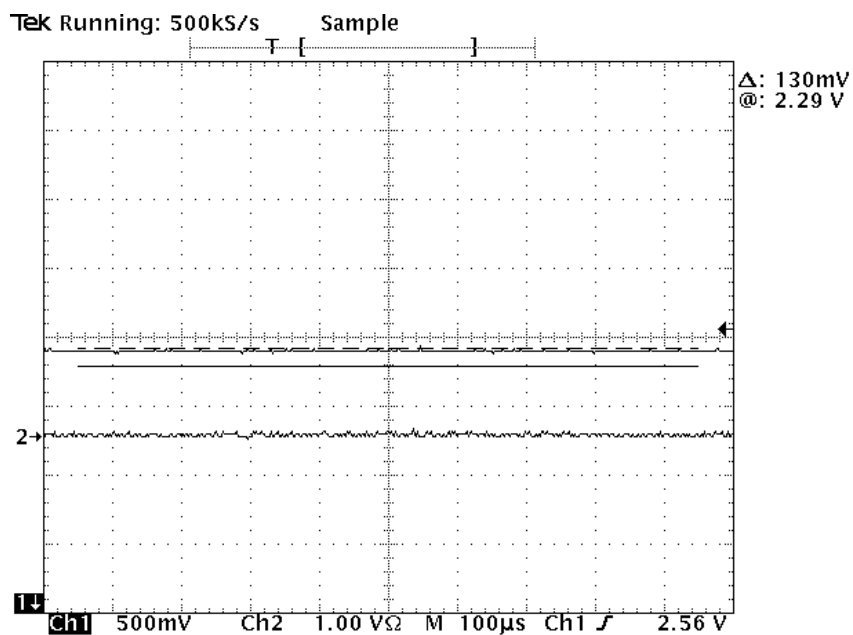


Figure 4.34: Oscilloscope screenshot of V_{solar} and V_{gate} : $V_{supercap} = 2.3$ V

To get an even better picture of the phenomenon, waveforms of the current going to the supercapacitor are included in this section (Figures 4.35, 4.36, 4.37, 4.38 and 4.39). These currents were measured

by external shunts of $0.5\ \Omega$ instead of the internal shunt of the DMM. The reason for this choice will be given in Section 5.2. Because of this shunt value, the voltages in the oscilloscope screenshot need to be multiplied with two to obtain the actual supercapacitor current.

The negative spikes in the current are caused by the DC/DC converter. For a higher supercapacitor voltage, less spikes per burst and a lower burst frequency can be observed. The DC/DC converter's efficiency decreases for a decreasing input voltage. Especially in the low input voltage range, the efficiency is quite sensitive to the input voltage level. For the same output power (BTnode draws constant average current), the DC/DC needs much more power for an input voltage of 1 V than for an input voltage of 1.4 V. This explains the big difference in amount of spikes between Figures 4.35 and 4.36.

The DC/DC converter current and the lower frequency inductor current can be easily distinguished. For a higher $V_{supercap}$, the period during which the inductor current rises (switch closed) increases while the increase rate of the current decreases. For $V_{supercap} = 2.3\ \text{V}$, the current going into the supercapacitor is constant, excluding limited noise and the negative DC/DC converter spikes. This indicates that the MPP tracking has been stopped.

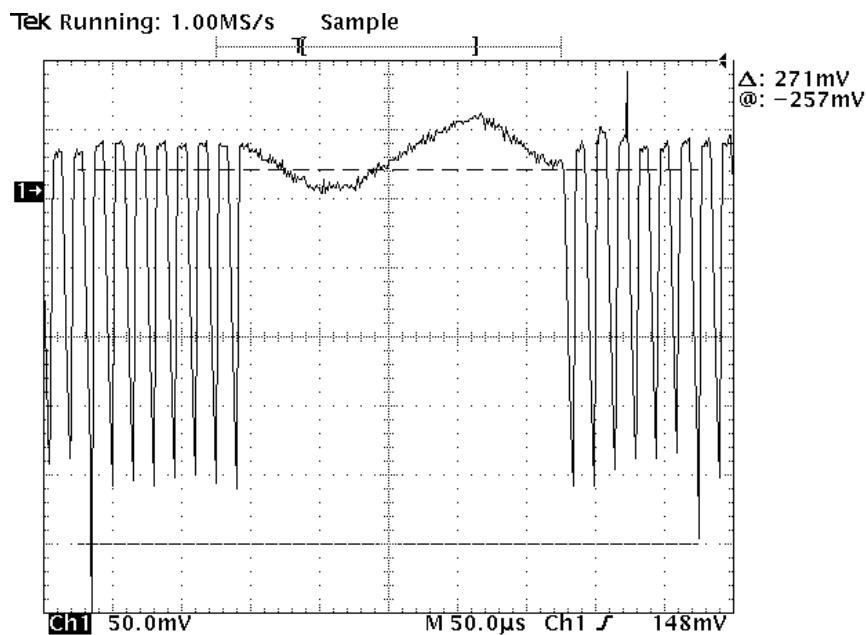


Figure 4.35: Oscilloscope screenshot of $I_{supercap}$: $V_{supercap} = 1\ \text{V}$

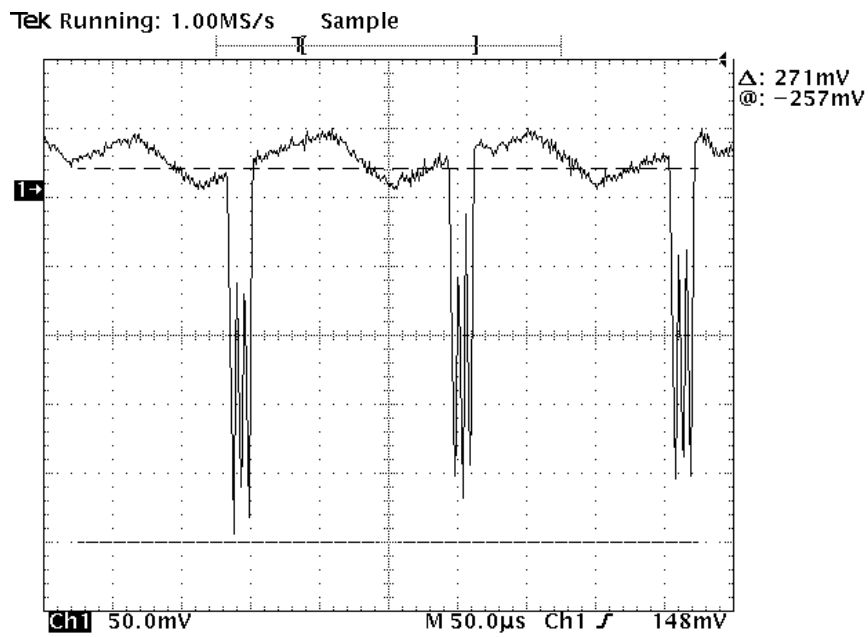


Figure 4.36: Oscilloscope screenshot of $I_{supercap}$: $V_{supercap} = 1.4$ V

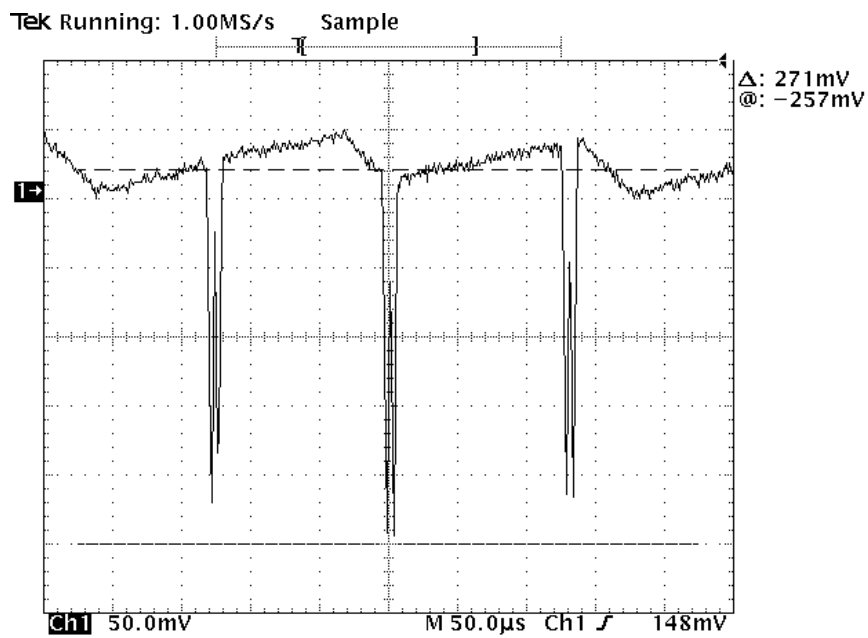


Figure 4.37: Oscilloscope screenshot of $I_{supercap}$: $V_{supercap} = 1.8$ V

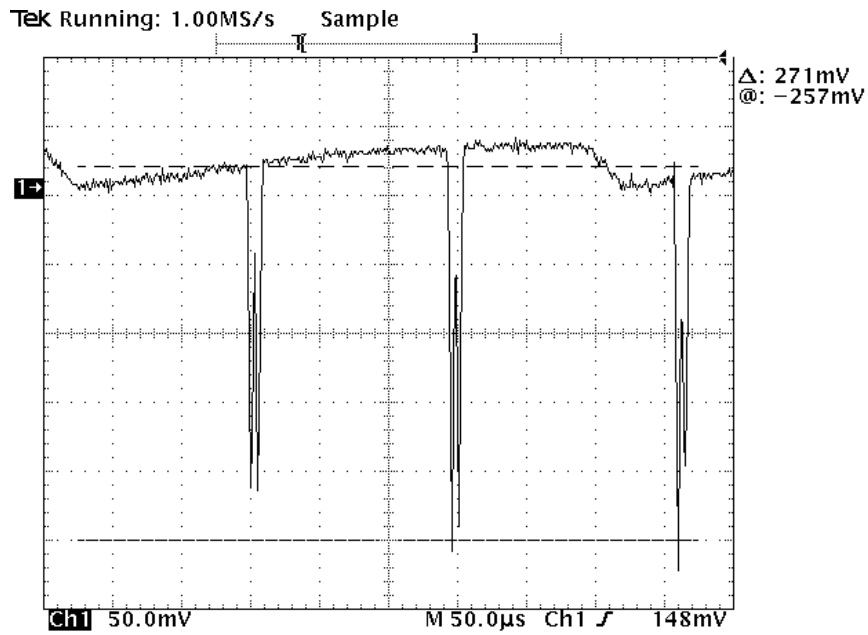


Figure 4.38: Oscilloscope screenshot of $I_{supercap}$: $V_{supercap} = 2.2$ V

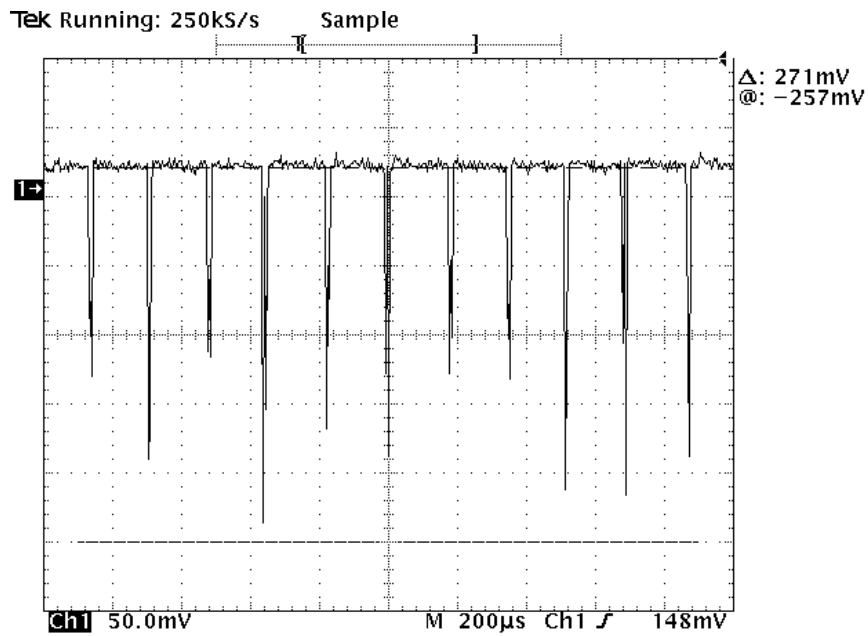


Figure 4.39: Oscilloscope screenshot of $I_{supercap}$: $V_{supercap} = 2.3$ V
(Sampling rate is 4 times lower than for other $I_{supercap}$ waveforms).

Figure 4.40 presents a simulation that shows the end of the MPP tracking. The values in the plot are not really comparable with the voltages and currents observed during our test setup but the simulation can nonetheless be used to demonstrate the concept of what happens. While normally the inductor current is always higher than the solar cell current (see Figure 4.5), one can see that in the case of $V_{supercap}$ close to V_{solar} , the currents oscillate around each other. One can also notice a decrease of I_L before the steep decrease caused by the opening of the switch. This decrease indicates that the voltage over the inductor is negative. The lower boundary for V_{solar} is at that point lower than $V_{supercap}$ since V_{solar} can go below $V_{supercap}$ without causing the switch to be opened. At a certain point, the decrease of I_L causes an increase of V_{solar} before reaching the lower boundary. The current I_L increases, V_{solar} decreases and eventually a transitional oscillation takes place.

The transitional oscillation of V_{solar} settles at a value higher than the lower boundary of the allowed voltage band. The switch stays open and all AC phenomena die out. The voltage difference of about 100 mV between V_{solar} and $V_{supercap}$ in Figure 4.28 is caused by the voltage drop over the internal resistance of the inductor and the equivalent resistance of the PMOS transistor. Starting from the moment the MPP tracking stops, V_{solar} is completely determined by $V_{supercap}$.

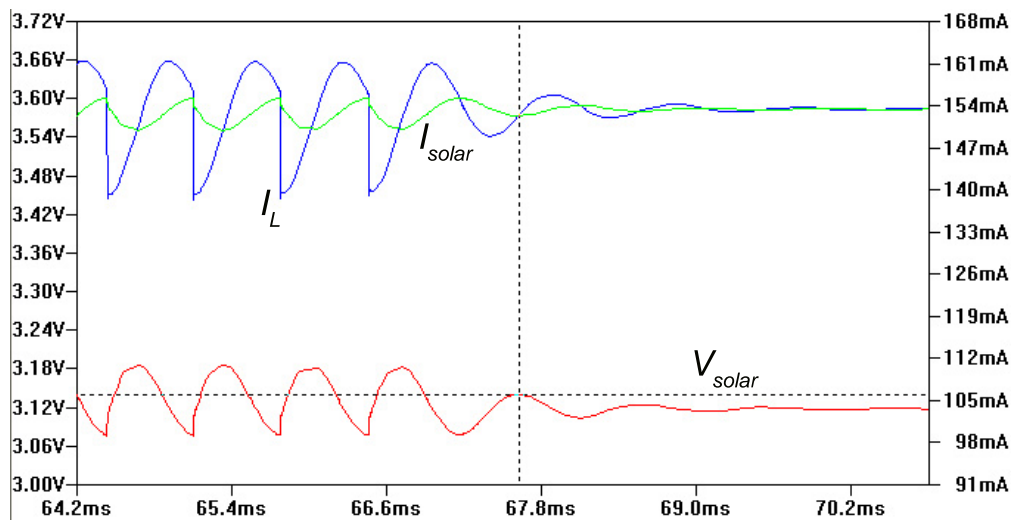


Figure 4.40: MPP tracking operation ends.

We now return to Figure 4.28. The moment V_{solar} reaches 2.5 V, the desk lamp is completely turned off. In the mentioned graph one can observe that also during discharging the MPP tracking does not work. The pilot cell tries to force a much lower voltage over the solar cell than the value the cell has the moment the light intensity is reduced. Consequently the switch stays closed. The voltage over the supercapacitor is however much higher than the open circuit voltage of the solar cell when the desk lamp is turned off. Consequently, the solar cell experiences reverse current, a serious shortcoming of this circuit. It means that a charged supercapacitor is discharged during periods that its voltage is higher than the open circuit voltage of the solar cell (periods of low light intensity). This discharge

even takes place when the sensor node itself does not consume any energy. Once V_{solar} is lower than the lower boundary of the voltage band the pilot cell controls, the switch will open again, starting the MPP tracking.

The described phenomenon was also the reason behind the choice of 1.8 V as maximal $V_{supercap}$ during the experiment that demonstrated normal operation. We had to make sure that the difference between $V_{supercap}$ and V_{solar} remained more than 100 mV, even for the low light condition (that was not chosen too low), to keep normal MPP tracking going.

The sudden shift of V_{solar} and I_{solar} when the MPP tracking stops, has not been explained yet. This shift is caused by the fact that the measured values are averages. As long as the MPP tracking works, V_{solar} and I_{solar} oscillate. The averages of these oscillating signals are higher than the DC value they obtain after the oscillating has stopped, causing the shift. The averaging process can also explain the slow increase of V_{solar} in Figure 4.28 before the shift. One would expect a decrease caused by the heating of the pilot cell. The waveforms of V_{solar} and I_{solar} change however during charging and this can also cause a slight change in their average values, in this case an increase.

Finally, Figure 4.41 depicts all the $V_{solar} - P_{solar}$ combinations that were recorded during the experiment. The point in which the solar cell was forced during MPP tracking can be easily distinguished. The points recorded during charging without MPP tracking form a sequence of points with an increasing V_{solar} . Excluding temperature effects, these points follow the VP curve of the solar cell for the light condition under which the solar cell operated during charging. P_{solar} stays quite stable which indicates that the solar cell was working very close to its MPP, on the top of the VP curve. The combinations that were registered during discharging have a negative P_{solar} .

4.3.6 Comparator power supply issue

Section 4.12 already described the ways through which the comparator can be supplied with power. Even when the supercapacitor is insufficiently charged to turn on the DC/DC converter, the comparator and hence the MPP tracker can function properly thanks to the connection between the solar cell and the comparator supply pin. This feature has been successfully tested for a test setup with a distance of less than 10 cm between desk lamp and solar cell. For our standard test setup with a distance of 12 cm however, even the maximum light intensity did not suffice for a proper operation of the MPP tracker.

Figure 4.42 depicts an experiment through which the supply function of the solar cell for the comparator was tested. The light intensity of the lamp was chosen at its maximal value and the supercapacitor was completely discharged at the start of the experiment. For about 70 minutes the solar cell was kept disconnected but at the same time illuminated by the desk lamp. This was done to demonstrate the influence of the heat of the lamp on the open circuit voltage of the solar cell.

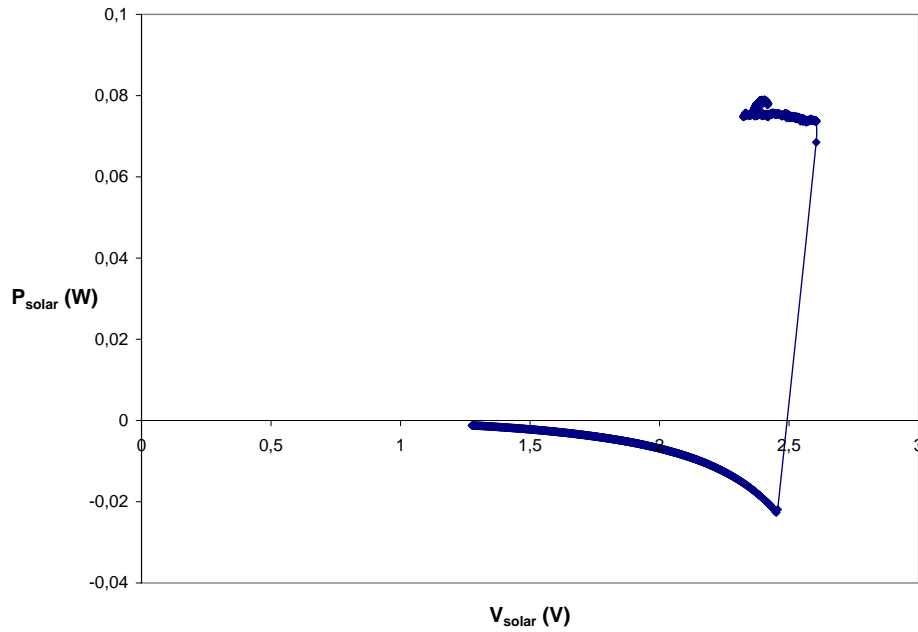


Figure 4.41: Unwanted behaviour: P_{solar} as a function of V_{solar} .

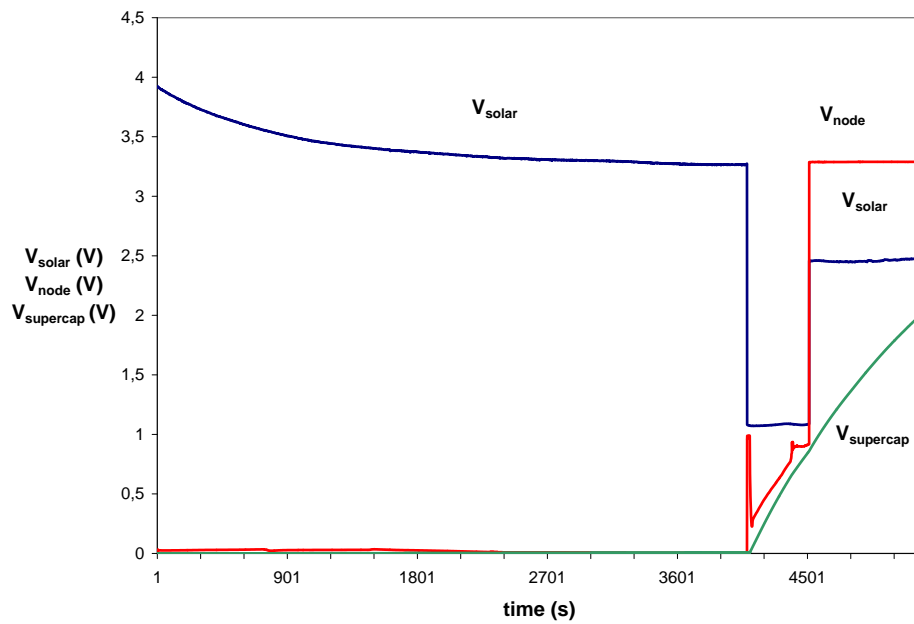


Figure 4.42: Comparator supply issue: V_{solar} , V_{node} and $V_{supercap}$.

The moment the solar cell is connected to the Bologna scavenger, the solar cell voltage jumps to 1.08 V. This voltage is not at all high enough to power the comparator (minimum supply voltage is 2 V), especially when the voltage drop over the Schottky diode is taken into account. Consequently the comparator is turned off, the PMOS transistor is closed and the supercapacitor is charged with a DC

current. One can notice a steep temporary jump of V_{node} after the solar cell is connected, indicating that the DC/DC converter tries to start up but fails. During the charging, V_{node} increases together with $V_{supercap}$. V_{node} remains a little bit higher than $V_{supercap}$ because the charge that was stored on the output capacitor of the DC/DC converter during the start-up attempt has no other place to go to. Eventually $V_{supercap}$ is high enough to turn on the DC/DC converter and the moment the converter is on, V_{solar} jumps. At that point, the MPP tracker is functioning, powered by the DC/DC converter.

This example proves that enough solar cell power needs to be available for the alternative comparator supply to work. The moment the solar cell is connected to the scavenger, its voltage starts to decrease. The solar cell needs to deliver enough power to ensure that the comparator is capable of opening the transistor switch before V_{solar} falls below the minimum supply voltage of the comparator. Otherwise the transistor stays closed, allowing V_{solar} to decrease even more and preventing the solar cell of being used as power supply.

Chapter summary and conclusions

This chapter discussed the working principle of the Bologna scavenger with attention for the many influences on its behaviour. The values of the several circuit components were kept unchanged compared to the original design from the University of Bologna. There is however a lot of research that can be done on the influence of the components on the overall performance of the circuit.

A suggestion for the MPP tracker is for example the use of a higher input capacitor and a higher inductor to reduce the frequency of the switch and consequently the switching losses. The optimal value for the hysteresis of the comparator is another subject that could be investigated. A smaller hysteresis will ensure that the solar cell is confined to a smaller voltage range. This can lead to a higher average output power if the MPP tracker is configured correctly, since the solar cell will spend much more time close to its MPP. This chapter however demonstrated how fast the accuracy of the tracker can change under changing conditions, making the case for more hysteresis. If the voltage around which the solar cell is forced to operate is different from the maximum power point voltage, more hysteresis can make sure that at least some time of one switching period is spent close to the MPP. A smaller hysteresis will also lead to a higher switching frequency, which should be taken into account.

This chapter identified some serious shortcomings of the Bologna scavenger. Especially for conditions of low light intensity the scavenger seems inadequate. Under these conditions, the MPP tracker does not work for the majority of the time while the extra losses remain. For some problems, easy solutions can be considered. A Schottky diode between the solar cell and the circuit prevents reverse current but adds extra diode losses during charging. Even with this extra diode, charging the supercapacitor up to voltages higher than the maximum power point voltage remains impossible without giving up proper MPP tracking operation. The only solution for this problem appears to be a newly conceived circuit based on a different architecture. Slight modifications of a boost converter architecture seem the best candidates for a first tryout.

This chapter explained most of the operational aspects of the Bologna scavenger. The next chapter will compare the scavenger with two simple direct connection implementations. The focus of the chapter will be on energy efficiency.

Chapter 5

Energy efficiency performance of Bologna scavenger

5.1 Introduction

This chapter will investigate the energy efficiency performance of the Bologna scavenger. First however, two simple direct connection implementations will be tested on their efficiency. These results will enable us to determine how useful the MPP tracking really is for the lab conditions under which the scavenger was tested. The MPP tracking reduces the losses in the solar cell but creates additional losses in between the cell and the DC/DC converter. Which effect takes the upper hand will be discussed in this chapter. We will also have a look at the performance of the supercapacitor when used in an energy scavenger. As in Chapter 3, the supercapacitor will be discussed based on cycle efficiencies and the validity of the energy content formula.

5.2 Test setup

5.2.1 Tested circuits

We already mentioned in the introduction that besides the Bologna scavenger, two simple direct connection implementations were tested. Figure 5.1 shows the first circuit and the according test setup. Thick arrows indicate the measured currents while the thin arrows represent the measured voltages. The same DMM as in Section 4.3.1 was used. This time, all current measurements were executed via external shunts of $0.5\ \Omega$. This choice was inspired by the conclusion that current measurements through the internal shunt of the DMM gave inconsistent results. This will be demonstrated in Section 5.4.1.

The circuit of Figure 5.1 is certainly not advanced. The BTnode and the supercapacitor are directly connected to the solar cell. The voltage and the current of the solar cell are consequently completely determined by the supercapacitor voltage. Because the circuit lacks a DC/DC converter, the DC/DC

converter of the BTnode was used (LTC3429). We could have opted for an external DC/DC converter identical to the converter implemented in the Bologna scavenger. In practice however, a simple direct connection like depicted in Figure 5.1 will never use an external DC/DC converter when the sensor node has one onboard. This way, an additional printed circuit board can be avoided. The LTC3429 operates in a very similar manner as the LTC3401 (DC/DC converter of the Bologna scavenger). The burst mode of the devices are however conceived in a slightly different way, leading to different efficiency curves. In every experiment discussed in this chapter, the BTnode - excluding its onboard DC/DC converter - draws the same constant power and current (see next section for more information about the test procedure). For this constant output current, the onboard DC/DC converter and the external LTC3401 achieve very similar efficiencies according to their datasheets [32, 31]. Nonetheless, the difference in used DC/DC converter will be taken into account during the comparison of the tested circuits.

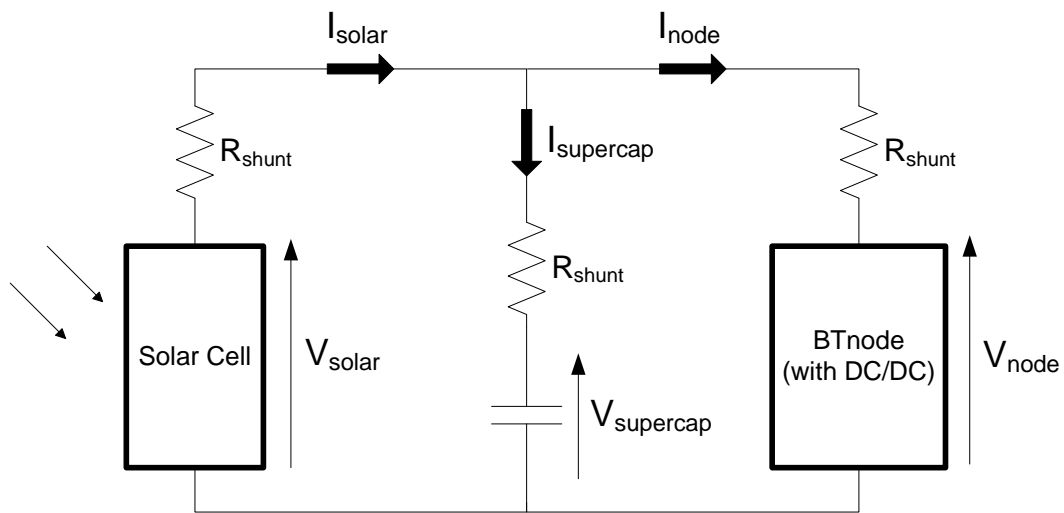


Figure 5.1: Direct connection test setup.

The second direct connection implementation is depicted in Figure 5.2. The only added feature in comparison with the previous circuit is the diode that is placed just after the solar cell. This diode will prevent a discharge of the supercapacitor via a reverse solar cell current for situations during which $V_{supercap}$ is larger than the open-circuit voltage of the solar cell. The diode however also introduces additional losses when the solar cell supplies energy to the supercapacitor and BTnode. The comparison between the two direct connection implementations will demonstrate if the extra diode can be considered as an improvement or a disadvantage, at least for the used test setup and procedure.

For the test setup of the Bologna scavenger we refer to Section 4.3.1 and Figure 4.15. We also implemented our own Bologna circuit on a prototype board. All components were kept identical in comparison to the PCB implementation of the circuit. We however added extra pins and jumpers to allow an easy measurement of internal voltages and currents. This way we were able to measure

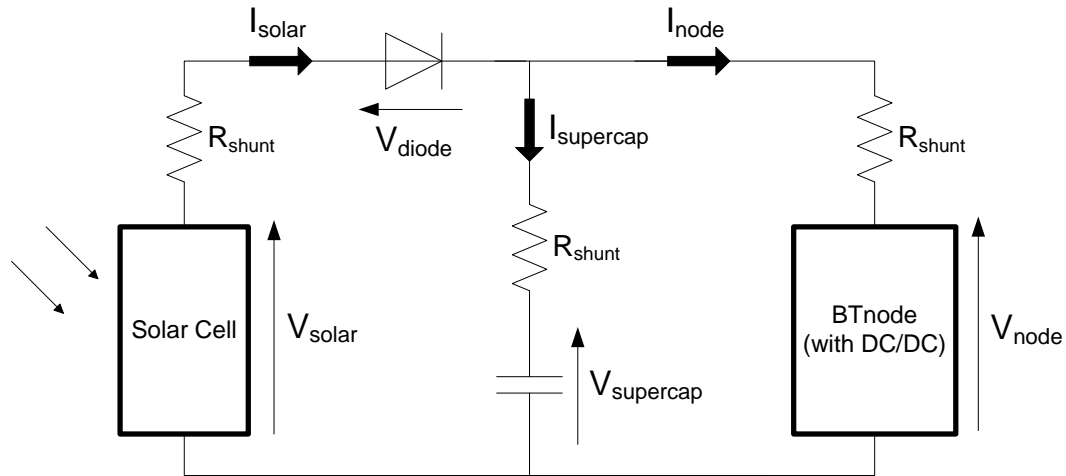


Figure 5.2: Direct connection test setup.

the power consumed by the comparator and measure the current entering the DC/DC converter. To measure a current, the jumper had to be replaced by a modest two-pin connector that was directly connected to a $0.5\ \Omega$ shunt resistor. In Chapter 4 we discussed the investigation of the influence of circuit component values as possible future work. This prototype board will enable easy replacement of components, even when the replacement has a different footprint. This can be very convenient when testing e.g. high inductance and capacitance components since the available footprint of those components can vary greatly. Both the PCB and the prototype board implementation of the Bologna scavenger were tested and analysed.

5.2.2 Test procedure

The test procedure used in this chapter is a combination of the procedures used in Chapters 3 and 4 and is identical for the different circuits. Before starting an experiment, the supercapacitor is pre-charged to 2 V for about an hour. This ensures that the state of the supercapacitor at the beginning of each experiment is to a very large extent the same. The operating system of the BTnode is active during the whole course of the experiment and does not execute any additional tasks. This keeps the current drawn by the BTnode (excluding the onboard DC/DC converter) very stable and constant. The solar cell is illuminated by a desk lamp with a distance of 12 cm between lamp and solar cell. For this test setup, the maximum light intensity of the lamp enables the solar cell to produce about 50 mW more than is consumed by the BTnode. Consequently, the supercapacitor will be charged when the desk lamp operates at its maximum light intensity.

At the start of the experiment, the desk lamp is fully switched on, leading to the charging of the supercapacitor. The moment the supercapacitor reaches its maximum allowed voltage, 2.5 V, the lamp is completely switched off. In this situation, the supercapacitor is discharged to enable continued operation of the BTnode. The discharging is stopped the moment $V_{supercap}$ falls below the experiment-

specific lower boundary voltage. The lamp is turned on again, operating at its maximum light intensity and causing the supercapacitor to be charged. At this point, a sequence of identical charge/discharge cycles begins, with $V_{supercap}$ cycling between the experiment-specific lower boundary and 2.5 V. During charging the desk lamp's intensity is kept constant at its maximum while during discharging the lamp stays completely turned off. In this chapter, two lower boundaries will be used: 1.3 V and 2 V. The same boundaries were adopted in Chapter 3, allowing an easy comparison of the different chapters' results. The lowest boundary of 250 mV used in Chapter 3 was not employed in this chapter for the simple reason that the DC/DC converter stops functioning below 1.3 V. Every experiment was stopped after three cycles, since Section 3.3.4 proved this to be enough for the supercapacitor to reach its cycle-specific steady state.

The maximum power point of a solar cell is very sensitive to its temperature (see Section 4.3.3). During an experiment, the temperature of the solar cell will vary greatly because periods of heating (lamp on) are followed by periods of cooling (lamp off). In order to start each experiment with a comparable solar cell performance, the solar cell was illuminated by the desk lamp at its maximum light intensity for about 40 minutes. Section 4.3.3 demonstrated how, for the same test setup, the VI curve of a solar cell stabilizes after 36 minutes of being illuminated. Therefore, one can assume that the solar cell has reached this stable state after 40 minutes. During the experiment, the change of the solar cell's temperature and consequently of its MPP will depend on the used lower boundary voltage and the speed of charging and discharging. These last two characteristics are different for every individual circuit.

5.2.3 Accuracy of calculations

In Chapter 4, the measurement results related to the Bologna scavenger were used to visualize the operational behaviour of the circuit. In this chapter however, the results will be used to calculate powers, energies and energy efficiencies. We already mentioned in Section 4.3.1 how the measurement results of the DMM (Agilent 34980A Multifunction Switch/Measure Unit with 34921A 40-Channel Armature Multiplexer) are obtained through an integration or averaging process that results in the average of a signal over an integration time of 20 ms. It is important to understand what the obtained results really represent when they are used in calculations and this section will focus on that.

The 34921A multiplexer contains an integrating multi-slope analog-to-digital converter. This converter performs the averaging process that gives a result following Formula 5.1. The symbol $V_{channel}$ represents the signal that is being sampled/integrated while t_{int} denotes the integration time.

$$V_{result} = \frac{\int_0^{t_{int}} V_{channel}(t) dt}{t_{int}} \quad (5.1)$$

The result can be considered as a weighted average over the integration time, with the voltage of each elementary time interval weighted equally. The results of current measurements follow the same

formula with the addition of a constant factor, the multiplicative inverse of the shunt resistance.

For each sampling period t_{sample} (one second for all experiments), the results will be used to calculate the total energy that has passed through a certain point in the circuit during the whole sampling period. Since the sampling period equals one second, the total energy equals the average power during this sampling period. This average power can be theoretically described as in Formula 5.2.

$$P_{average} = \frac{\int_0^{t_{sample}} V_{channel}(t) \cdot I_{channel}(t) dt}{t_{sample}} \quad (5.2)$$

The obvious method for the calculation of the average power during one sampling period would be the multiplication of the concerned voltage and current results. The result of this multiplication is then given by Formula 5.3.

$$P_{result} = \frac{\int_0^{t_{int}} V_{channel}(t) dt \cdot \int_0^{t_{int}} I_{channel}(t) dt}{t_{int}^2} \quad (5.3)$$

It is clear that some assumptions need to be true before $P_{average}$ can be estimated by P_{result} . In case both $V_{channel}$ and $I_{channel}$ change substantially during the sampling period, Formula 5.3 cannot be used as an estimation of $P_{average}$, since in general the integral of a product of two functions is not equal to the product of the individual integrals of those two functions. If one assumes that e.g. $V_{channel}$ stays constant during the whole integration period, Formula 5.3 becomes however very similar to Formula 5.2.

$$P_{average} = \frac{\int_0^{t_{int}} V_{channel}(t) \cdot I_{channel}(t) dt}{t_{int}} \quad (5.4)$$

Assume now that the changing signal, in this case $I_{channel}$, has a periodic behaviour with a period that is much smaller than the integration time. In this case, Formula 5.4 can be considered as an accurate estimation of the average power during one period of the signal $I_{channel}$. If one assumes that the periodic behaviour of this signal does not change during the whole sampling period, there are no obstructions left to state that $P_{average}$ can be estimated by the formula of P_{result} .

The tested circuits and their measured signals all show the characteristics that are needed to allow a power estimation through Formula 5.3. For the direct connection implementations, V_{solar} and I_{solar} can be considered constant during the sampling period as they follow the slowly changing $V_{supercap}$. The current going from the supercapacitor to the onboard DC/DC converter shows a periodic repetition of a sequence of steep spikes. The voltage over the supercapacitor remains however practically constant during a sampling period, allowing the estimation formula to be used for the power going into the supercapacitor and the power entering the DC/DC converters. The same reasoning can be done for those powers in the Bologna circuit. The power leaving the DC/DC converter can also be estimated by the proposed method, since its output voltage is kept constant. Our own implementation of the

Bologna scavenger enabled the measurement of the power consumed by the comparator. Its supply voltage is also constant when provided by the DC/DC converter making the estimation formula valid for the power consumed by the comparator. The voltage over and the current delivered by the solar cell during MPP tracking meet the requirements the least. The voltage is however confined to a small voltage band for which the decline of the current for an increasing voltage (according to VI curve) is still limited. This should make the estimations of the solar cell power during MPP tracking acceptable.

The problem of finding a suitable measurement method stems from the fact that the tested circuits experience high frequency behaviour that needs to be tracked over a period of several hours. An oscilloscope with enough channels could be used to sample the fast changing signals at a frequency that is more than enough (more than double of highest frequency: Nyquist criterion) to obtain a very accurate estimation of the power. An oscilloscope is however not suited for long uninterrupted measurements. The average power over a small period in time (not more than a couple of milliseconds for frequencies up to 1 MHz) can be accurately calculated based on oscilloscope measurements. The total delivered energy during a duration of minutes or even hours is however out of its scope. The DMM that was used for our measurements has a minimum integration time of $300\ \mu\text{s}$, which is still substantially larger than the period of a 1 MHz signal ($1\ \mu\text{s}$). If more accurate measurements are wanted, other solutions will have to be sought.

5.3 Efficiency definitions

In Chapter 3 we already introduced the cycle efficiency as a measure of the efficiency of a supercapacitor. This section presents two other efficiency definitions that will allow us to analyse the different tested circuits.

5.3.1 Short-term or instant efficiency

The short-term efficiency of an energy scavenger is calculated for every sampling period of the measurement duration. It basically compares the difference between the energy delivered to and by the circuit with the energy delivered to the storage device, in our case a supercapacitor. The principle is demonstrated in Figure 5.3. The energy delivered by the solar cell to the scavenger system during the sampling period at time t is denoted by $E_{solar}(t)$. Energies $E_{node}(t)$ and $E_{supercap}(t)$ represent the total energy respectively delivered to the sensor node and the supercapacitor during the same sampling period. The short-term efficiency $\eta_{short}(t)$ is then defined as in Formulas 5.5 and 5.6.

$$\text{if } E_{solar}(t) > E_{node}(t) \text{ then } \eta_{short}(t) = \frac{E_{supercap}(t)}{(E_{solar}(t) - E_{node}(t))} \quad (5.5)$$

$$\text{else } \eta_{short}(t) = -\frac{(E_{solar}(t) - E_{node}(t))}{E_{supercap}(t)} \quad (5.6)$$

In case the scavenger would have zero losses, the short-term efficiency would be 100%. All energy delivered to the system and not delivered to the sensor node would be stored in the supercapacitor.

The definition of $\eta_{short}(t)$ depends on the sign of the net energy provided to the system. If more energy is provided than consumed, the unused energy can be stored in the supercapacitor. There are however losses in the circuit that will lead to a value of $\eta_{short}(t)$ lower than 1, according to Formula 5.5. In case more energy is consumed by the node than provided by the solar cell, the supercapacitor is discharged to compensate the difference. In this situation the circuit also introduces losses, which means that $E_{supercap}(t)$ will need to be higher than the difference between provided and consumed energy. Therefore, $\eta_{short}(t)$ will have again a value between 0 and 1, now according to Formula 5.6.

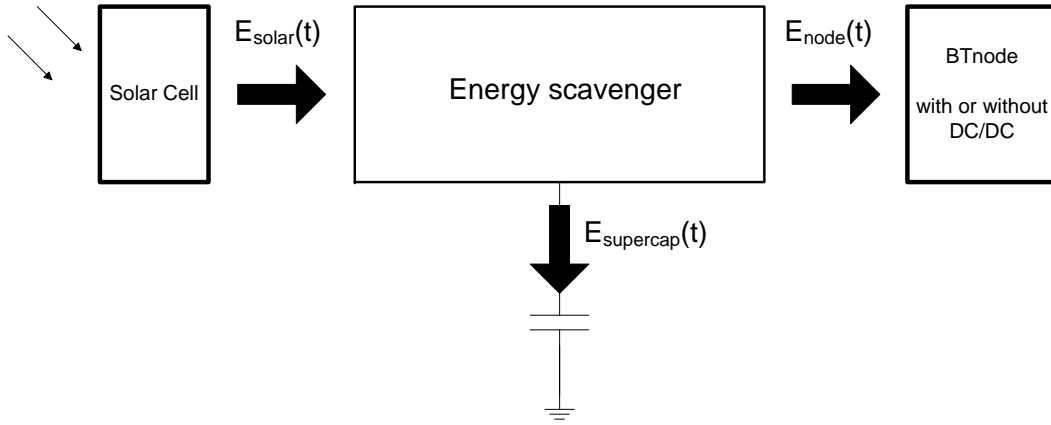


Figure 5.3: Short-term efficiency principle.

5.3.2 Long-term or round-trip efficiency

The short-term efficiency allows to investigate how the efficiency of the scavenger evolves during an experiment. It is however less suited for an overall comparison of different circuits. Therefore we came up with our own definition of a long-term efficiency that would enable us to easily compare totally different energy scavenging systems. The definition of this long-term or round-trip efficiency η_{long} is given by Formula 5.7.

$$\eta_{long} = \frac{P_{node}}{\left(\frac{t_{charge}}{t_{charge} + t_{discharge}} \right) P_{max}} \quad (5.7)$$

The power P_{node} is the power drawn by the BTnode over the course of the experiment. We already mentioned in previous sections that this power is practically stable and constant. The time t_{charge} denotes the duration of the charging for one charge/discharge cycle. The time $t_{discharge}$ represents the time during which the supercapacitor is discharged and the lamp is turned off, again during one cycle. The total duration of a charge/discharge cycle can then be calculated as $t_{charge} + t_{discharge}$. The power P_{max} equals the maximum power the solar cell can deliver for the used test setup. It is used as reference power and it enables to take into account the mismatch between the MPP and the actual

operating point of the solar cell. Since the MPP is influenced by the solar cell's temperature (the higher the temperature, the lower the maximum power), the maximum power provided by the solar cell when the solar cell is at room temperature (lowest achievable temperature during experiment) is used as P_{max} . Consequently, when the actual P_{solar} is lower than P_{max} this can be caused by a mismatch between the MPP and the actual operating point, but also by the effect of the heat generated by the desk lamp.

The total energy consumed by the BTnode during one cycle can be calculated as P_{node} multiplied with $(t_{charge} + t_{discharge})$. The total energy that could have been provided by the solar cell during one cycle - assuming no MPP mismatch and no temperature effects - equals $(t_{charge} \cdot P_{max})$. The ratio of the total output energy and the maximum achievable input energy for one cycle is then given by Formula 5.7 and represents the long-term efficiency.

It is important to note that this long-term efficiency definition is based on assumptions typical for the used test setup and procedure. Since P_{max} and P_{node} will have the same value for the different tested circuits, the long-term efficiency is completely determined by the ratio $\left(\frac{t_{charge}}{t_{charge} + t_{discharge}}\right)$. The long-term efficiency indicates how efficiently the available solar power is used to provide a constant output power.

5.4 Measurement results

The results obtained for the tested circuits will be discussed in this section. First, every circuit will be investigated in an own dedicated section. Those individual sections will take a look at where the losses for a specific circuit can be found and how those losses evolve during the experiment, dependent on supercapacitor voltage, solar cell temperature, solar cell power, etc. Finally, Section 5.5 will compare the different circuits through the help of suitable criteria.

5.4.1 Direct connection

We already mentioned in the description of the test setup that 0.5Ω shunt resistors were used for the current measurements. In Chapter 3 however, the current measurements were performed by the internal shunt of the DMM and also the first experiment of this chapter was done in this way. The results of this first experiment showed however serious inconsistencies indicating a non-negligible influence of the measurements on the behaviour of the circuit. In contrast to the supercapacitor experiments of Chapter 3, some of the measured currents in this chapter possess high frequency components. There is only one internal shunt in the DMM present and therefore an individual current only passes through the shunt during the actual measurement. After a measurement, another to be measured current is lead through the shunt while the first one is short-circuited. This is done by a switching process that is executed in such a way that the current always has a path to go through. Apparently however,

this frequent change of current path influences the high-frequency behaviour of the circuit. This is demonstrated by Figure 5.4, showing a 1.3 V to 2.5 V charge/discharge cycle of the direct connection.

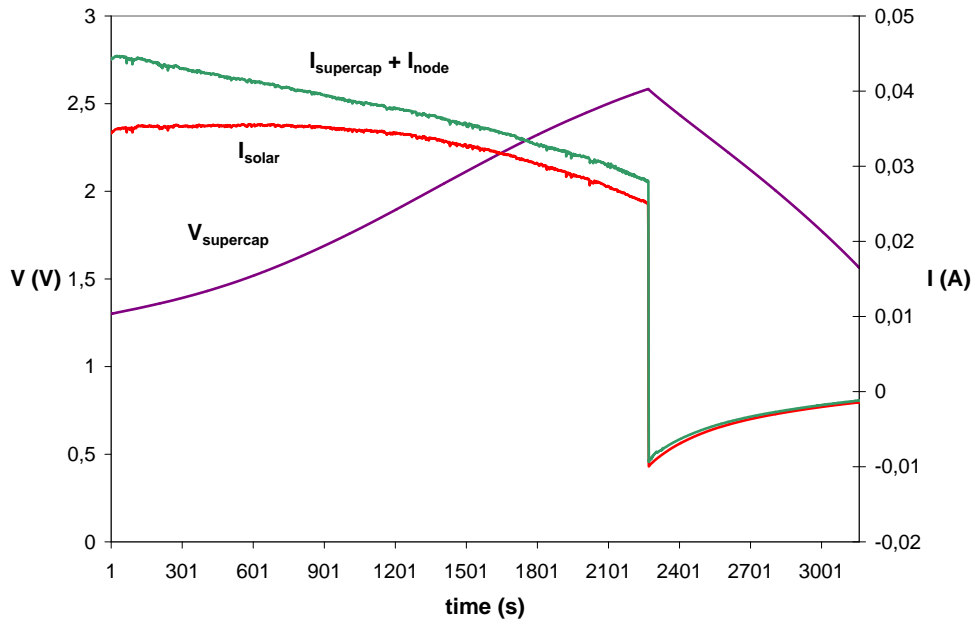


Figure 5.4: Influence of switching in DMM on measurement results.

In a direct connection, the current provided by the solar cell flows to the supercapacitor or to the DC/DC converter. As a consequence, the sum of those last two currents has to be equal to the current coming from the solar cell (Kirchhoff's Current Law). The results shown in Figure 5.4 seem to claim otherwise. Especially during charging, when the solar cell produces power, $(I_{supercap} + I_{node})$ and I_{solar} differ substantially. The results obtained through the DMM are averages but nonetheless $(I_{supercap} + I_{node})$ and I_{solar} should be equal during normal circuit behaviour. To remove the effect of the internal switching of the DMM, we opted for external shunts and placed one shunt in each circuit path of which the current had to be measured. This way, a permanent and unvarying path for each current was assured. The results for the same experiment but obtained through external shunts are depicted in Figure 5.5. The curves of $(I_{supercap} + I_{node})$ and I_{solar} are completely similar now, indicating that the influence problem has been resolved. The external shunts were used for all experiments discussed in this chapter.

Figure 5.6 contains the complete 1.3 V to 2.5 V charge/discharge cycle experiment for the direct connection. The power consumed by the node, which in this case includes the onboard DC/DC converter, is denoted as P_{node} . The fact that P_{node} doesn't stay constant over the course of the experiment, despite no changes in the tasks executed by the BTnode, is solely caused by the input voltage dependency of the DC/DC converter. During charging the current going to the supercapacitor increases as the DC/DC converter needs less power and consequently draws less current to maintain the converting process.

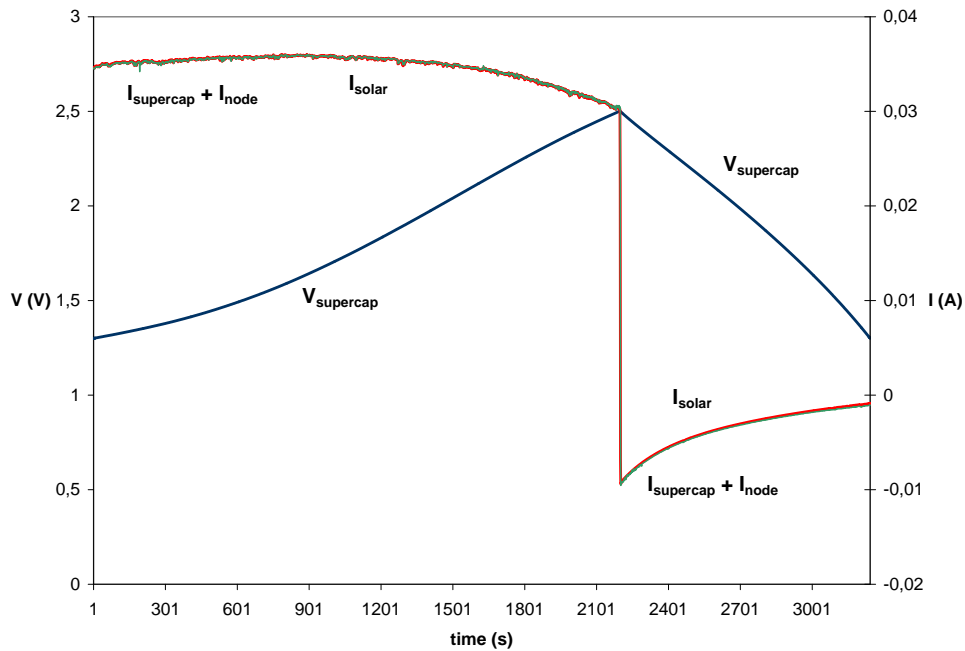


Figure 5.5: Direct connection: current measurements with external shunts.

At the end of charging this increase becomes a decrease. The solar cell is at this point close to or past its MPP and for this voltage range the VI curve shows a steep decline for an increasing voltage. The moment the discharging starts, $I_{supercap}$ becomes negative. The negative current experiences first a decline - in absolute value - as the reverse current through the solar cell decreases for a decreasing solar cell voltage (and besides the very small voltage drops over the shunts, $V_{solar} = V_{supercap}$). At a certain point however, the effect of the higher demand for current by the DC/DC converter starts to dominate, leading to an increase of $|I_{supercap}|$.

For a direct connection, the solar cell is not working in its MPP for the majority of time, as is demonstrated in Figure 5.7. Only right before the end of discharging the solar cell operates in what seems to be its MPP. The $V_{solar} - P_{solar}$ combinations depicted in Figure 5.7 also demonstrate the influence of temperature. In contrast to all other experiments in this chapter, the solar cell for this experiment was not 'pre-heated' at the start of the experiment. The first time 2.5 V is reached, the solar cell has consequently a lower temperature and a higher maximum output power than at the end of charging during the 1.3 V to 2.5 V cycles. During those cycles, charging and the resulting heating last longer, reducing the performance of the solar cell.

The cycle efficiencies for the direct connection experiments are presented in Table 5.1. Those cycle efficiencies ($\eta_{cycle,circuit}$) are calculated in a very similar manner as the supercapacitor cycle efficiencies discussed in Chapter 3 (see Formula 5.8). The energy E_{in} is in this case however the total energy provided by the solar cell during the charging phase of one cycle. The energy E_{out} on the other hand

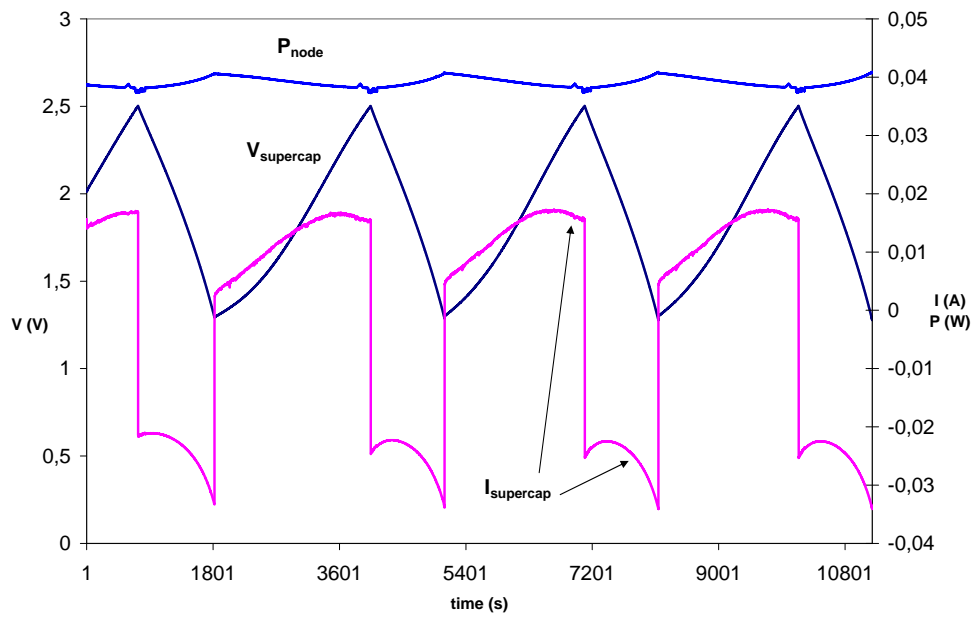


Figure 5.6: Direct connection: 1.3 V to 2.5 V charge/discharge cycle.

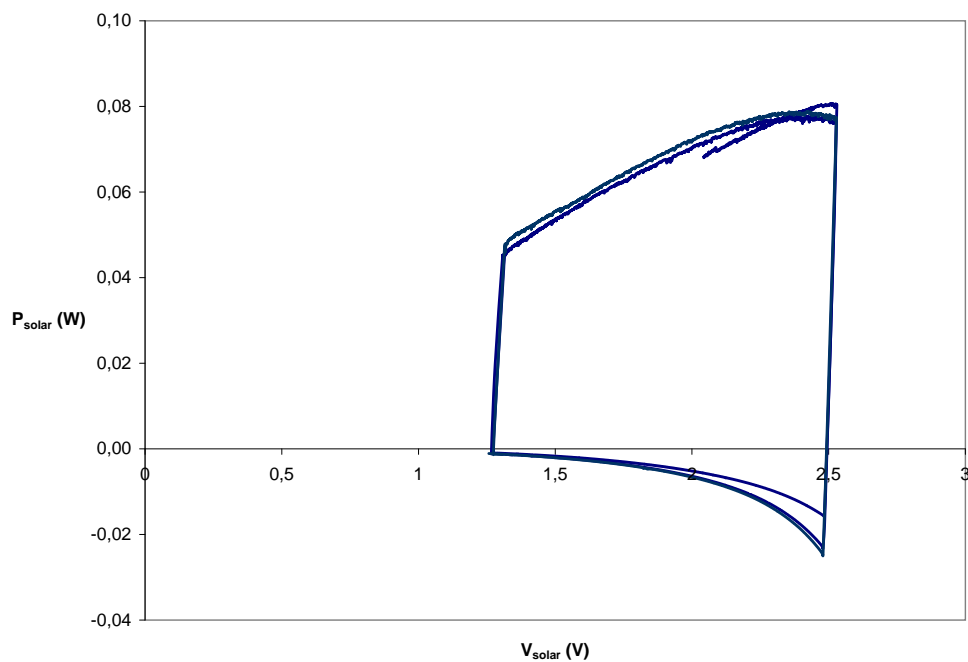


Figure 5.7: Direct connection: P_{solar} versus V_{solar} (1.3 V to 2.5 V cycle).

denotes the total energy consumed by the BTnode (with or without DC/DC converter, depending on the circuit-specific test setup) during the whole duration of one cycle. For each experiment, the cycle efficiencies in Table 5.1 belong to the last cycle of the three cycle sequence. This gives enough time to the circuit to get rid of most of the transitional effects, like e.g. the effect of the pre-charging of the

supercapacitor. This choice was repeated for the other experiments discussed in this chapter.

$$\eta_{cycle} = \frac{E_{out}}{E_{in}} \times 100 \quad (5.8)$$

		Charge/discharge interval	
		1.3 V to 2.5 V	2 V to 2.5 V
$\eta_{cycle,circuit}$ reference	1.3 V	90.29%	
	2 V	81.26%	86.42%

Table 5.1: Direct connection: cycle efficiency ($\eta_{cycle,circuit}$).

The only losses that can occur in the direct connection circuit are supercapacitor losses and the loss of energy due to reverse current through the solar cell during the discharge phase (the DC/DC converter is not considered as a part of the circuit). Table 5.2 shows the cycle efficiencies for the supercapacitor ($\eta_{cycle,cap}$), defined and calculated in the exact same way as in Chapter 3 (Section 3.3.4). The difference between the two tables indicates the extent of the losses caused by reverse solar cell current.

		Charge/discharge interval	
		1.3 V to 2.5 V	2 V to 2.5 V
$\eta_{cycle,cap}$ reference	1.3 V	97.95%	
	2 V	87.27%	97.89%

Table 5.2: Direct connection: cycle efficiency of supercapacitor ($\eta_{cycle,cap}$).

Figures 5.8 and 5.9 contain the E_{form} and E_{adj} curves for the supercapacitor. The energies E_{form} and E_{adj} have the same definition as their counterparts in Chapter 3 (Section 3.3.4). The figures show very similar behaviour compared to the results obtained in Section 3.3.4 for the multiple cycle supercapacitor experiments.

Section 5.5 contains a comparative analysis of the different tested circuits. The long-term efficiency of each circuit will be covered there. The short-term efficiency gives insight in how the instant efficiency of a specific circuit (excluding the supercapacitor) changes for various $V_{supercap}$, V_{solar} , etc. Therefore, the short-term efficiency of a circuit will be discussed in the section dedicated to that circuit. Since the direct connection possesses no energy-consuming components, $(P_{solar} - P_{node})$ and $P_{supercap}$ are equal at each moment in time (see Figure 5.10), making the short-term efficiency for this circuit not very informative. This will be different for the more complex circuits.

5.4.2 Direct connection with diode

Figure 5.11 displays the 1.3 V to 2.5 V cycle experiment for the direct connection with diode. The biggest difference with the previous section is the absence of negative solar cell current during dis-

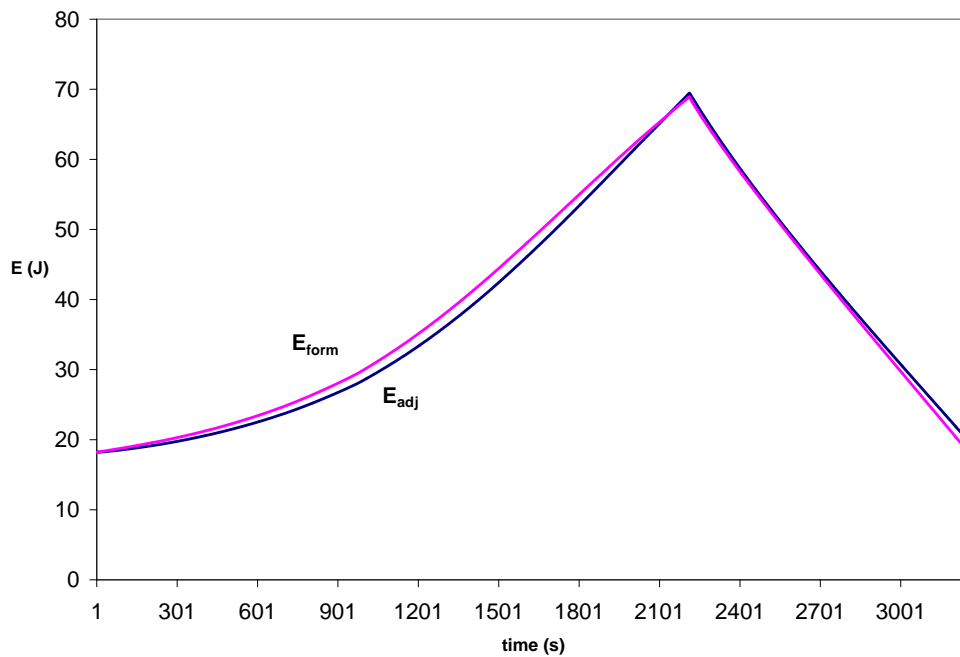


Figure 5.8: Direct connection: supercapacitor's energy content (1.3 V to 2.5 V cycle).

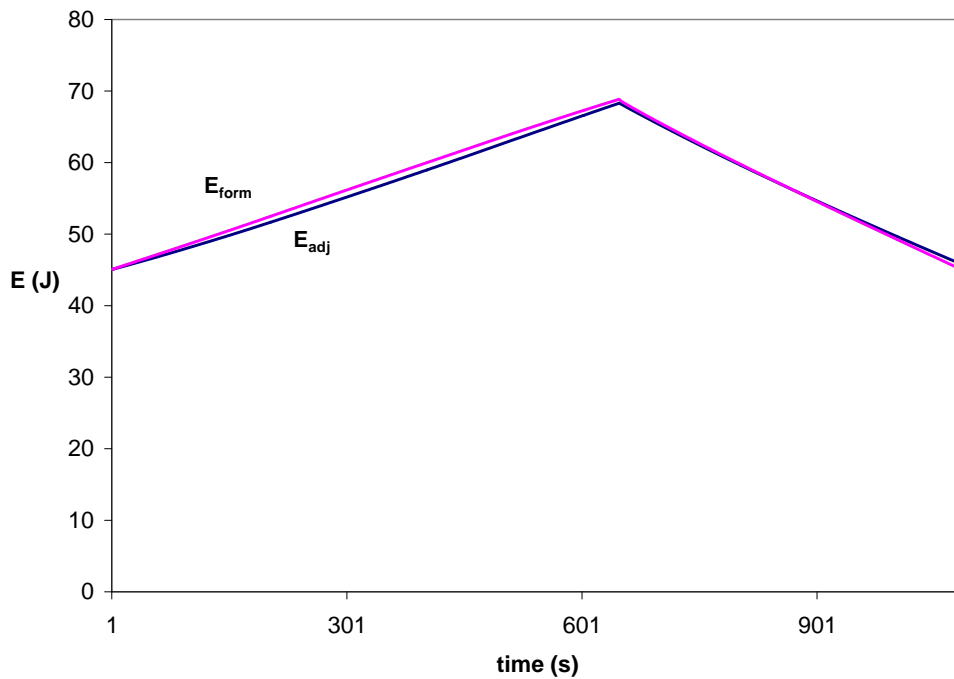


Figure 5.9: Direct connection: supercapacitor's energy content (2 V to 2.5 V cycle).

charging. The diode is responsible for a positive shift of the solar cell voltage of 250 mV. Figure 5.12 shows how this influences the solar cell power during the course of the experiment (compare with Figure 5.7 for the direct connection). For this experiment, the solar cell was 'pre-heated' and this for

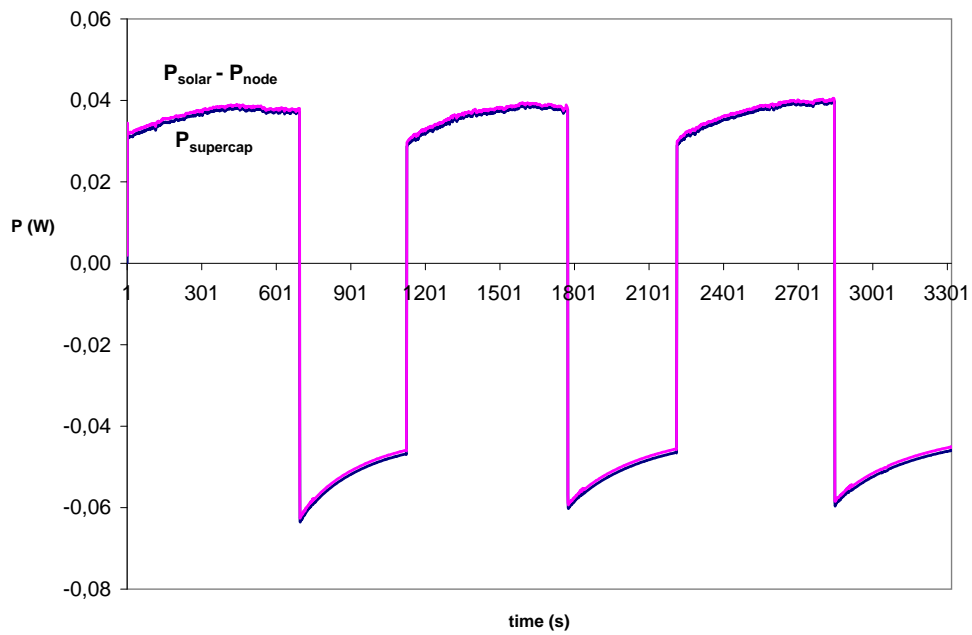


Figure 5.10: Direct connection: short-term efficiency (2 V to 2.5 V cycle).

a longer time than the charging time of a cycle. Consequently, the solar cell's temperature was higher at the beginning of the experiment than during any other moment. This explains the lower power provided during the first charging phase from 2 V to 2.5 V.

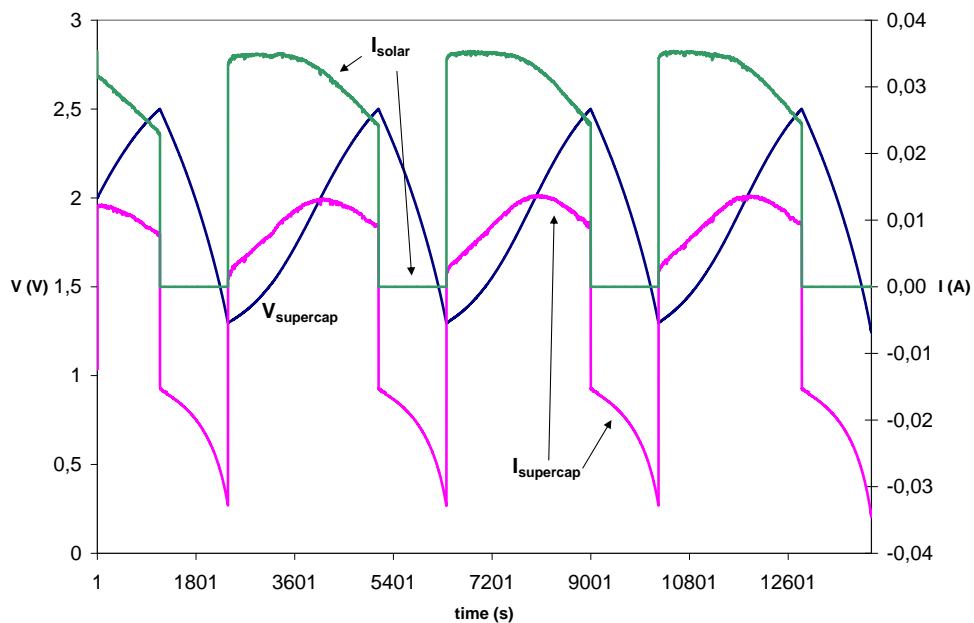


Figure 5.11: Direct connection with diode: 1.3 V to 2.5 V charge/discharge cycle.

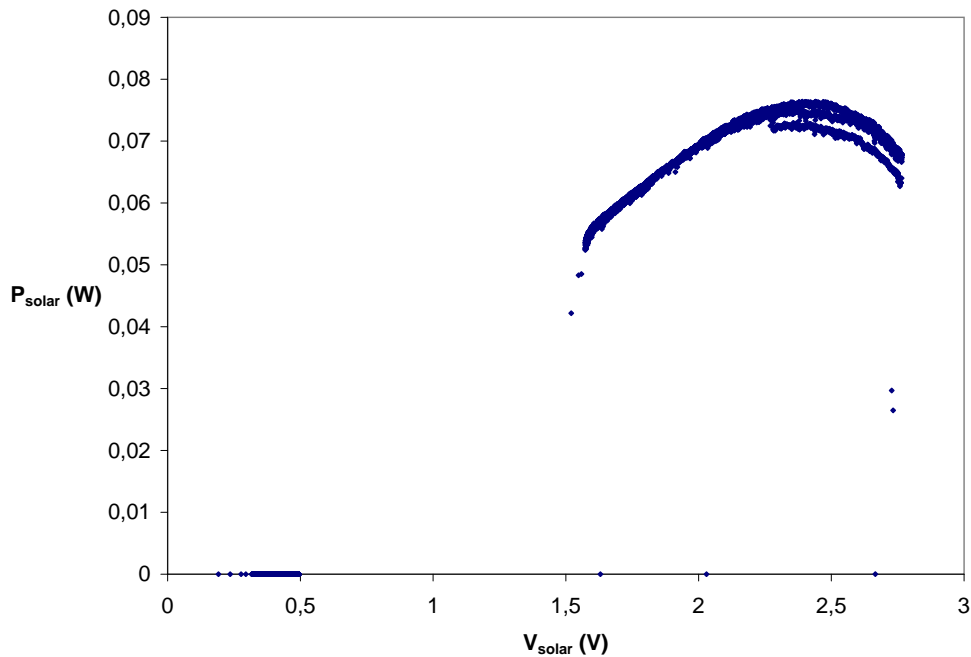


Figure 5.12: Direct connection with diode: P_{solar} versus V_{solar} (1.3 V to 2.5 V cycle).

Table 5.3 contains the cycle efficiencies for the direct connection with diode. Compared to the direct connection (Table 5.1), the cycle efficiency for the 1.3 V to 2.5 V charge/discharge cycle is lower while the cycle efficiencies for a reference of 2 V are higher. This makes sense since the advantage of the diode is the highest for high solar cell voltages. In this range, the losses of the diode are lower (since the solar cell current is lower) and the reverse current during discharging is higher, making the presence of the diode more advantageous.

		Charge/discharge interval	
		1.3 V to 2.5 V	2 V to 2.5 V
$\eta_{cycle,circuit}$ reference	1.3 V	84.89%	
	2 V	85.31%	87.53%

Table 5.3: Direct connection with diode: cycle efficiency ($\eta_{cycle,circuit}$).

Table 5.4 contains the supercapacitor cycle efficiencies. For a 1.3 V to 2.5 V charge/discharge cycle, the supercapacitor cycle efficiency is higher for the lower cycle reference. The presence of the diode has turned this higher supercapacitor cycle efficiency in a lower cycle efficiency for the circuit as a whole.

		Charge/discharge interval	
		1.3 V to 2.5 V	2 V to 2.5 V
$\eta_{cycle,cap}$ reference	1.3 V	96.80%	
	2 V	90.95%	97.23%

Table 5.4: Direct connection with diode: cycle efficiency of supercapacitor ($\eta_{cycle,cap}$).

Figure 5.13 depicts the short-term efficiency of the direct connection together with its power components (for the 1.3 V to 2.5 V cycle experiment). The efficiency during charging improves for an increasing supercapacitor voltage. As could be seen in Figure 5.11, the solar cell current decreases during charging. The diode is the only energy-consuming component in the observed circuit and has a constant voltage drop. As a consequence, the consumed power by the diode decreases, increasing the short-term efficiency. During discharging, η_{short} stays very close to 100%. This is no surprise since the current from the supercapacitor runs directly to the BTnode. Nonetheless, one can notice a slight decrease of the short-term efficiency for an decreasing supercapacitor voltage. This is more than likely caused by the shunts that were used to measure the currents. The lower $V_{supercap}$ gets, the higher the current drawn by the onboard DC/DC converter of the BTnode. This higher current leads to higher losses in the shunts.

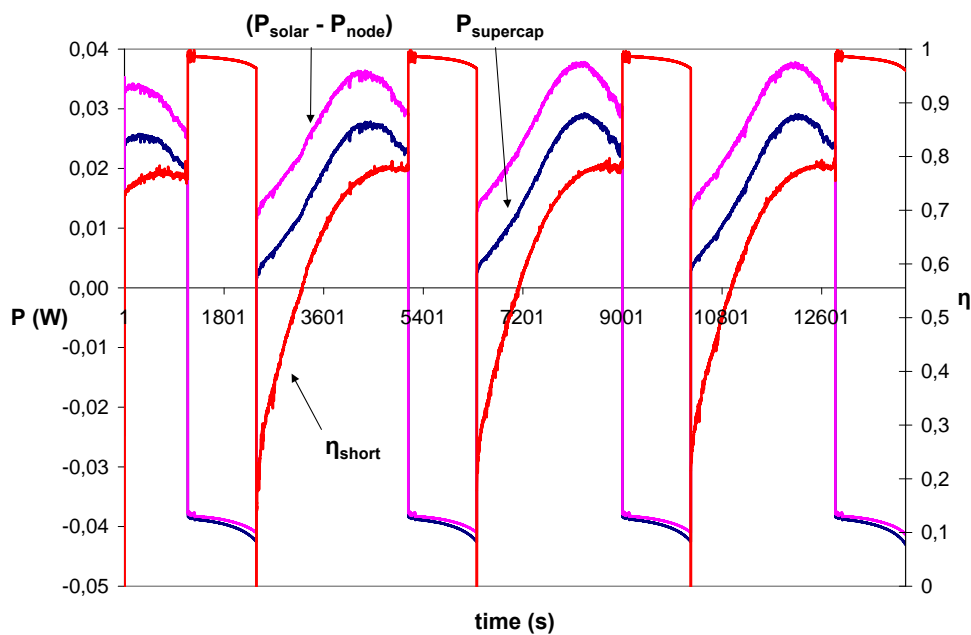


Figure 5.13: Direct connection with diode: short-term efficiency (1.3 V to 2.5 V cycle).

The losses taking place in the circuit for the 1.3 V to 2.5 V cycle experiment are visualized in Figure 5.14. The definition of the energy $E_{circuit}$ is very similar to the definition of the energy E that was used in Chapter 3 to represent the energy content of a supercapacitor, based on the entering and outgoing

energy. As Formula 5.9 shows, $E_{circuit}$ is adjusted based on the entering and outgoing energy with regard to the complete circuit. It represents the energy content of the whole circuit, assuming no circuit losses occur.

$$E_{circuit}(n+1) = E_{circuit}(n) + (P_{solar}(n+1) - P_{node}(n+1)) \cdot 1s \quad (5.9)$$

The energy $E_{circuit,adj}$ is the adjusted version of $E_{circuit}$ for which the value is reset to the theoretical energy content of the circuit at the end of each cycle. This theoretical energy content is the energy content of the supercapacitor according to the energy content formula. The curve of $E_{circuit,adj}$ allows to easily distinguish the difference between the total energy that has entered the circuit - during one cycle - and the total energy that has left it - during the same cycle. After all, this difference equals the difference between the start and the end value of $E_{circuit,adj}$ with respect to the concerned cycle.

The energy E_{adj} has the same definition as in Chapter 3, representing the energy content of the supercapacitor while assuming no internal losses. At the end of a cycle, E_{adj} is also reset to the theoretical energy content. The cycle efficiencies of the supercapacitor are for this experiment that high (see Table 5.4) that the resetting of E_{adj} at the end of a cycle is barely noticeable.

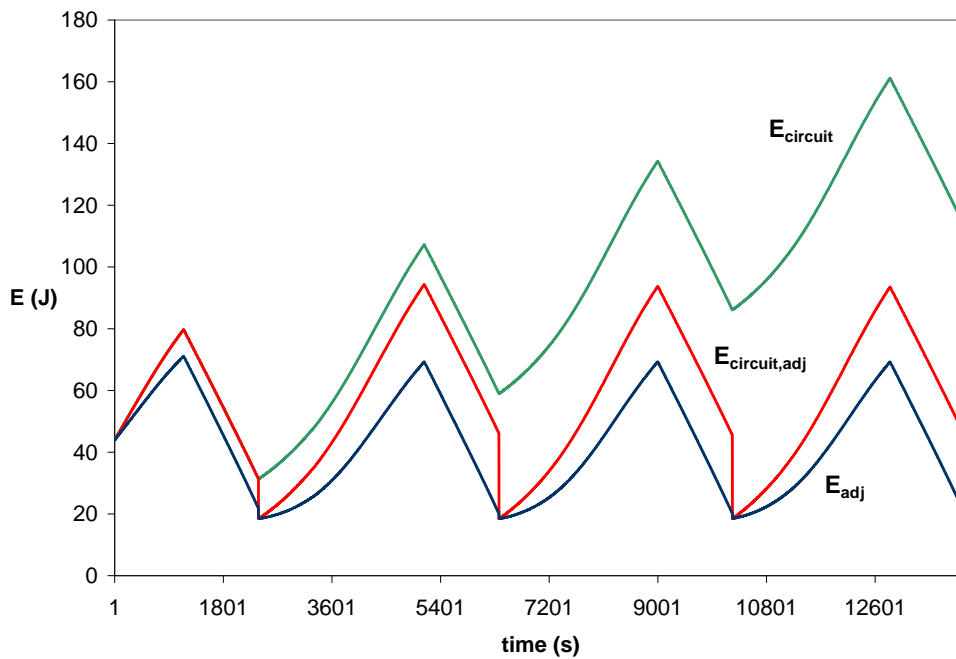


Figure 5.14: Direct connection with diode: energy losses (1.3 V to 2.5 V cycle).

The counterparts of the figures in this section for the 2 V to 2.5 V cycle experiment are not included since they do not provide additional insight in the behaviour of the concerned circuit. For the next two sections, the same decision was taken.

5.4.3 Bologna scavenger

The 1.3 V to 2.5 V cycle experiment of the Bologna scavenger is shown in Figure 5.15. As Chapter 4 already gave a lot of attention to the working principle of the Bologna scavenger, this figure won't be discussed extensively. As for the discharging phase in the direct connection, the negative $I_{supercap}$ decreases in absolute value before starting a steep decline. At first, the effect of the decreasing reverse solar cell current is dominating. At a certain point however, the effect of an increasing current demanded by the onboard DC/DC converter starts to carry more weight, leading to the steep decline. One can also notice a disruption of the first discharging phase. During this disruption, the MPP of the solar cell was measured in order to configure the voltage dividers of the MPP tracker.

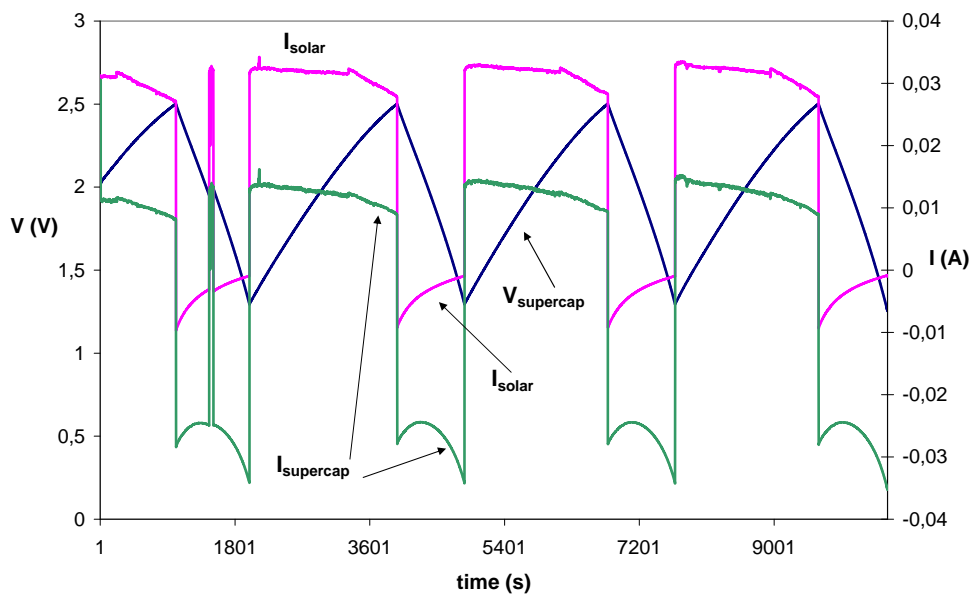


Figure 5.15: Bologna scavenger: 1.3 V to 2.5 V charge/discharge cycle.

The cycle efficiencies for the Bologna scavenger are presented in Table 5.5. Efficiencies of only 60% are achieved. One should keep in mind that for the Bologna scavenger the DC/DC converter is included in the circuit, in contrast to the two previous discussed circuits. When comparing the circuits in Section 5.5, this disparity will certainly be taken into account. Table 5.6 shows the cycle efficiencies for the supercapacitor. The losses in the supercapacitor appear to be very limited for the specific multiple cycle experiments that were performed in this chapter, independent of which circuit was tested.

		Charge/discharge interval	
		1.3 V to 2.5 V	2 V to 2.5 V
$\eta_{cycle,circuit}$ reference	1.3 V	60.80%	
	2 V	59.84%	60.68%

Table 5.5: Bologna scavenger: cycle efficiency ($\eta_{cycle,circuit}$).

		Charge/discharge interval	
		1.3 V to 2.5 V	2 V to 2.5 V
$\eta_{cycle,cap}$ reference	1.3 V	98.00%	
	2 V	93.42%	97.63%

Table 5.6: Bologna scavenger: cycle efficiency of supercapacitor ($\eta_{cycle,cap}$).

We already mentioned that the BTnode consumed a constant power (excluding DC/DC converting) for each experiment. For the previous circuits, the DC/DC converting was done onboard and we actually didn't know this constant power. In the Bologna scavenger test setup, the onboard converter is circumvented and the power entering the node is directly used to power the different sensor node ICs. Figure 5.16 shows the power delivered by the external DC/DC converter of the Bologna scavenger during the 1.3 V to 2.5 V cycle experiment. The power equals 31.6 mW and is indeed constant over the course of the whole experiment. The BTnode was programmed in the exact same way for all experiments. Therefore it is certainly justified to assume that the power that needed to be provided by the onboard DC/DC converter during the direct connection experiments was also equal to 31.6 mW.

The short-term efficiency for the 1.3 V to 2.5 V cycle experiment is depicted in Figure 5.17. As P_{node} is constant, one can observe a slight decline of P_{solar} during the MPP tracking. This decline is caused by the increase of temperature during charging. The efficiency η_{short} increases from below 40% to about 62% during MPP tracking. One could actually expect an improvement of the efficiency of the MPP tracker for an increasing $V_{supercap}$. The duty cycle of the MPP tracker switch changes during charging in such a way that the diode conducts less and less compared to the time during which the switch is closed. With its voltage drop of 250 mV, the diode is by far the most energy-consuming component in the tracker.

The moment the MPP tracking stops, η_{short} starts to decrease until the discharging begins. The last phase of the charging during which the MPP tracker does not function is characterised by an increase of the solar cell voltage and a simultaneous decrease of the solar cell power. The increasing voltage $V_{supercap}$ is also responsible for less demand for power by the DC/DC converter. The decreasing solar cell power seems to be the dominating effect as $P_{supercap}$ decreases faster than P_{solar} with a falling η_{short} as a consequence. The short-term efficiency during discharging lies below 80%. This is due to the losses in the DC/DC converter and the losses caused by the reverse solar cell current.

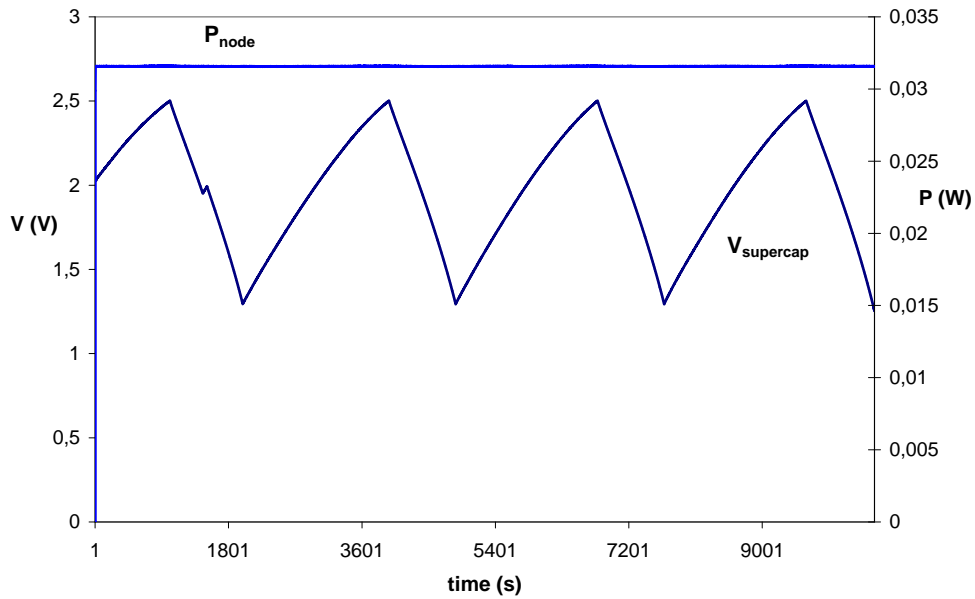


Figure 5.16: Bologna scavenger: P_{node} (1.3 V to 2.5 V cycle).

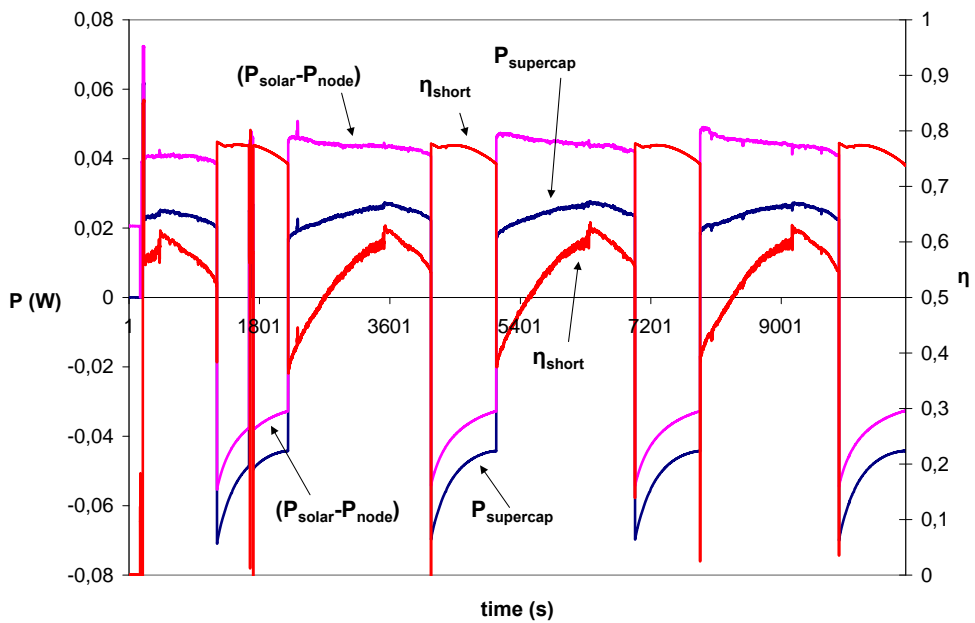


Figure 5.17: Bologna scavenger: short-term efficiency (1.3 V to 2.5 V cycle).

The energy losses in the circuit (including the supercapacitor) are pictured in Figure 5.18. The total energy that is lost during one cycle (= difference between start and end value for concerned cycle) is even higher than the total energy that was inserted in the supercapacitor during this same cycle. The supercapacitor losses are for this experiment negligible as the resetting of E_{adj} is once again barely noticeable.

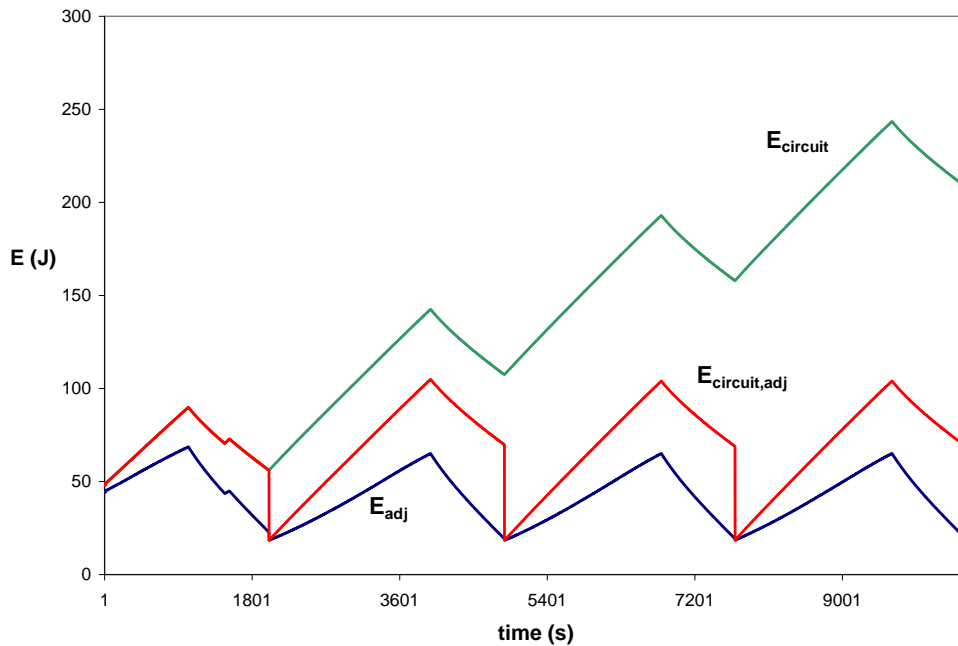


Figure 5.18: Bologna scavenger: energy losses (1.3 V to 2.5 V cycle).

5.4.4 Prototype board implementation of Bologna scavenger

In this section, the prototype that we personally constructed is discussed (picture can be found in Appendix A). The prototype circuit is identical to the circuit of the PCB implementation that was investigated in the previous section. It allowed us however to monitor the power used by the comparator in order to get a better picture of where most power is lost. This prototype board actually also allows to measure the current entering the DC/DC converter. We however noticed a difference in charging rate for the circuit with and without a shunt placed between the supercapacitor and the DC/DC converter. To allow a fair comparison between this section and the previous one, we opted for experiments without the measurement of the current entering the DC/DC converter. Time constraints prevented us of fully repeating all the experiments with the inclusion of a DC/DC converter current measurement. These experiments should be able to provide a more precise idea of where most power is lost.

The power consumed by the comparator is depicted in Figure 5.19. A maximum of $700\ \mu\text{W}$ is used at the beginning of charging, during which the frequency of the MPP tracker is the highest. During charging, the frequency and the average comparator power decrease. Right before the end of discharging, only $150\ \mu\text{W}$ is needed by the comparator. During one cycle, the energy consumed by the comparator represents only 0.38% of the energy that was inserted in the circuit. It is consequently fair to say that the comparator is only responsible for a negligible part of the losses. When the harvester is used in an environment that provides only on rare occasions energy to the system, the quiescent power of $15\ \mu\text{W}$ (drawn by the comparator when no switching is done) can however start to play a

more important role.

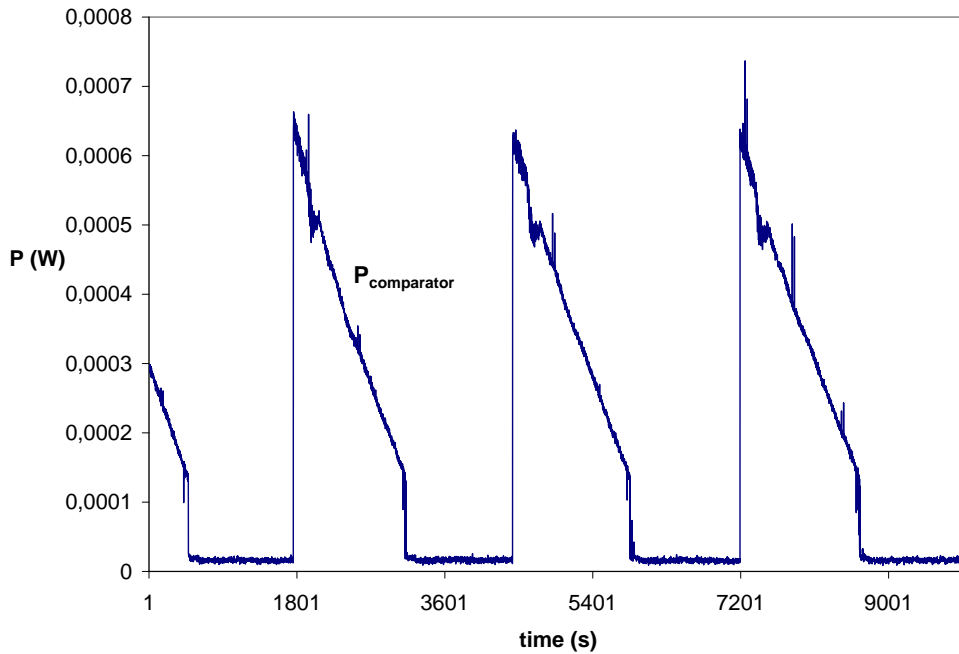


Figure 5.19: Power consumption by comparator (1.3 V to 2.5 V cycle).

While the supercapacitor cycle efficiencies (Table 5.8) are quite similar to the ones obtained for the PCB implementation of the Bologna scavenger (Table 5.6), a more than noticeable difference can be observed for the cycle efficiencies of the circuit as a whole (Table 5.7 compared to Table 5.5). The efficiencies for the prototype board are 3% up to 5% higher than for the PCB implementation. At first sight, this seems definitely strange since both circuits are practically identical - only the placement of the components has been done differently. The plot of the short-term efficiency in Figure 5.20 offers however an explanation.

		Charge/discharge interval	
		1.3 V to 2.5 V	2 V to 2.5 V
$\eta_{\text{cycle,circuit}}$ reference	1.3 V	63.51%	
	2 V	64.47%	65.59%

Table 5.7: Prototype board implementation of Bologna scavenger: cycle efficiency ($\eta_{\text{cycle,circuit}}$).

		Charge/discharge interval	
		1.3 V to 2.5 V	2 V to 2.5 V
$\eta_{cycle,cap}$ reference	1.3 V	97.57%	
	2 V	92.82%	97.97%

Table 5.8: Prototype board implementation of Bologna scavenger: cycle efficiency of supercapacitor ($\eta_{cycle,cap}$).

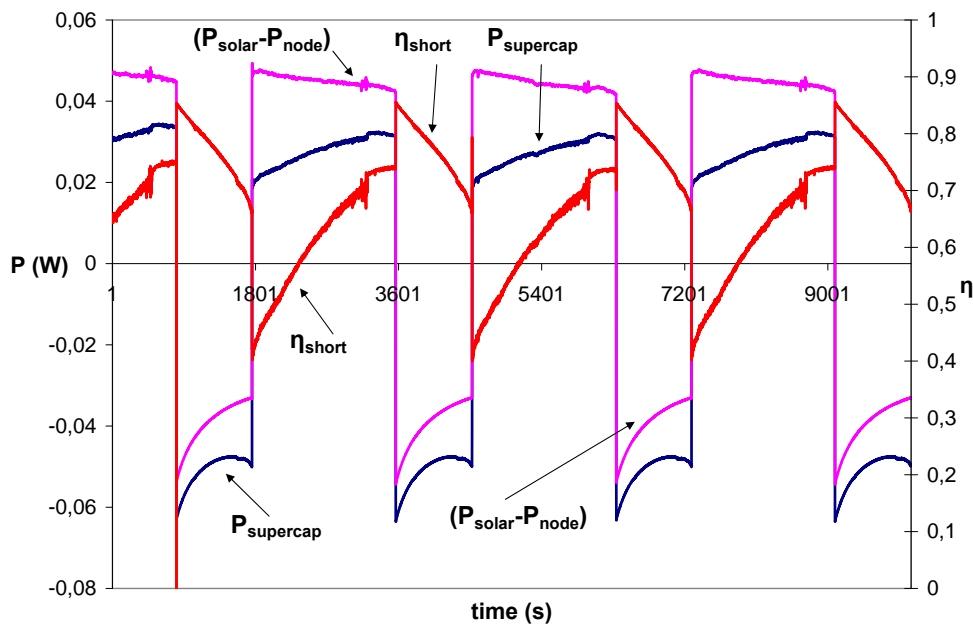


Figure 5.20: Prototype board implementation of Bologna scavenger: short-term efficiency (1.3 V to 2.5 V cycle).

In contrast to the previous section, one can notice an increasing η_{short} after the MPP tracking has stopped (visible as small positive jump of $P_{supercap}$). The power $P_{supercap}$ still decreases but does this at a rate lower than P_{node} . The short-term efficiency starts at the same minimum of 40% but increases during charging up to 73%, approximately 10% higher than the maximum η_{short} achieved in the previous section. The period during which the supercapacitor is charged without MPP tracking seems to be shorter than for the PCB implementation of the circuit (Figure 5.17). All these phenomena can be explained, directly or indirectly, by the temperature dependence of the solar cell, as will be demonstrated through the help of Figure 5.21. This figure plots the $V_{solar} - P_{solar}$ combinations recorded during the 1.3 V to 2.5 V cycle experiments for both of the Bologna scavenger implementations.

Before the prototype experiment began, the MPP of the solar cell was measured to determine the correct configuration of the voltage dividers of the MPP tracker. Although the desk lamp operated at the same light intensity and the pre-heating duration was identical, the measured MPP voltage for the prototype experiment was about 100 mV higher than for the PCB implementation experiment.

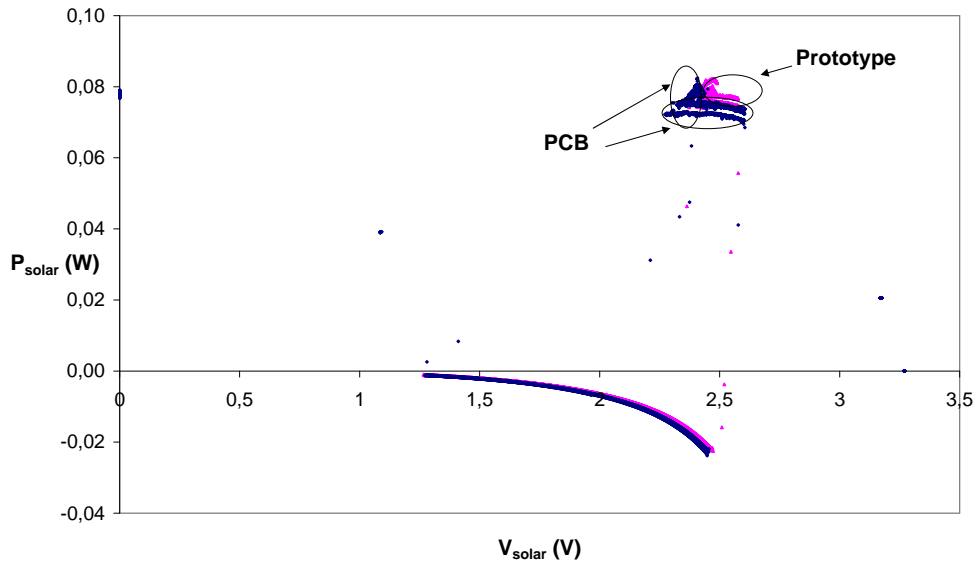


Figure 5.21: P_{solar} versus V_{solar} for PCB and prototype implementation of Bologna scavenger.

The reason behind this discrepancy can be sought in the room temperature difference between both experiments. The prototype experiment was done during a day that the airconditioning of the lab was fully active, while the PCB experiment was performed in a lab with less active airconditioning. A more active airconditioning causes a lower room temperature and more air circulation right above the solar cell. Apparently, this can have a substantial influence on the performance of the scavenger.

Because the solar cell was forced around a higher voltage during MPP tracking, the MPP tracking stops for a higher supercapacitor voltage. Since the average solar cell power is higher with than without MPP tracking this already causes a certain advantage. One can also notice in Figure 5.21 that during charging without MPP tracking, P_{solar} for the prototype experiment is higher than P_{solar} for the PCB experiment. One can conclude that, for this higher power level, the short-term efficiency increases for an increasing $V_{supercap}$. This is in contrast to the η_{short} variation for a lower solar cell power.

The solar cell power during charging with MPP tracking appears to be equal for both circuits. This already indicates that the MPP tracker of the prototype was configured incorrectly, as the maximum achievable solar cell power is higher for a lower temperature (forced voltage should be lower). This only proves how tricky the configuration of the MPP tracker can be. The more active airconditioning changed the temperature variation of the solar cell during the 40 minutes of pre-heating and also during the experiment itself. Although the MPP was measured during a similar stage of the experiment, an accurate configuration is not guaranteed. Since the solar cell power during charging with MPP tracking is practically identical for the two implementations, the reason for the higher short-term efficiency (up to 10% higher) has to be the different solar cell voltage around which the solar cell was forced. A higher solar cell voltage is apparently advantageous for the MPP tracker's efficiency.

The short-term efficiency of the tracker is influenced by the level of $V_{supercap}$, the level of V_{solar} and also by the power delivered by the solar cell. Keeping the additional influence of temperature and available light energy in mind, the prediction of the efficiency can be considered as incredibly difficult. Rough estimations of trends remain however still possible.

The energy losses of the prototype implementation are visualized in Figure 5.22. The total energy inserted in the supercapacitor during one cycle is slightly higher than the end value of $E_{circuit,adj}$ for that same cycle. This is again in contrast to the PCB implementation experiment.

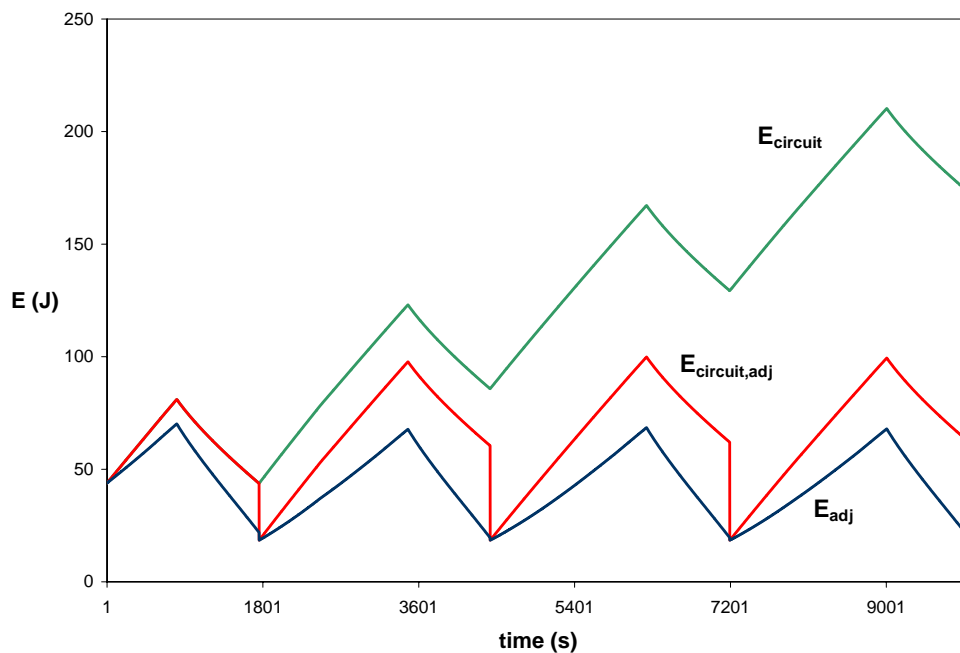


Figure 5.22: Prototype board implementation of Bologna scavenger: energy losses (1.3 V to 2.5 V cycle).

5.5 Comparative Analysis of tested circuits

The first criterion that will be used to compare the tested circuits is the long-term efficiency (Formula 5.7). The output power P_{node} equals for every circuit the 31.6 mW that was discussed in Section 5.4.3. This way, when comparing the different circuits, the onboard DC/DC converter is considered as a part of the circuit for the direct connection implementations.

	Charge/discharge interval	
	1.3 V to 2.5 V	2 V to 2.5 V
Direct connection	56%	63%
Direct connection with diode	55%	64%
Bologna scavenger (PCB)	55%	55%
Prototype board	57%	60%

Table 5.9: Long-term efficiency η_{long} for the different tested circuits.

According to Table 5.9, the four tested circuits possess a very similar η_{long} , especially for the 1.3 V to 2.5 V charge/discharge cycle experiments. For the 2 V to 2.5 V charge/discharge cycle experiments, the direct connection implementations achieve a η_{long} of a few percentage points higher than the ones for the Bologna scavenger. In general, the 2 V to 2.5 V cycle exhibits a higher long-term efficiency. This is no surprise since the highest short-term efficiencies were attained in this voltage range. One should be cautious about immediately concluding that the Bologna scavenger does not add any advantage to the overall energy scavenging capabilities of a system. The long-term efficiency is very sensitive to the used test setup and procedure. The charging and discharging times per cycle (Tables 5.10 and 5.11) will ease the interpretation of the η_{long} values.

	Charge/discharge interval	
	1.3 V to 2.5 V	2 V to 2.5 V
Direct connection	1996 s	634 s
Direct connection with diode	2598 s	840 s
Bologna scavenger (PCB)	1911 s	882 s
Prototype board	1808 s	726 s

Table 5.10: Charging times per cycle for the different tested circuits.

The charging times for the 1.3 V to 2.5 V charge/discharge cycle show faster charging by the Bologna scavenger implementations. Especially the direct connection with diode is much slower than the other circuits, which is mainly caused by the extra losses of the diode. The Bologna scavenger is responsible for a higher input energy but also for more circuit losses. Apparently, for the 1.3 V to 2.5 V charge/discharge cycle, the first effect outweighs the last one. For the 2 V to 2.5 V charge/discharge cycle on the other hand, the direct connection exhibits the shortest charging time. This can be explained by the fact that the Bologna scavenger is charged without MPP tracking for the majority of this voltage range. The provided solar cell power is very similar in this voltage range while the presence of the MPP tracker components adds extra losses. The prototype board achieves shorter charging times than the PCB implementation because of the prototype's generally higher η_{short} for the concerned test setup. Also the preservation of the normal operation of MPP tracking for higher voltages will have played a role.

	Charge/discharge interval	
	1.3 V to 2.5 V	2 V to 2.5 V
Direct connection	1034 s	443 s
Direct connection with diode	1234 s	600 s
Bologna scavenger (PCB)	894 s	408 s
Prototype board	948 s	440 s

Table 5.11: Discharging times per cycle for the different tested circuits.

The discharging time for the direct connection with diode is for both tested cycles by far the highest. This is caused by the lack of reverse solar cell current that was blocked by the diode. The prototype board is able to provide energy to the node longer than the PCB implementation. The solar cell reverse current for the same V_{solar} is lower for a higher open-circuit voltage of the solar cell. The lower temperature during the prototype tests was consequently responsible for less reverse current through the solar cell, leaving more energy for the sensor node. Figure 5.21 shows a slightly lower P_{solar} (in absolute value) during the whole duration of discharging. One can also not forget the influence of the charge distribution effects in the supercapacitor. A longer charging time will improve the charging of the slow branches, which basically means that more energy is stored in the supercapacitor. This can be the reason behind the longer discharging time for the direct connection in comparison to the PCB implementation of the Bologna scavenger. The supercapacitor behaviour makes the predictability of the energy performance even more complex.

We now return to the long-term efficiencies in Table 5.9. We already mentioned in Section 5.3.2 that η_{long} is only dependent on the ratio of the charging and discharging time per cycle. A fast charging time, like for the Bologna scavenger, can be penalized by a fast discharging time. A short charging time combined with a long discharging time enables the sensor node to run continuously while only a limited amount of solar cell power is needed, with a high η_{long} as consequence. One has to keep in mind however that this is only true for our specific test procedure. The desk lamp was turned off once 2.5 V was reached and turned on again the moment the lower boundary was crossed. In real-life situations, moments during which solar energy is available although the supercapacitor is full or during which no solar energy is available while the supercapacitor is near the minimum input voltage of the DC/DC converter, can happen. In this context, what matters the most is a fast charging time and a slow discharging time. One cannot always be sure of how long solar energy will be available and therefore a fast charging time is advantageous. A long discharging time implies that most energy is used to provide power to the sensor node and is not lost to e.g. reverse solar cell current. A long discharging time consequently entails a longer time during which a sensor node can be powered without available ambient energy. It is in this sense that the long-term efficiency can be useful as benchmark for the performance of an energy scavenger. The Bologna scavenger has a short charging time compared to the other circuits (1.3 V to 2.5 V cycle), which certainly can be considered an advantage. The discharging time is however also shorter because the circuit is less able of retaining energy than e.g.

the direct connection with diode. Overall, this leads to practically the same η_{long} .

The selection of the most suited circuit depends on the expected voltage range in which the super-capacitor will operate, the available solar energy profile and the energy consumption profile of the sensor node.

Chapter summary and conclusions

This chapter investigated the energy efficiency performance of the Bologna scavenger and used two simple direct connection implementations as references for comparison. The goal was to find out which factors can influence the performance of a photovoltaic energy scavenger and how well this performance can be predicted. Finally, we wanted to know how big the benefits of the Bologna scavenger actually are in comparison to simple direct connection implementations.

The answer to the raised questions has proved to be substantially complex. The energy efficiency of the Bologna scavenger is influenced by the available photovoltaic energy, the solar cell voltage and the voltage level of the storage supercapacitor. The influence of the solar cell's temperature on its performance and the effect of charge distribution and internal losses in the supercapacitor transform the Bologna scavenger in an even more unpredictable system. Rough estimations and the prediction of trends remain however possible. The findings in this chapter can be very helpful as guidelines for the selection of the most suited energy scavenger under a specific set of circumstances.

For the used test setup and procedure, the supercapacitors were only responsible for a maximum of 4% of the losses. This allowed us to easily distinguish the losses caused by the circuit from the losses occurring in the supercapacitor. For other charge/discharge patterns, the unregular supercapacitor behaviour will of course play a bigger role. It is also important to realize that a substantial part of the overall losses in the tested scavenger applications were caused by the DC/DC converter. The DC/DC converter used in the direct connection implementations (LTC3429) and the converter used in the Bologna scavenger circuits (LTC3401) demonstrate however for our particular test setup a practically identical efficiency performance with an efficiency ranging from 80% up to 85%, depending on the supercapacitor voltage. Therefore, a comparison of the different overall circuits can be considered as a comparison of the scavenger circuits with the DC/DC converter excluded.

For conditions of low light intensity (lower than for our test setup), the Bologna scavenger performs worse than a simple direct connection of the solar cell, the supercapacitor and the sensor node. Due to the low MPP voltage, the MPP tracker stops functioning early in the charging process (the moment $V_{supercap}$ reaches the low MPP voltage). At that point, the only difference between the direct connection and the Bologna scavenger is the additional loss taking place in the MPP tracker circuit. For high light conditions however, the Bologna scavenger can be a real asset. The MPP tracker is then able to operate normally for supercapacitor voltages up to the maximum allowed $V_{supercap}$, leading to a shorter charging time in comparison to a direct connection. This is especially useful in an environment in which periods of ample solar energy are short. A disadvantage of the Bologna scavenger circuit is the low energy retention during periods for which the solar cell's open-circuit voltage is substantially lower than the supercapacitor voltage. The reverse solar cell current that is responsible for this characteristic can be stopped by placing a diode between the solar cell and the rest of the circuit. For the direct connection, this addition of a diode caused however an increase of the charging

time of 30%. For the Bologna scavenger, a diode will also lower the maximum supercapacitor voltage that still allows normal MPP tracking operation. Therefore, it seems reasonable to add an extra low-power comparator to the circuit. This comparator can open the switch in the MPP tracker as soon as a negative solar cell current is detected (through the help of a low value permanent shunt). The extra comparator will consume about $10\ \mu\text{W}$ in an inactive state and also the shunt will cause losses. This additional energy loss will be lower than the loss in a diode and is easily compensated by the much higher energy retention that is achieved.

The charge/discharge cycles that were used for the experiments of this chapter will probably never occur in real-life situations. They were however very useful to observe and detect the dependencies and trends of the energy efficiency of the tested circuits. The guidelines mentioned above can be an ideal starting point for the implementation of an energy scavenger dedicated to a specific environment and application. The knowledge about how the circuit efficiency evolves can be used in the algorithms that run on the sensor node and that try to predict the future available energy.

Chapter 6

Conclusions

The main part of the research was focused on a specific existing scavenger design, the Bologna scavenger. This scavenger has been only recently developed and can be considered as an ideal representation of the technology that is currently available in the area of energy scavengers for sensor nodes. The scavenger uses a supercapacitor as storage device and is self-powered and self-controlled. More specifically, the following research activities have been performed:

- Extensive testing of the supercapacitor to gain a thorough understanding of its internal effects and losses.
- Detailed investigation of the working principle of the Bologna scavenger and the identification of its shortcomings.
- Tests and measurements of two simple direct connection implementations (solar cell, supercapacitor and BTnode directly connected) with a specific focus on the non-linearities in the power flows and losses.
- Tests and measurements of the Bologna scavenger with a specific focus on the non-linearities in the power flows and losses.
- Construction and testing of a prototype implementation of the Bologna scavenger that allows more elaborate measurements and enables an easy replacement of components in order to test possible circuit improvements.

The behaviour of a supercapacitor has never been tested before in the context of energy scavengers for sensor nodes. The research related to scavengers with a supercapacitor as storage device start from the assumption that a supercapacitor behaves in the same way as the classic small-value capacitors used in many electronic circuits. Chapter 3 has proved that under certain charge/discharge conditions the unregular behaviour of supercapacitors (compared to classic small-value ones) cannot be ignored. The voltage over the supercapacitor is not the only factor that indicates the stored and available electrical energy. The recent history of how the supercapacitor has been charged and discharged carries

an equally important weight. For certain conditions, supercapacitor efficiencies of only 70% were observed, meaning that 30% of the inserted energy could not be extracted from the supercapacitor although its voltage indicated all inserted energy had been returned. In the context of predictability of available electrical energy, these observations entail the necessary inclusion of supercapacitor behaviour in the sensor node optimization algorithms. Chapter 3 discussed a simulation model for supercapacitors that originates from the field of power electronics and that was used to explain the observed behaviour conceptually. In case this model proves to be accurate enough for the supercapacitors used in energy scavengers, model parameters can be extracted. Extensive simulations and additional measurements can then lead to look-up tables that enable a better estimation of the actual energy a supercapacitor can provide.

Chapter 4 investigated the working principle of the Bologna scavenger and demonstrated that a correct maximum power point tracking operation is certainly not guaranteed. Especially for low light conditions (= indoor conditions with artificial light only) the scavenger exhibits serious shortcomings that lead to unacceptable energy loss. The extent of the influence of characteristics like the solar cell's temperature and the configuration of the MPP tracker was also examined. Based on the knowledge gained in Chapter 4, we can conclude that the Bologna scavenger architecture is not suited for indoor applications with limited available light. The change of component values can improve the efficiency and overall performance of the circuit. Low light conditions will however require the design of a new circuit architecture. Slight modifications of a boost converter architecture seem at this point the best candidates for a first tryout.

The profound understanding of the working principle of the scavenger that was obtained in Chapter 4, was used in Chapter 5 to interpret the several measurement results. Those results led to significantly more insight in how much electrical energy can be expected for a certain available solar energy. A lot of attention was given to the performance of two direct connection implementations. After all, an advanced scavenger circuit is only useful when its performance exceeds the performance of a very simple direct connection between solar cell, supercapacitor and sensor node. Therefore, the obtained measurement results for the two circuits can be used as references for all other scavenger circuits. Chapter 5 demonstrated how for certain conditions, a direct connection is to be preferred above the Bologna scavenger. For high enough light conditions, the Bologna scavenger can reduce the charging time of a supercapacitor substantially. The scavenger however also suffers from a low energy retention during low light conditions, causing similar overall round-trip efficiencies (of 55% up to 65%) for the direct connection circuits and the Bologna scavenger. A solution for this low energy retention, based on an additional low-power comparator, was proposed in the end of the chapter. Finally, the prototype board that we constructed ourselves was successfully tested. Not all features of the board have been already put into use, like e.g. the easy replacement of components that allows the investigation of the influence of changed component values. This is certainly something that can be done in the future.

Appendix A

More pictures

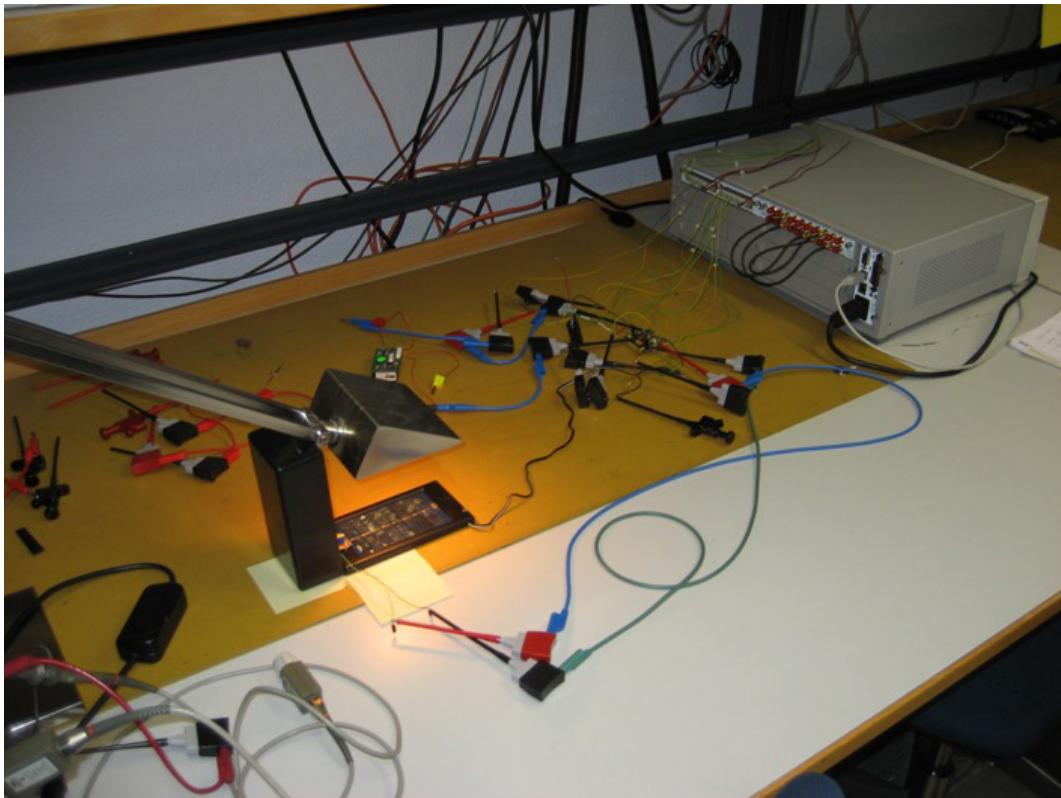


Figure A.1: Test setup with Bologna scavenger (PCB version).

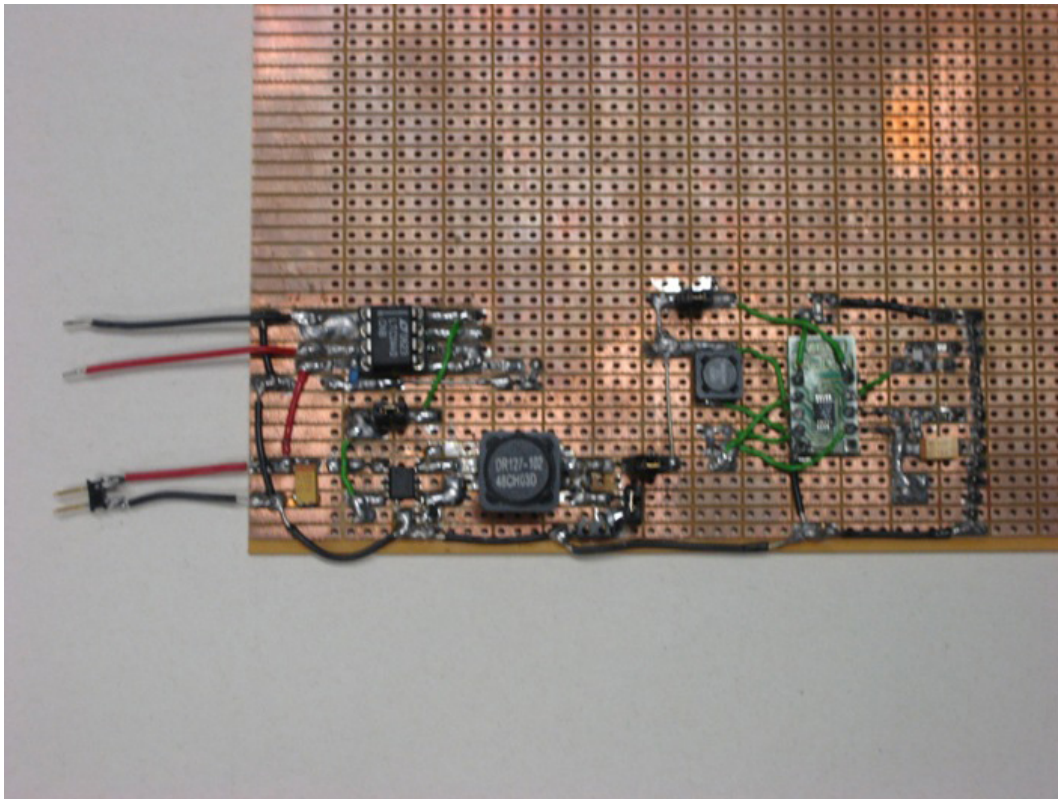


Figure A.2: Prototype implementation of the Bologna scavenger.



Figure A.3: The BTnode sensor node.

List of Figures

2.1	Equivalent circuit of a solar cell.	4
2.2	VI and VP curve of a solar cell.	5
2.3	System architecture and Prometheus implementation.	8
2.4	Architecture of Ambimax platform	9
2.5	Reservoir supercapacitor array	9
2.6	Everlast system block diagram.	10
3.1	The Gouy-Chapman model.	12
3.2	The Stern model.	13
3.3	An individual supercapacitor cell.	14
3.4	A cross-section of a supercapacitor.	14
3.5	A supercapacitor image indicating the distribution of the solvent's molecules.	15
3.6	Ragone chart showing energy density vs. power density for various energy storing devices	16
3.7	A 54V/175F NESSCAP ultracapacitor bank module	18
3.8	Supercapacitor model based on physical structure.	20
3.9	Supercapacitor model	21
3.10	Schematic representation of the elementary component of a transmission line.	22
3.11	An electrode pore as a sequence of elementary transmission line elements.	22
3.12	Supercapacitor test setup.	23
3.13	Cooper-Bussmann supercapacitor B series.	23
3.14	Leakage phenomenon in a single supercapacitor: voltage.	25
3.15	Leakage phenomenon in a single supercapacitor: energy content.	25
3.16	Series connection of two identical supercapacitors.	26
3.17	Leakage phenomenon in a series connection of two supercapacitors: voltage.	26
3.18	Leakage phenomenon in a series connection of two supercapacitors: energy content.	26
3.19	Single cycle with quick charging and slow discharging (short pre-charging).	29
3.20	Single cycle with quick charging and slow discharging (1 hour pre-charging).	29
3.21	Single cycle with quick charging and quick discharging.	30
3.22	Single cycle with slow charging and slow discharging.	30

3.23	Single cycle with slow charging and quick discharging.	31
3.24	Single cycle with long delay interval.	34
3.25	Long delay after short single cycle.	34
3.26	Long delay after short single cycle.	35
3.27	Long single cycle.	36
3.28	Multiple charge/discharge cycles between 0.25 V and 2.5 V.	37
3.29	Multiple charge/discharge cycles: cycle efficiencies (η_{cycle}).	38
3.30	Multiple charge/discharge cycles between 0.25 V and 2.5 V: one cycle.	38
3.31	Multiple charge/discharge cycles between 1.3 V and 2.5 V: one cycle.	39
3.32	Multiple charge/discharge cycles between 2 V and 2.5 V: one cycle.	39
3.33	Multiple charge/discharge cycles between 1.3 V and 2.5 V: influence of pre-charging on η_{cycle}	40
3.34	Multiple charge/discharge cycles between 0.25 V and 2.5 V: cycle efficiency with 1.3 V as reference.	41
3.35	Charge distribution in equivalent circuit model at beginning of discharge phase.	42
4.1	Buck converter architecture.	45
4.2	Complete MPP tracker circuit.	46
4.3	MPP tracker circuit with open switch.	46
4.4	MPP tracker circuit with closed switch.	47
4.5	MPP tracker simulation.	49
4.6	DC/DC converter (LTC3401) circuit.	50
4.7	Boost converter architecture.	50
4.8	DC/DC converter in fixed frequency (300 kHz) mode.	52
4.9	DC/DC converter in burst mode.	52
4.10	DC/DC converter in burst mode (more detail).	53
4.11	LTC3401 efficiency: step-up from 1.2V to 3.3V.	53
4.12	The complete Bologna scavenger circuit.	54
4.13	Bottom layer of the Bologna scavenger PCB.	55
4.14	Top layer of the Bologna scavenger PCB.	55
4.15	Test setup for the Bologna scavenger.	56
4.16	Principle of the Agilent 34921A 40-Channel Armature Multiplexer.	57
4.17	VI and VP curve: maximum obtainable power for test setup.	58
4.18	VI and VP curve: behind window during typical sunny day.	58
4.19	VI and VP curve: lab environment without additional lighting.	59
4.20	Relation between V_{oc} , V_{mpp} and V_{pilot}	60
4.21	Ratio of V_{mpp} and V_{pilot} as a function of V_{oc}	60
4.22	Temperature influence on VP curve of solar cell: lamp on.	61
4.23	Temperature influence on VI curve of solar cell: lamp on.	62

4.24	Temperature influence on VP curve of solar cell: lamp off.	62
4.25	Temperature influence on relation between V_{mpp} and V_{pilot}	63
4.26	Normal operation: V_{solar} and $V_{supercap}$	64
4.27	Normal operation: P_{solar} as a function of V_{solar}	64
4.28	Unwanted behaviour: V_{solar} , $V_{supercap}$ and I_{solar}	65
4.29	Oscilloscope screenshot of V_{solar} and V_{gate} : $V_{supercap} = 0.9\text{ V}$	66
4.30	Oscilloscope screenshot of V_{solar} and V_{gate} : $V_{supercap} = 1.4\text{ V}$	66
4.31	Oscilloscope screenshot of V_{solar} and V_{gate} : $V_{supercap} = 1.8\text{ V}$	67
4.32	Oscilloscope screenshot of V_{solar} and V_{gate} : $V_{supercap} = 2.2\text{ V}$	67
4.33	Oscilloscope screenshot of V_{solar} and V_{gate} : $V_{supercap} = 2.28\text{ V}$	68
4.34	Oscilloscope screenshot of V_{solar} and V_{gate} : $V_{supercap} = 2.3\text{ V}$	68
4.35	Oscilloscope screenshot of $I_{supercap}$: $V_{supercap} = 1\text{ V}$	69
4.36	Oscilloscope screenshot of $I_{supercap}$: $V_{supercap} = 1.4\text{ V}$	70
4.37	Oscilloscope screenshot of $I_{supercap}$: $V_{supercap} = 1.8\text{ V}$	70
4.38	Oscilloscope screenshot of $I_{supercap}$: $V_{supercap} = 2.2\text{ V}$	71
4.39	Oscilloscope screenshot of $I_{supercap}$: $V_{supercap} = 2.3\text{ V}$ (Sampling rate is 4 times lower than for other $I_{supercap}$ waveforms).	71
4.40	MPP tracking operation ends.	72
4.41	Unwanted behaviour: P_{solar} as a function of V_{solar}	74
4.42	Comparator supply issue: V_{solar} , V_{node} and $V_{supercap}$	74
5.1	Direct connection test setup.	78
5.2	Direct connection test setup.	79
5.3	Short-term efficiency principle.	83
5.4	Influence of switching in DMM on measurement results.	85
5.5	Direct connection: current measurements with external shunts.	86
5.6	Direct connection: 1.3 V to 2.5 V charge/discharge cycle.	87
5.7	Direct connection: P_{solar} versus V_{solar} (1.3 V to 2.5 V cycle).	87
5.8	Direct connection: supercapacitor's energy content (1.3 V to 2.5 V cycle).	89
5.9	Direct connection: supercapacitor's energy content (2 V to 2.5 V cycle).	89
5.10	Direct connection: short-term efficiency (2 V to 2.5 V cycle).	90
5.11	Direct connection with diode: 1.3 V to 2.5 V charge/discharge cycle.	90
5.12	Direct connection with diode: P_{solar} versus V_{solar} (1.3 V to 2.5 V cycle).	91
5.13	Direct connection with diode: short-term efficiency (1.3 V to 2.5 V cycle).	92
5.14	Direct connection with diode: energy losses (1.3 V to 2.5 V cycle).	93
5.15	Bologna scavenger: 1.3 V to 2.5 V charge/discharge cycle.	94
5.16	Bologna scavenger: P_{node} (1.3 V to 2.5 V cycle).	96
5.17	Bologna scavenger: short-term efficiency (1.3 V to 2.5 V cycle).	96
5.18	Bologna scavenger: energy losses (1.3 V to 2.5 V cycle).	97

<i>List of Figures</i>	114
5.19 Power consumption by comparator (1.3 V to 2.5 V cycle).	98
5.20 Prototype board implementation of Bologna scavenger: short-term efficiency (1.3 V to 2.5 V cycle).	99
5.21 P_{solar} versus V_{solar} for PCB and prototype implementation of Bologna scavenger. . .	100
5.22 Prototype board implementation of Bologna scavenger: energy losses (1.3 V to 2.5 V cycle).	101
A.1 Test setup with Bologna scavenger (PCB version).	109
A.2 Prototype implementation of the Bologna scavenger.	110
A.3 The BTnode sensor node.	110

List of Tables

3.1	Cooper-Bussmann supercapacitor B series specifications.	24
3.2	Voltage distribution over the series connection: start of the experiment.	27
3.3	Voltage distribution over the series connection: end of the experiment.	27
3.4	Used resistance values for the charge and the discharge resistor.	28
3.5	Cycle efficiencies (η_{cycle}).	31
3.6	The energy E_{in} for the different tested cycles.	32
3.7	The energy E_{out} for the different tested cycles.	32
3.8	Difference between E and E_{form} after charging (%).	32
3.9	Energy loss during delay according to $E = CV^2/2$ (%).	32
3.10	Difference between actual and formula-based E_{out} (%).	33
3.11	Average cycle efficiencies (η_{cycle}) for multiple cycles	41
3.12	Average charging times for multiple cycles.	41
3.13	Average discharging times for multiple cycles.	42
5.1	Direct connection: cycle efficiency ($\eta_{cycle,circuit}$).	88
5.2	Direct connection: cycle efficiency of supercapacitor ($\eta_{cycle,cap}$).	88
5.3	Direct connection with diode: cycle efficiency ($\eta_{cycle,circuit}$).	91
5.4	Direct connection with diode: cycle efficiency of supercapacitor ($\eta_{cycle,cap}$).	92
5.5	Bologna scavenger: cycle efficiency ($\eta_{cycle,circuit}$).	95
5.6	Bologna scavenger: cycle efficiency of supercapacitor ($\eta_{cycle,cap}$).	95
5.7	Prototype board implementation of Bologna scavenger: cycle efficiency ($\eta_{cycle,circuit}$).	98
5.8	Prototype board implementation of Bologna scavenger: cycle efficiency of supercapacitor ($\eta_{cycle,cap}$).	99
5.9	Long-term efficiency η_{long} for the different tested circuits.	102
5.10	Charging times per cycle for the different tested circuits.	102
5.11	Discharging times per cycle for the different tested circuits.	103

Bibliography

- [1] Clemens Moser, Lothar Thiele, Davide Brunelli, and Luca Benini. Adaptive Power Management for Energy Harvesting Systems. In *Design, Automation and Test in Europe (DATE 07)*, Nice, France, April 16-20 2007.
- [2] C. Moser, L. Thiele, L. Benini, and D. Brunelli. Real-time scheduling with regenerative energy. In *ECRTS '06: Proceedings of the 18th Euromicro Conference on Real-Time Systems*, pages 261–270, Washington, DC, USA, 2006. IEEE Computer Society.
- [3] Xiaofan Jiang, Joseph Polastre, and David E. Culler. Perpetual environmentally powered sensor networks. In *Proceedings of the Fourth International Symposium on Information Processing in Sensor Networks, IPSN 2005*, pages 463–468, UCLA, Los Angeles, California, USA, April 25-27 2005.
- [4] Farhan Simjee and Pai H. Chou. Everlast: Long-life, supercapacitor-operated wireless sensor node. In *Proc. Int. Symposium on Low Power Electronics and Design (ISLPED)*, October 2006.
- [5] C. Park and Pai H. Chou. Ambimax: Autonomous energy harvesting platform for multi-supply wireless sensor nodes. In *Proc. Third Annual IEEE Communications Society Conference on Sensor, Mesh, and Ad Hoc Communications and Networks (Secon'06)*, pages 168–177, Reston, VA, USA, September 25-28 2006.
- [6] Davide Brunelli, Luca Benini, Clemens Moser, and Lothar Thiele. An efficient solar energy harvester for wireless sensor nodes. In *Design, Automation and Test in Europe (DATE 08)*, Munich, Germany, March 10-14 2008.
- [7] Simone Raggini. Designing of a solar harvester system for micro sensor networks. progettazione di un sistema per alimentazione solare di un nodo sensore miniaturizzato. Master's thesis, University of Bologna, 2006.
- [8] J. Beutel, M. Dyer, M. Hinz, L. Meier, and M. Ringwald. Next-generation prototyping of sensor networks. In *Proc. 2nd ACM Conf. Embedded Networked Sensor Systems (SenSys 2004)*, pages 291–292. ACM Press, New York, November 2004.
- [9] T. Eswam and P. L. Chapman. Comparison of photovoltaic array maximum power point tracking techniques. *IEEE Transactions on Energy Conversion*, 22(2):439–449, June 2007.

- [10] T. Noguchi, S. Togashi, and R. Nakamoto. Short-current pulse-based maximum-power-point tracking method for multiple photovoltaic-and-converter module system. *IEEE Transactions on Industrial Electronics*, 49(1):217–223, February 2002.
- [11] Dong-Yun Lee, Hyeong-Ju Noh, Dong-Seok Hyun, and Ick Choy. An improved mppt converter using current compensation method for small scale pv-applications. In *IEEE 18th Annual Applied Power Electronics Conf. and Expo.*, 2003.
- [12] A.M. Namisnyk and J.G. Zhu. A survey of electrochemical supercapacitor technology. In *Australasian Universities Power Engineering Conference*, 2003.
- [13] J. P. Rothstein. Electrokinetics, lecture 7. Technical report, University of Massachusetts, Amherst, 2005.
- [14] P. Barrade. Energy storage and applications with supercapacitors. Technical report, Laboratoire d'Electronique Industrielle, STI-ISE, Ecole Polytechnique Fédérale de Lausanne, EPFL, 2003.
- [15] Ultracapacitors.org. How an ultra capacitor works. <http://www.ultracapacitors.org/how-an-ultra-capacitor-works.htm>.
- [16] K. Y. C. Cheung, S. T. H. Cheung, R.G. Navin De Silva, M. P. T. Juvonen, R. Singh, and J.J. Woo. Large-scale energy storage systems. Technical report, Imperial College London, ISE2, 2002/2003.
- [17] A Green and C. Jehoulet. The non-battery battery - the potential role of supercapacitors in standby power applications. Technical report, Saft, 2002.
- [18] P. Barrade. Series Connection of Supercapacitors: Comparative Study of Solutions for the Active equalization of the Voltages. In *Electrimacs 2002, 7th International Conference on Modeling and Simulation of Electric Machines, Converters and Systems*, 2002.
- [19] K Youngho. Ultracapacitor technology powers electronic circuit. *Power Electronics Technology*, pages 34–39, October 2003.
- [20] L. Zubieta and R. Bonert. Characterization of double-layer capacitors for power electronics applications. *IEEE Transactions on Industry Applications*, 36(1):199–205, January/February 2000.
- [21] L. Zubieta. Characterization of double-layer capacitors for power electronics applications. Master's thesis, Dep. Elect. Comput. Eng., Univ. Toronto, Toronto, Ont., Canada, 1984.
- [22] F. Belhachemi, S. Rael, and B. Davat. A physical based model of power electric double-layer supercapacitors. In *Industry Applications Conference, 2000. Conference Record of the 2000 IEEE*, 2000.

- [23] WELWYN. Resistor, 1206 0R5, Datasheet. <http://www.farnell.com/datasheets/80966.pdf>.
- [24] Cooper Bussmann. Aerogel Supercapacitors B Series, Datasheet. <http://www.bussmann.com/pdf/39719066-0619-4987-bc43-55222fa5727a.pdf>.
- [25] Agilent Technologies. 34980A Multifunction Switch/Measure Unit, Manual. http://www.home.agilent.com/upload/cmc_upload/All/34980-90001_Ed3.pdf.
- [26] Agilent Technologies. 34980A Multifunction Switch/Measure Unit, Datasheet. <http://cp.literature.agilent.com/litweb/pdf/5989-1437EN.pdf>.
- [27] Linear Technology. LTC1440 - Ultralow Power Single/Dual Comparator with Reference, Datasheet. <http://www.linear.com/pc/downloadDocument.do?navId=H0,C1,C1154,C1002,C1463,P1172,D2764>.
- [28] Solarex. MSX-005F, Solar Panel 0.5W, Datasheet. <http://www.farnell.com/datasheets/8196.pdf>.
- [29] Clare, an IXYS company. CPC1824, 4V Output Solar Cell, Datasheet. [http://www.clare.com/home/pdfs.nsf/www/CPC1824.pdf/\\$file/CPC1824.pdf](http://www.clare.com/home/pdfs.nsf/www/CPC1824.pdf/$file/CPC1824.pdf).
- [30] Moteiv Corporation. Tmote sky - ultra low power iee 802.15.4 compliant wireless sensor module, datasheet. <http://www.moteiv.com/products/docs/tmote-sky-datasheet.pdf>, June, 2006.
- [31] Linear Technology. LTC3401 - 1A, 3MHz Micropower Synchronous Boost Converter, Datasheet. <http://www.linear.com/pc/downloadDocument.do?navId=H0,C1,C1003,C1042,C1031,C1060,P1897,D2673>.
- [32] Linear Technology. LTC3429 - 600mA, 500kHz Micropower Synchronous Boost Converter with Output Disconnect, Datasheet. <http://www.linear.com/pc/downloadDocument.do?navId=H0,C1,C1003,C1042,C1031,C1060,P2346,D2041>.